LEAD MAGNESIUM NIOBATE TITANATE THICK FILMS PREPARED BY AEROSOL DEPOSITION METHOD

Matej Šadl

Doctoral Dissertation
Jožef Stefan International Postgraduate School
Ljubljana, Slovenia

Supervisor: Assoc. Prof. Dr. Hana Uršič Nemevšek, Jožef Stefan Institute, Ljubljana, Slovenia

Evaluation Board:
Assoc. Prof. Dr. Matjaž Spreitzer, Chair, Jožef Stefan Institute, Ljubljana, Slovenia
Prof. Dr. Andrej Kitanovski, Member, Faculty of Mechanical Engineering, University of Ljubljana, Ljubljana, Slovenia
Dr. Jaroslaw Kita, Member, University of Bayreuth, Bayreuth, Germany

MEDNARODNA PODIPLOMSKA ŠOLA JOŽEFA STEFANA
JOŽEF STEFAN INTERNATIONAL POSTGRADUATE SCHOOL

Matej Šadl

LEAD MAGNESIUM NIOBATE TITANATE THICK FILMS PREPARED BY AEROSOL DEPOSITION METHOD

Doctoral Dissertation

DEBELE PLASTI SVINČEVEGA MAGNEZIJEVEGA NIOBATA TITANATA PRIPRAVLJENE Z METODO NANAŠANJA V AEROSOLU

Doktorska disertacija

Supervisor: Assoc. Prof. Dr. Hana Uršič Nemevšek

Ljubljana, Slovenia, October 2022

Acknowledgments

I found it fascinating to deal with the subject of aerosol deposition (AD). Researching and implementing the method in the Electronic Ceramics Department (K5), Jožef Stefan Institute (JSI) was a new and interesting challenge. But the work on AD would not have been possible without three ambitious researchers at K5: Dr. Marko Vrabelj, Asst. Prof. Dr. Mojca Otoničar and Assoc. Prof. Dr. Hana Uršič Nemevšek. They were successful with their great idea and received the JSI Director's fund in 2017 for the establishment of the Laboratory for the ultracool preparation of complex oxides - ULTRACOOL at K5, including the AD equipment.

This work would not have been possible without my supervisor Assoc. Prof. Dr. Hana Uršič Nemevšek. She believed in me from the very beginning. She gave me a lot of support, guidance and knowledge, while her optimism constantly motivated me. She was an attentive and patient mentor. I must also thank our head of department Prof. Dr. Barbara Malič, who gave me the opportunity to be part of the K5 team since 2014. Because of her, the environment in the department always felt familiar.

There are many colleagues in the K5 department who helped me during my PhD studies. Dr. Andraž Bradeško and Dr. Uroš Prah were very helpful when I needed help and always willing to share their skills and advice with me. Without them, I would not have been able to get so into the experimental work and measurements. I am grateful to Oana Condurache and Assoc. Prof. Dr. Andreja Benčan for their work on transmission electron microscopy. Asst. Prof. Dr. Mirela Dragomir was very valuable as she provided me with all the knowledge for Rietveld refinement analysis. Assoc. Prof. Dr. Tadej Rojac and Assoc. Prof. Dr. Danjela Kuščer contributed with fruitful discussions.

I would also like to thank our technical staff Jena Cilenšek, Silvo Drnovšek, Brigita Kmet and Andrej Debevec and students Antonio Lisičak, Remy Lecomte and Nejc Suban for their technical support in performing the experiments and analyses. I must also thank our students at the atomic force microscope Val Fišinger, Maria Karypidou and Reham Elshuraf who were very diligent in making the measurements. Basically, I am grateful to all current and former K5 staff, who all contributed to a great and very supportive atmosphere.

I would also like to thank the staff outside the Jožef Stefan Institute. The list of our good friends is quite long. Udo Eckstein, Neamul H. Khansur and Kyle G. Webber from Friedrich-Alexander-Universität Erlangen-Nürnberg (FAU); Marco Deluca from Materials Centre Leoben Forschung GmbH (MCL); Kevin Nadaud, Micka Bah, and Franck Levassort from the laboratory GREMAN UMR 7347, Université de Tours; Urban Tomc, Andrej Lebar, and Joško Valentinčič from the Faculty of Mechanical Engineering, University of Ljubljana. Finally, I must not forget Edi Kranjc from the Slovenian National Institute of Chemistry, who made the X-ray measurements, and Michael Schubert and Jörg Exner from the University of Bayreuth, who taught us basic and practical things about the AD process.

The work presented in the dissertation was funded by the JSI Director's fund 2017-ULTRACOOL and Slovenian Research Agency (young researcher project PR-08977,

research projects J2-3058 and N2-0212, research core funding P2-0105 and bi-lateral projects BI-DE-20/21-012 and BI-FR/21-22-PROTEUS-004).

Finally, I would like to express my great gratitude to my dear friends and family. I appreciate their trust and enthusiasm. My biggest supporters were especially my parents and my girlfriend Tjaša.

Abstract

The miniaturization of electronic devices requires the fabrication of functional components in the form of µm-sized thick films. Some of the most promising functional materials are relaxor-ferroelectric (1-x)Pb($Mg_{1/3}Nb_{2/3}$)O_3–$x$$PbTiO_3$ (PMN–100xPT), as they exhibit versatile dielectric, piezoelectric and relaxor-ferroelectric properties. However, the integration of functional ceramic thick films with non-conventional substrates such as metals and polymers remains challenging due to the thermally activated processes and incompatibilities that arise during the high-temperature sintering process of ceramics. To overcome the integration barrier, an aerosol deposition (AD), spray-coating method based on room-temperature deposition is used.

In this work, PMN–100xPT thick films were deposited on low-cost substrates using the AD method. We deposited PMN–10PT and PMN–35PT on stainless-steel (SS) and PMN–10PT on flexible polyimide (PI) substrates. The focus of this thesis is on the optimization of the deposition process of thick films and on the effect of thermal annealing the samples on their structural, microstructural and functional properties.

First, the main material parameters for successful AD of the powder were identified and used in the process. It was found that after the mechanochemically assisted synthesis of PMN–10PT powder, additional powder treatments such as heating and subsequent milling are crucial for efficient film deposition, as the treatment yields highly crystalline powder particles in the range of several hundred nm. The optimized PMN–10PT and PMN–35PT powders resulted in high-density and few-µm-thick films with very low porosity (1.5–3.0%) and good adhesion. These are also the properties that contribute to the very high dielectric breakdown strength of the films (above 900 $kV \cdot cm^{-1}$).

The as-deposited thick films were thermally annealed at temperatures of 400 °C (for PI substrates) and 500 °C (for SS substrates), which are far below the temperatures for sintering ceramics. Thermal annealing at such moderate temperatures does not change the microstructure of the ceramic thick films, i.e., crystallite and grain growth is insignificant, and the density remains the same. However, thermal annealing leads to compressive stress relaxation in PMN–10PT and PMN–35PT thick films, which is evident from structural analysis by X-ray diffraction and Raman spectroscopy. The as-deposited films show promising room-temperature electrical energy-storage properties, which improve after thermal annealing due to stress relaxation. After thermal annealing, the recoverable energy-storage density (U_{rec}) and energy-storage efficiency (η) reach 8.8–9.8 $J \cdot cm^{-3}$ and 61–79% at 900 $kV \cdot cm^{-1}$, respectively. In particular, the PMN–10PT thick films on SS exhibit excellent temperature stability up to 200 °C and electric field cycling stability up to $16 \cdot 10^6$ cycles. The PMN–10PT thick films on PI were subjected to flexural bending tests, which showed high flexibility (1.1% bending strain) and high durability (10^5 bending cycles). The piezoelectric activity of the AD thick films was also confirmed for the PMN–35PT thick films on SS. The as-deposited and annealed thick films achieve a piezoelectric coefficient of 25 and 41 $pm \cdot V^{-1}$, respectively. We demonstrate that the integration of PMN–100xPT on low-cost substrates such as SS and PI is feasible, which can significantly impact the diversity and affordability of future electro-energy systems and devices.

Povzetek

Miniaturizacija elektronskih naprav zahteva pripravo funkcijskih komponent v obliki mikrometrskih debelih plasti. Eden izmed najbolj obetavnih funkcijskih materialov je relaksorski feroelektrik (1-x)Pb($Mg_{1/3}Nb_{2/3}$)O_3–$x$$PbTiO_3$ (PMN–100xPT), saj izkazuje vsestranske dielektrične, piezoelektrične in relaksor-feroelektrične lastnosti. Integracijo funkcijskih keramičnih materialov na neuveljavljene substrate, kot so kovine in polimeri, otežuje pojav termičnih procesov ob visokotemperaturnem postopku sintranja keramike.

V tej doktorski nalogi smo debele plasti PMN–100xPT nanesli na nizkocenovne podlage. Z namenom učinkovitejšega združevanja materialov smo uporabili metodo nanosa plasti v aerosolu (ang.: *aerosol deposition*, AD), ki temelji na pršenju delcev in oblikovanju prevlek pri sobni temperaturi. Plasti PMN–10PT in PMN–35PT smo nanesli na podlage iz nerjavnega jekla (ang.: *stainless steel*, SS) in upogljivega poliimida (PI). Osredotočali smo se na optimizacijo procesa nanašanja debelih plasti na podlage in na vpliv segrevanja vzorcev na njihove strukturne, mikrostrukturne in funkcijske lastnosti.

Opredelili smo ključne korake obdelave prahu, ki omogočajo uspešen nanos plasti. Ugotovili smo, da je za učinkovit nanos plasti prah potrebno po mehanokemijski sintezi dodatno segreti in mleti. Po omenjenem postopku postane prah visoko kristaliničen z nekaj sto nm velikimi delci. Z optimiziranimi prahovi PMN–10PT in PMN–35PT smo pridobili nekaj µm debele plasti z visoko gostoto, nizko poroznostjo (1,5–3,0 %) in dobrim spojem s podlago. Na zelo visoko dielektrično prebojno trdnost debelih plasti (več kot 900 $kV \cdot cm^{-1}$) pomembno vplivata predvsem debelina in visoka gostota.

Debele plasti smo v nadaljevanju toplotno obdelali pri temperaturah, nižjih od temperatur, ki so potrebne za sintranje keramike. Plasti na PI smo segreli na 400 °C in plasti na SS na 500 °C. Te zmerne temperature niso vplivale na mikrostrukturo debelih plasti, saj je bila rast kristalitov in zrn zanemarljiva, gostota plasti pa je ostala enaka. Iz strukturnih analiz rentgenske difrakcije in ramanske spektroskopije je razvidno, da je segrevanje debelih plasti PMN–10PT in PMN–35PT vodilo v popuščanje tlačnih napetosti, ki so se v plasteh razvile med postopkom nanašanja. Nanešene debele plasti izkazujejo lastnosti, ki so obetavne za shranjevanje električne energije. Te lastnosti se po segrevanju še izboljšajo zaradi popuščanja napetosti. Po segrevanju doseže gostota povrnjene električne energije (ang.: *recoverable energy-storage density*, U_{rec}) v plasteh 8,8–9,8 $J \cdot cm^{-3}$ in učinkovitost shranjevanja električne energije (η) 61–79 % pri električnem polju 900 $kV \cdot cm^{-1}$. Debele plasti PMN–10PT na SS izkazujejo tudi odlično temperaturno stabilnost do 200 °C in odlično odpornost proti električnemu utrujanju do $16 \cdot 10^6$ ciklov. Na debelih plasteh PMN–10PT na PI smo naredili teste upogibanja, ki so pokazali visoko prožnost (brez poškodbe do 1,1 % upogibne napetosti) in visoko trpežnost (do 10^5 ciklov upogibanja). V debelih plasteh PMN–35PT na SS smo potrdili tudi piezoelektrični pojav. Nanešeni vzorci dosežejo piezoelektrični koeficient 25 $pm \cdot V^{-1}$, dodatno segreti vzorci pa 41 $pm \cdot V^{-1}$. Dokazali smo, da je integracija debelih plasti PMN–100xPT na nizkocenovne podlage izvedljiva, kar lahko občutno vpliva na raznolikost in dostopnost bodočih elektronsko-energetskih sistemov in naprav.

Contents

List of Figures

List of Tables

Abbreviations

a.u.	... arbitrary units
ABO_3	... chemical formula of the perovskite unit cell
AC	... alternating current
AD	... aerosol deposition
AFM	... atomic force microscopy
BNT-SBT	... $(Bi,Na)TiO_3$–$(Sr,Bi)TiO_3$
BT	... $BaTiO_3$
BZN	... $Bi(Zn,Nb)O_3$
cAFM	... conductive atomic force microscopy
CNRS	... French National Centre for Scientific Research
DAAD	... German Academic Exchange Service
DBLI	... double-beam laser interferometer
DBS	... dielectric breakdown strength
DC	... direct current
EDXS	... energy-dispersive X-ray spectrometer
ERC	... European Research Council
FAU	... Friedrich-Alexander-Universität Erlangen-Nürnberg
FE-SEM	... field-emission scanning electron microscope
FPA	... fundamental parameters' approach
H	... heat-treated powder
HM30	... heat-treated and milled (30 min) powder
HM60	... heat-treated and milled (60 min) powder
INSA CVL	... French National Institutes of Science and Technology, Centre Val de Loire
IPA	... isopropanol
JCPDS	... joint committee on powder-diffraction standards
JSI	... Jožef Stefan Institute
KNNLN	... $(K,Na)NbO_3$–$LiNbO_3$
MCL	... Materials Center Leoben Forschung GmbH
MPB	... morphotropic phase boundary
NT	... non-treated powder
PECS	... precision etching and coating system
PFM	... piezo-response force microscopy
PI	... polyimide
PLZT	... $(Pb,La)(Zr,Ti)O_3$
PMN	... $Pb(Mg_{1/3}Nb_{2/3})O_3$
PMN–100xPT	... $(1\text{-}x)Pb(Mg_{1/3}Nb_{2/3})O_3$–$xPbTiO_3$
PMN–10PT	... $0.9Pb(Mg_{1/3}Nb_{2/3})O_3$–$0.1PbTiO_3$
PMN–35PT	... $0.65Pb(Mg_{1/3}Nb_{2/3})O_3$–$0.35PbTiO_3$
PNR	... polar nano-region
PT	... $PbTiO_3$

PZT	... $Pb(Zr,Ti)O_3$
RF	... radio frequency
SAED	... selected-area electron diffraction
SBLI	... single-beam laser interferometer
SS	... stainless steel
TEM	... transmission electron microscopy
XRD	... X-ray diffraction
YSZ	... yttria-stabilized zirconia

Symbols

2θ	... X-ray diffraction angle
$a,\ c$	... unit-cell parameters
b	... distance between the neutral mechanical plane in the thick film structure and the film surface
D	... dielectric displacement
d	... interplanar spacing
$d^*_{33\ eff}$	... inverse effective longitudinal piezoelectric coefficient
$d_{33\ eff}$	... direct effective longitudinal piezoelectric coefficient
d_{50}	... 50^{th} percentile of the particle size limit
d_{im}	... piezoelectric coefficient with an electrical and mechanical component in the i and m directions, respectively
DR	... deposition rate ($mm^3 \cdot min^{-1}$)
E	... electric field
E_C	... coercive field
E_i	... Young's modulus of the i^{th} layer
$G.\ O.\ F.$	... goodness of fit
h	... film thickness
N	... number of scans
N	... number of cycles, sum of the tested specimens or total number of layers
P	... electric polarization
p_i	... cumulative probability of dielectric breakdown
P_{max}	... maximum polarization
P_R	... remanent polarization
R	... bending radius
R_{exp}	... expected R-factor
R_p	... un-weighted profile R-factor
R_q	... root-mean-square roughness
R_{wp}	... weighted profile R-factor
S	... strain
$tan\ \delta$	... dielectric losses
T_C	... Curie temperature
T_{room}	... room temperature
U_{loss}	... energy-loss density
U_{rec}	... recoverable energy density
v	... sweep speed
w	... film width
y	... distance from the neutral mechanical plane
β	... shape factor, slope of the Weibull distribution
ε	... bending strain
η	... energy-storage efficiency
ν_i	... Poisson's ratio of the i^{th} layer

ψ . . . sample-tilting angle
σ . . . stress

Chapter 1

Introduction

In the Introduction a literature overview of the relevant topics for the thesis is provided. The chapter begins with a basic definition of the problem and the motivation for this work. The following section deals with a basic description of AD, which covers some technological aspects of the method and a theoretical background for the deposition mechanism. Next, piezoelectric, ferroelectric and relaxor-ferroelectric materials are presented and the physical properties of (100–x)Pb($Mg_{1/3}Nb_{2/3}$)O_3–$x$$PbTiO_3$ (PMN–100xPT) materials are explained. The chapter continues with aerosol-deposited ferroelectric films. Special attention is given to their ferroelectric behavior, which is different from the behavior of conventional bulk ferroelectrics. At the end, the objectives and hypotheses of the dissertation are presented.

1.1 Definition of the Problem

Ferroelectric ceramic components used in electronic devices are conventionally fabricated using a top-down approach. The process of producing bulk ceramics involves powder compaction, densification and subsequent shaping of the ceramic components to dimensions of the order of a few hundred µm. This approach is not suitable for ceramic components of the order of µm. However, thick-film technology, i.e., a bottom-up approach, can produce layered structures with the thickness of the functional layers being between 1 µm and 100 µm [1]. The advantage of thick-film technology is that it can fabricate complex-shaped structures in a cost-effective way [2].

The conventional thick-film deposition methods, such as screen-printing, tape casting, electrophoretic deposition and ink-jet printing, deposit ceramic thick films with relatively low green densities (from 60% to 70% of the theoretical density) [2]. Thus, the deposition of the thick films is followed by a high-temperature annealing treatment (often over 1000 °C), in order to densify the films using a sintering process [3]. However, the annealing at high temperatures imposes many drawbacks on the process. Higher annealing temperatures increase the production costs, and promote the evaporation of volatile components, which can significantly deteriorate the final chemical composition of the thick films. Furthermore, annealing at high temperatures restricts the use of substrate materials with low melting points, such as metals, polymers and glass. The integration possibilities are especially important when designing diverse applications. In order to overcome the mentioned shortcomings, another deposition method is required. Aerosol deposition (AD) has a unique deposition mechanism and is capable of producing dense, ceramic thick films at room temperature [4], [5]. The AD method differs significantly from conventional thick-film deposition methods mentioned above because the film densification in AD is basically without thermally activated processes, but happens due to the high kinetic energies involved. Any thick films deposited by AD possess special features, such as significant

internal stresses and small crystallite sizes. In the case of ferroelectric thick films, these features not only contribute to the film's constitution (physical appearance), but also alter the functional behavior. The focus of this thesis is on aerosol-deposited ceramic thick films and the effect of thermal annealing on their structural, microstructural and functional properties.

1.2 Aerosol Deposition Method

Aerosol deposition is a method for producing dense thick films on a variety of substrates at room temperature. It is a spray-coating process, where the deposition mechanism is based on the collision of fine particles with the substrate's surface. A powder with the required chemical composition is mixed with a carrier gas to form an aerosol, which is then ejected through a micro-orifice nozzle and deposited on the substrate under vacuum [4], [5]. A schematic of some typical AD apparatus is shown in Figure 1.1.

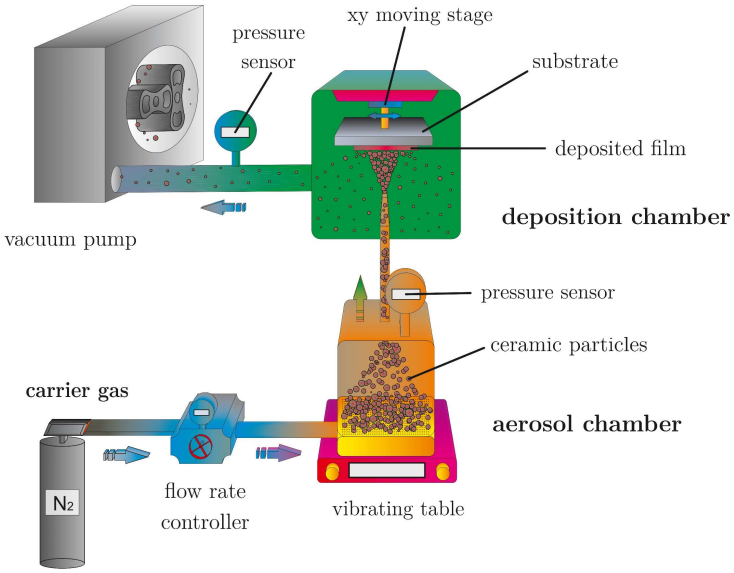

Figure 1.1: Scheme of the AD apparatus.

There are two chambers in the system: the aerosol chamber and the deposition chamber. The aerosol chamber has the function of aerosol generation, whereas in the deposition chamber the aerosol is deposited onto a substrate. For that reason, the deposition chamber is evacuated with a vacuum pump and equipped with a programmable moving stage that has a substrate holder. By passing the carrier gas in the aerosol chamber, which is positioned on a vibrating table, a fluidized bed of aerosol is produced. The connecting pipes enable the transfer of the aerosol in the evacuated deposition chamber, which occurs due to the pressure difference [4], [5]. The aerosol is accelerated when passing through the nozzle in the evacuated chamber. The focused jet of particles collides with the substrate, causing fragmentation and re-bonding to form a thick film [4].

The process parameters that can be controlled in AD are the following: the carrier-gas species, the gas consumption (i.e., gas flow rate), the distance between the nozzle and substrate, the number, velocity and length of the scans, the size of the nozzle orifice, the pressure in the deposition chambers and the pressure in the aerosol chambers. The thickness of the films is controlled by the number and velocity of the scans, although the gas flow rate also affects the deposition rate and, consequently, the final thickness. For a

setup with a fixed pipe and nozzle dimensions, varying the carrier gas (e.g., N_2, He, O_2, Air, Ar) as well as its flow rate influences the pressure in the aerosol chamber and the deposition chamber. By varying the gas flow rate between 1 L/min and 30 L/min we can control the pressure in the evacuated deposition chamber between 0.2 mbar and 20 mbar. The pressure difference between the aerosol chamber and the deposition chamber determines the velocity of the aerosol jet (ranging between 100 m/s and 600 m/s) and the kinetic energies of the impacting particles [6]. It is common to use converging nozzles with a narrow orifice, having a typical slit width between 0.2 mm and 0.8 mm. The flow and the velocity of the aerosol jet also depends on the nozzle geometry [5].

The materials that have typically been deposited by AD are ceramic materials. These can be divided into simple oxides (Al_2O_3 [7], TiO_2 [8], Y_2O_3 [9], yttria-stabilized zirconia (YSZ) [10], ZnO [11]), perovskites ($Pb(Zr,Ti)O_3$ (PZT) [4], [12], $BaTiO_3$ [13], $LaNiO_3$ [14], $MgTiO_3$ [15], $(La_{0.8}Sr_{0.2})MnO_3$ [16], $(La_{0.6}Sr_{0.4})(Co_{0.2}Fe_{0.8})O_3$ [17], $BaZr_{0.8}Y_{0.2}O_3$ [18], $(K,Na)NbO_3$ [19]–[21], $BiFeO_3$ [22], PMN–100xPT [23] and other ceramics ($CuFeO_2$ [24], NiZnCu-Fe_2O_3 [25], $NiMn_2O_4$ [26], $Ca_{10}(PO_4)_6(OH)_2$ [27], AlN [28]). However, AD is not limited to ceramics, as metal materials can also be deposited, e.g., Ag [29], $Bi_{0.4}Sb_{1.6}Te_3$ [30], $Nd_{4.5}Fe_{73}Co_2Cr_2B_{18.5}$ [31], $Sm_2Fe_{17}N_3$ [32]. A great advantage of the AD method is the combination of different materials in the deposition simultaneously. This is called aerosol co-deposition, which was used to deposit different composites, like ceramic/ceramic (e.g., $BaTiO_3/Al_2O_3$ [33]), ceramic/metal (e.g., $BaTiO_3$/Al [34]) and ceramic/organic composites (e.g., $Ca_{10}(PO_4)_6(OH)_2$/chitosan [35])

Furthermore, AD provides an appropriate way to coat these materials on a variety of substrates. The substrates that were already used for AD can be divided into: i) ceramics, e.g., Al_2O_3 [36], [37] and low-temperature co-fired ceramics [38], [39]; ii) metals, e.g., stainless steel (SS) [40], [41], Cu [13], [42], Pt [43], Au [44], Al [45]; iii) polymers [46], [47] and iv) others, such as glass [37], [48] or Si [49], [50].

To summarize, with the AD method it is possible to combine ceramics, metals and polymers in order to prepare thick-film structures for various applications. While the topic of the thesis is oriented towards functional ceramic thick films, the AD process of ceramic thick films and their properties will be discussed further on.

1.2.1 Ceramic Thick Films Prepared by Aerosol Deposition

For the AD of ceramic thick films, it is very important to control the material parameters, such as the properties of the ceramic powders [51]. In contrast to metal particles, which are ductile and deform plastically during the collision with the substrate, the ceramic particles are brittle, thus the plastic deformation is often accompanied by fracture [5]. As shown in Figure 1.2, smaller ceramic particles ($<<$ 0.1 µm) ejected from the nozzle have a lower kinetic energy and can be deflected (by the bow shocks) or rebound elastically from the substrate/film. Medium-sized ceramic particles have an appropriate kinetic energy and are deposited due to the plastic deformation and fracturing. Larger ceramic particles ($>>$ 10 µm) obtain a too high kinetic energy, which causes abrasive blasting of the substrate/film [5]. Thus, the proposed deposition mechanism is based on the ceramic particle cracking and deformation, which occurs due to a hammering effect of the subsequent particle bombardment [52].

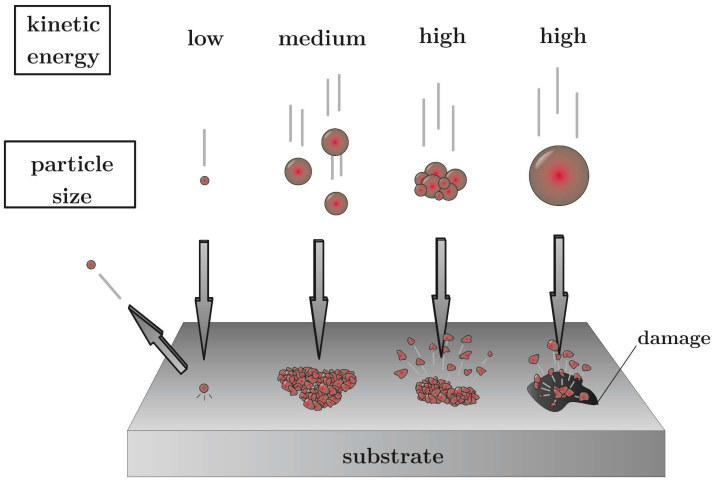

Figure 1.2: Schematic representation of different sized ceramic particle collisions that take place during the AD process. A successful deposition of appropriate (medium) sized particles happens due to ceramic particle cracking and deforming.

The particles' deposition efficiency is not just size dependent; it also depends on the ceramic particles' hardness, fracture toughness, density and state of agglomeration. Small, sub-µm-sized particles agglomerate due to their high specific surface energy. An agglomerate is a larger unit, which comprises loosely bonded particles. The degree of agglomeration does not influence just the deposition efficiency of the powder, but also the distribution of the particles lifted in the aerosol. Agglomerates behave differently when hitting the substrate/film surface than primary particles (of the same size). They presumably crash into smaller, loose particles, which are not able to bond to the substrate/film surface (Figure 1.2) [5]. An appropriate ceramic particle size range that is suitable for aerosol generation and deposition is estimated to be between 0.2 µm and 2 µm [5], [37]. To control the powder parameters such as powder particle size distribution, state of agglomeration, surface morphology and crystallite size, the powder is often treated prior to AD. The treatment of the powder usually involves heating to the temperatures of partial sintering, milling, sieving and drying [51], [53], [54]. Heating of the powders was proven to be essential in ensuring the adequate crystallinity and growth of crystallites. Only sufficiently large crystallites can undergo fracturing and plastic deformation, which is a prerequisite for successful powder deposition [55]. The powder milling reduces the particle size, while preserving the crystallite size. The milling is therefore used to increase the deposition rate, but progressive milling can also lead to insufficient particle compaction and increase the porosity of the deposited films, as reported by Akedo and Lebedev [54].

AD ceramic thick films exhibit some special characteristics. The typical films (Figure 1.3(a)) are dense (over 95% of theoretical density [56]) with nm-sized pores [57], [58] and with a good adhesion to the substrate [4]. The reason for the high density can be found in the kinetic energy of the high-speed particles, as already discussed. The high kinetic energy causes an intensive solidification when impacting with the substrate. Since the deposition occurs at room temperature, the bonding of the particles does not occur because of the thermal energy, but as a consequence of a sufficiently high kinetic energy. In studies where the particle collisions were modelled, it was shown that the local maximum temperature of the particles does not exceed 330 °C, which is far below the ceramics' melting point [6], [59].

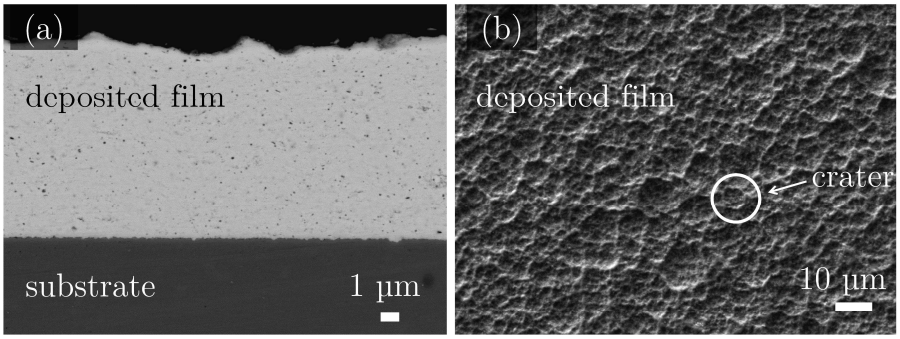

Figure 1.3: Scanning electron microscope images of AD $0.9Pb(Mg_{1/3}Nb_{2/3})O_3$–$0.1PbTiO_3$ thick films on SS substrates in (a) cross-section and (b) surface (plain) view. An example of a crater is marked with a white circle.

The microstructure of the ceramic films shows non-distinctive grains reaching a few tens of nm in diameter [4], [57]. The impact of the ceramic particles does not just make the films dense; it also significantly increases the internal stress, which can be of the order of GPa [60], [61]. Usually, after the deposition the crystallographic phase is preserved and the crystallite size is reduced compared to the initial particles [50]. AD films also exhibit a relatively rough surface (Figure 1.3(b)). The root-mean-square values of the roughness (R_q) are usually in the range of a few hundred nm [48].

1.3 Piezoelectrics, Ferroelectrics and Relaxor Ferroelectrics

1.3.1 Piezoelectrics and Ferroelectrics

Electro-mechanical devices, such as sensors, actuators and ultrasonic transducers, often consist of functional materials that exhibit a piezoelectric effect. Piezoelectrics are materials that can develop a dielectric displacement when a mechanical stress is applied (direct piezoelectricity, equation (1.1)) and mechanical deformation when an external electric field is applied (converse piezoelectricity, equation (1.2)). The direct and converse piezoelectric effects are schematically illustrated in Figure 1.4(a) and can be written in matrix form as:

$$D_i = d_{im}\ \sigma_m \tag{1.1}$$

$$S_m = d_{im}\ E_i \tag{1.2}$$

where D, S, σ, E, d are the dielectric displacement ($C{\cdot}m^{-2}$), strain (/), stress ($N{\cdot}m^{-2}$), electric field ($V{\cdot}m^{-1}$) and piezoelectric coefficient ($C{\cdot}N^{-1}$ or $m{\cdot}V^{-1}$), respectively [62].

Piezoelectricity can only be exploited in crystals that do not have a center of symmetry. Out of 32 crystal classes, 21 of them exhibit non-centrosymmetry and 20 of them exhibit piezoelectricity. Piezoelectrics are further divided into pyroelectrics (10 crystal classes), which exhibit a spontaneous polarization (i.e., a permanent electrical dipole at the unit-cell level) in the absence of an external electric field. Pyroelectrics can also change their polarization with the temperature, which is known as pyroelectricity. Moreover, a subgroup of pyroelectrics are ferroelectrics. They possess at least two equilibrium orientations of the spontaneous polarization, which can be switched by an external electric field [62], [63]. The

hierarchical subdivision of piezoelectrics into ferroelectrics is schematically presented in Figure 1.4(b).

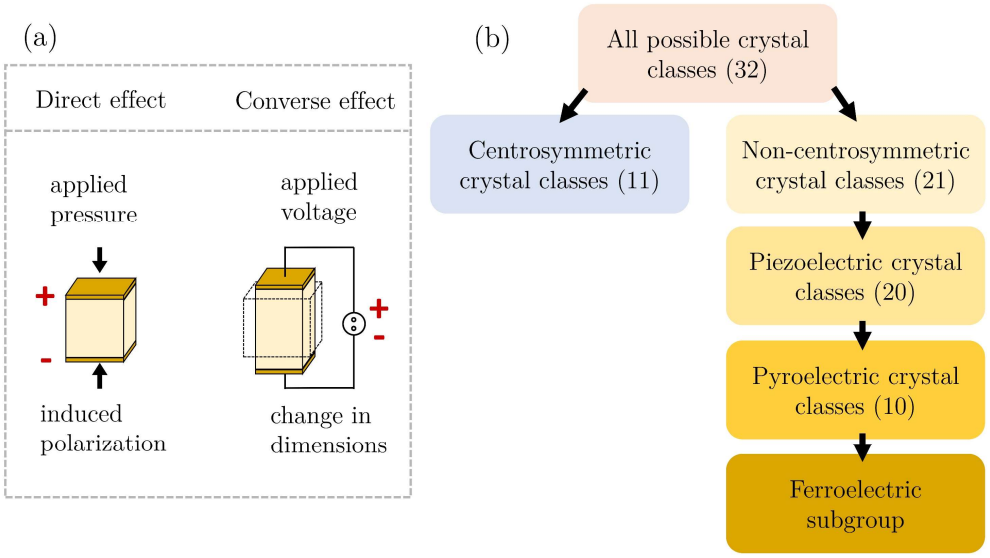

Figure 1.4: (a) Schematic of the direct and converse piezoelectric effects and (b) the hierarchical subdivision of piezoelectric materials.

The ferroelectric properties of crystals at the unit-cell level are often presented using the example of a perovskite (ABO_3) crystal structure (Figure 1.5). Above the Curie temperature (T_C) such materials are in a paraelectric (non-polar) phase, while below T_C they are in a ferroelectric (polar) phase. The paraelectric phase is centrosymmetric and always has a higher symmetry than the low-temperature ferroelectric phase, which exhibits spontaneous polarization (Figure 1.5) [62], [64]. At the microscopic level the regions of uniform spontaneous polarization are called the ferroelectric domains, which can be aligned in a certain direction with the application of an external electric field. The ferroelectric domains are separated by domain walls. The phase transition at T_C in ordinary ferroelectrics is accompanied by a sharp maximum in the dielectric permittivity vs. temperature dependence (Figure 1.5(a)). Furthermore, ferroelectric materials exhibit a typical electric polarization (P) vs. electric field (E) behavior, which is a consequence of domain switching (shown in Figure 1.5(b)) [62].

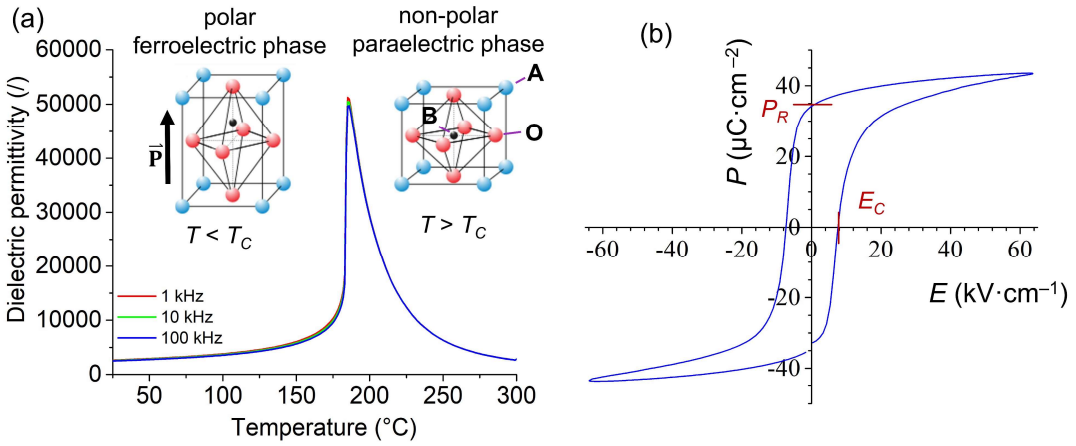

Figure 1.5: (a) Temperature dependence of the dielectric permittivity around T_C and (b) characteristic P–E hysteresis loop of a ferroelectric, with a perovskite crystal structure (ABO_3). The remanent polarization (P_R) is the polarization that persists when an external electric field is removed. The coercive field (E_C) is the electric field that reduces the polarization to zero. The schematics in panel (a) are modified after [65] and the graphs are courtesy of the Electronic Ceramics Department, JSI.

1.3.2 Relaxor-Ferroelectrics

In contrast to classic ferroelectrics, relaxor-ferroelectrics, or briefly relaxors, do not exhibit a long-range-ordered ferroelectric phase and their symmetry remains, on average, cubic down to very low temperatures. Relaxors are chemically (or compositionally) disordered, meaning that in the unit cell equivalent lattice sites are occupied by different cations in a random order [66]. Such chemical disorder creates randomly oriented dipoles with the associated local random fields, even in the paraelectric state [66], [67]. By cooling down from the paraelectric state, an (ergodic) relaxor state appears, which contains polar regions on the nm scale (called the polar nano region – PNR) [66], [68]. In the absence of an external electric field the polarization of the PNR is random and the macroscopic spontaneous polarization is zero. However, when applying an external electric field, the dipoles in the PNR become oriented [69]. Relaxors exhibit a broad and frequency-dependent dielectric permittivity vs. temperature maximum and rather slim P–E loops, as shown in Figure 1.6(a) and (b), respectively [66].

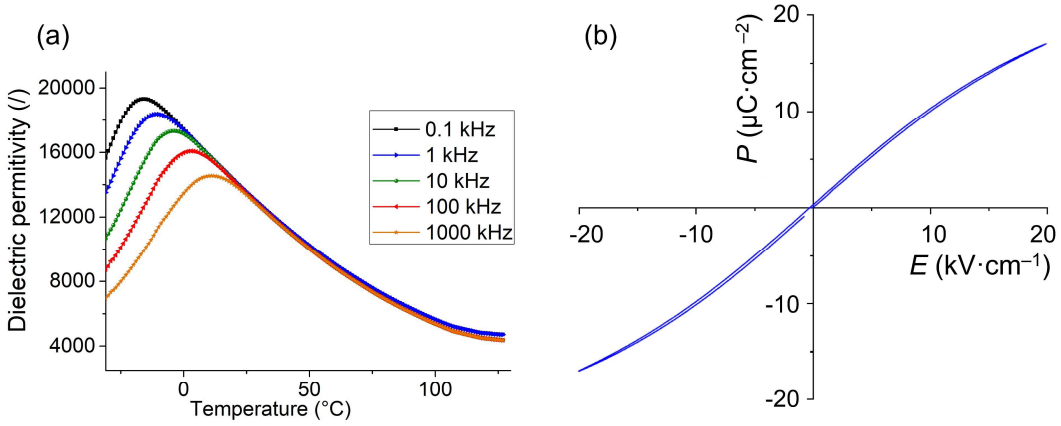

Figure 1.6: (a) Temperature dependence of the dielectric permittivity and (b) *P*–*E* hysteresis loop (at 1 kHz) of $Pb(Mg_{1/3}Nb_{2/3})O_3$ ceramics, which is a prototype relaxor. Courtesy of Electronic Ceramics Department, JSI.

1.3.3 $Pb(Mg_{1/3}Nb_{2/3})O_3$–$PbTiO_3$ Solid Solutions

One of the most studied relaxors is the perovskite lead magnesium niobate $Pb(Mg_{1/3}Nb_{2/3})O_3$ (PMN). Its chemical disorder, which is typical for relaxors, originates from the B-site Mg^{2+} and Nb^{5+} ions (with a stoichiometric ratio of 1:2). The occupancy of Mg^{2+} and Nb^{5+} ions is random, with the exception of the chemically ordered nm-sized regions [70], [71]. However, such a complex order/disorder local structure disturbs the long-range order typical for ferroelectrics and leads to the formation of PNR [72], [73]. Therefore, the nm-sized domain pattern and the absence of long-range ferroelectric order give rise to the characteristic relaxor behaviour shown in Figure 1.6.

On the other hand, the $PbTiO_3$ (PT) is ferroelectric, having a tetragonal crystal structure at room temperature. It shows a typical ferroelectric *P*–*E* hysteresis loop and a frequency-independent permittivity peak at $T_C = 495$ °C [74].

Together, the PMN and PT form a solid solution $(1\text{-}x)Pb(Mg_{1/3}Nb_{2/3})O_3$–$xPbTiO_3$ (PMN–100*x*PT) over the entire compositional range [75]. According to the binary phase diagram (shown in Figure 1.7) at room temperature (T_{room}), multiple phases exist between the cubic (*Pm-3m*) PMN and tetragonal PT (*P4mm*). With increasing PT content, the cubic phase first transforms to a "pseudo-rhombohedral" (*R3m*) phase (observed in single crystals) or distorted monoclinic (*Cm*) phase (observed in ceramics) and then to a monoclinic (*Cm*) and monoclinic (*Pm*) [76]. As expected, the increasing PT content gradually suppresses the relaxor behavior ($0 < x < 0.1$) and at $x > 0.30$ the ferroelectric behavior prevails [66], [77], [78]. The PMN–100*x*PT system shows a so-called morphotropic phase boundary (MPB) at $x \sim 0.35$, where monoclinic and tetragonal phases coexist. The compositions in the MPB region are characterized by promising ferroelectric properties. Thus the PMN–35PT (blue dotted vertical line shown in Figure 1.7) possesses excellent dielectric and piezoelectric properties, i.e., the longitudinal piezoelectric coefficient (d_{33}) of bulk ceramics typically reaches more than 500 $pC{\cdot}N^{-1}$ [77], [79]–[81]. On the other hand, compositions with a low PT content, like PMN–10PT (red dotted vertical line shown in Figure 1.7), exhibit small hysteretic losses (evident from the slim *P*–*E* loops) and exceptional electrocaloric properties [82]–[85], and so have potential in capacitive energy-storage and solid-state cooling technologies.

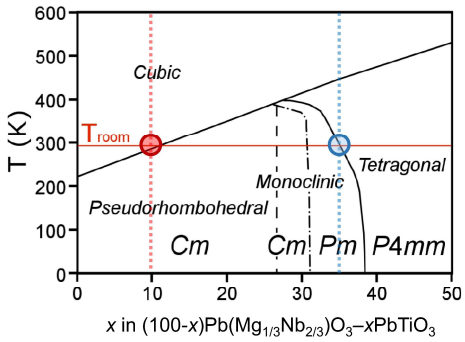

Figure 1.7: PMN–100xPT phase diagram. Modified after [76], [86].

1.4 Ferroelectric Ceramic Thick Films Prepared by Aerosol Deposition

Aerosol deposition is a promising method for the fabrication of ferroelectrics in the form of thick films. Most of the research on AD ferroelectrics has been conducted on lead zirconate titanate ($Pb(Zr,Ti)O_3$, PZT), as it offers excellent ferroelectric and piezoelectric properties. In addition, diverse chemical modifications of the PZT system make it possible to tailor its properties, which is beneficial when engineering various devices [87]. The applicability of aerosol-deposited PZT thick films was demonstrated in micro-electromechanical systems, such as micro-actuators [88]–[90], ultrasonic transducers [91], electro-optical modulators [92]–[94] and energy harvesters [95]–[97]. In recent years, more attention has been given to demonstrate the capacitive energy-storage capabilities of aerosol-deposited PZT thick films [98]–[102]. However, PZT is not the only ferroelectric material being prepared using the AD method. Other ferroelectrics include, e.g., $BaTiO_3$ [41], [103]–[106], $(K,Na)NbO_3$ [19]–[21], $BiFeO_3$ [22] and PMN–100xPT [23], [107], [108].

The microstructure of AD ferroelectric thick films is different compared with the bulk ferroelectrics prepared by conventional ceramic sintering. The as-deposited ferroelectric films have an increased amorphous content and a reduced crystallite size [50]. As mentioned earlier, the impact of the ceramic particles also increases the internal stresses in the material [60]. The consequences of such microstructural characteristics are poor dielectric, piezoelectric and ferroelectric properties of the as-deposited films. For example, the dielectric permittivity (measured at 1 kHz) of as-deposited $Pb(Zr_{0.52}Ti_{0.48})O_3$ thick films on Si substrates is low (~100) in comparison to their bulk counterparts (~1200) [109]. In addition, the P–E loops of the as-deposited $Pb(Zr_{0.52}Ti_{0.48})O_3$ films do not show typical ferroelectric hysteresis loops, but almost a linear behaviour, as shown in Figure 1.8 [109].

In order to improve the functional properties, the AD films are usually annealed above 500 °C after the deposition [12], [19], [22], [50], [104], [109]–[111]. However, low temperatures of 300 °C can also be used in the post-deposition annealing [60]. Depending on the temperature, the annealing increases the crystallinity and the crystallite size [50], and relaxes the internal stresses [41], [60], which leads to improved dielectric, piezoelectric and ferroelectric properties. For example, in $BaTiO_3$ thick films on stainless steel (SS) after annealing at 300 °C (500 °C) the compressive residual stress relaxes from 672 MPa to 319 MPa (271 MPa), and the maximum polarization at 500 $kV{\cdot}cm^{-1}$ increases from 3.3 $\mu C{\cdot}cm^{-2}$ to 5.0 $\mu C{\cdot}cm^{-2}$ (5.8 $\mu C{\cdot}cm^{-2}$) [60]. In this case, the annealing temperatures of

500 °C were too low to cause any crystallite growth. A further increment in the annealing temperature improves the functional properties even more. The enhancement of the ferroelectric character is especially obvious from the *P*–*E* hysteresis loops. In $Pb(Zr_{0.52}Ti_{0.48})O_3$ thick films on Si substrates the maximum polarization at 500 kV·cm^{-1} increases from 7.7 µC·cm^{-2} to 48.3 µC·cm^{-2} and 66.6 µC·cm^{-2}, when the annealing temperature increases from 500 °C to 700 °C, respectively (Figure 1.8) [109]. Note that above 500 °C the grain growth becomes a significant factor in the improvement of the functional properties.

Furthermore, the high density and low pore concentration of the AD thick films contribute to an extremely high dielectric breakdown strength (DBS). In general, the DBS's characteristics are independent of the post-deposition thermal annealing temperatures, since the annealing does not change the film density. For example, the DBS of AD $(Pb_{0.89}La_{0.11})(Zr_{0.70}Ti_{0.30})O_3$ thick films can reach 3000 kV·cm^{-1} [100], which is much higher than their bulk counterparts, with a DBS of ~80 kV·cm^{-1} [112].

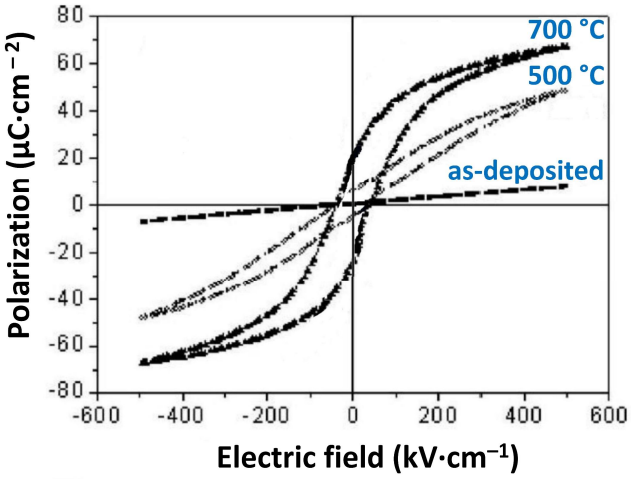

Figure 1.8: *P*–*E* hysteresis loops of AD $Pb(Zr_{0.52}Ti_{0.48})O_3$ thick films on Si substrates annealed at different temperatures. Modified after [109].

Ferroelectric materials are promising as piezoelectrics and therefore their electromechanical properties are also investigated in thick-film form. However, the piezoelectric effect in aerosol-deposited thick films is typically much lower than that of bulk ceramics. For example, it was shown that the film-substrate clamping effect remarkably reduces the maximum piezoelectric strain output of aerosol-deposited PZT thick films [113]. More studies have shown that the measured piezoelectric coefficient also depends on the thermal expansion mismatch between the film and the substrate [114] and on the thickness of the annealed aerosol-deposited films [115]. Han et al. demonstrated an increasing converse piezoelectric coefficient d_{33} with increasing the film's thickness (between 1 µm and 55 µm) [115].

Since aerosol-deposited ferroelectric thick films already have a high (green) density, no densification is required, only stress relaxation, crystallization and crystal growth. Thus, the temperatures for annealing the AD ferroelectric films are a few hundred degrees lower than the temperatures for sintering low-density thick films prepared by other methods. For example, screen-printed ferroelectric thick films often need to be densified at temperatures above 1000 °C [116], [117], while AD ferroelectric thick films can exhibit ferroelectric-like properties after annealing at 300 °C [60]. The advantage of the AD method is, therefore, the integration of thick films onto a wider collection of substrates.

Metal substrates offer good electrical conductivity and mechanical stability, while polymer substrates offer flexibility, bendability and pliability, making them a promising choice for flexible electronics [118], [119]. SS represents a versatile metal, durable and resistant to corrosion and wear. As a low-cost material it is in everyday use. When using flexible polymers as substrates, polyimide (PI) is often chosen as it offers excellent chemical resistance and thermal stability [120]. However, little research has been done on the integration of ferroelectric ceramic thick films on PI substrates [99].

Despite huge efforts that have been made with the AD of ferroelectrics, most of the studies have been conducted on PZT thick films (starting with Akedo et al. in 1999 [40], [50]), while little attention was given to the PMN–100xPT system [23], [107], [108]. Moreover, there is only one research group working on aerosol-deposited PMN–100xPT thick films on low-cost substrates such as SS [107] and none on flexible polymer substrates.

1.5 Objectives and Hypotheses of the Dissertation

Due to the room-temperature deposition, the AD method is a great option to integrate ceramics with a variety of low-melting-point substrates. The potential for developing new material combinations is huge, as well as being important for designing diverse applications (e.g., capacitive energy storage, energy harvesting, high-power electronics, actuators and sensors).

The main goal of the thesis is to prepare functional (1-x)Pb($Mg_{1/3}Nb_{2/3}$)O_3–$x$$PbTiO_3$ (PMN–100xPT) thick films using the AD method on stainless-steel (SS) and polyimide (PI) substrates. Furthermore, the purpose is to evaluate the influence of the post-deposition thermal annealing on the structural, microstructural and functional properties of the prepared films.

The objectives of this doctoral dissertation are the following:

1) To find the relation between the PMN–10PT and PMN–35PT powder-preparation procedure, particle properties and the powder-deposition efficiency during AD.
2) To integrate PMN–10PT and PMN–35PT thick films on substrates, incompatible with a high-temperature sintering process, such as on SS and PI substrates.
3) To deposit homogeneous PMN–10PT and PMN–35PT thick films with a relative density above 97%.
4) To determine the influence of thermal annealing on the structure and microstructure of PMN–10PT and PMN–35PT thick films, and consequently on their functional properties, i.e., dielectric, ferroelectric, energy-storage and electromechanical properties.
5) To evaluate the degree of stress relaxation during the thermal annealing of prepared thick films at different annealing temperatures.
6) To prepare PMN–10PT and PMN–35PT thick films with a high dielectric breakdown strength (DBS), which leads to a high energy-storage density.
7) To investigate the bendability of ceramic PMN–10PT thick films deposited on flexible PI substrates.
8) To determine the electromechanical properties of PMN–35PT thick films deposited using AD.

This doctoral dissertation is based on the following hypotheses:

1) PMN–10PT and PMN–35PT powders with particle sizes less than 100 nm are not suitable for the aerosol deposition of thick films because small particles do not undergo typical fragmentation and re-bonding. In addition, the presence of

agglomerates can hinder the deposition of films with a homogeneous film thickness. Only powders with particles in the range of several hundred nm can form dense, homogeneous, few-µm-thick films with good adhesion.

2) PMN–10PT and PMN–35PT powders, after mechanochemically assisted synthesis, consists of nanocrystalline particles; therefore, thermal annealing of the powder, which increases the particle size, is required for successful film deposition on SS and PI substrates.
3) The microstructure of PMN–10PT and PMN–35PT thick films does not change significantly with a post-deposition thermal annealing up to 500 °C.
4) The stress relaxation after the post-deposition thermal annealing of PMN–10PT and PMN–35PT thick films is significant and improves their functional properties.
5) The DBS of aerosol-deposited thick films is higher than that of bulk ceramics. Moreover, the dielectric breakdown characteristics of PMN–10PT and PMN–35PT thick films do not change after post-deposition thermal annealing due to the preserved microstructure.
6) Compared to their bulk-ceramic counterparts, the aerosol-deposited PMN–10PT and PMN–35PT thick films exhibit higher polarization and energy-storage properties.
7) The AD method enables the preparation of PMN–10PT and PMN–35PT thick films on SS with a high electrical fatigue stability, i.e., they withstand more than one million cycles of applied electric field.
8) The aerosol-deposited PMN–10PT thick films on PI substrates are flexible and durable, and can withstand bending up to a radius of 3 mm and repetitions of 10^5 bending cycles without degradation of the energy-storage performance.
9) Using the AD method, piezoelectrically active PMN–35PT thick films can be produced entirely at room temperature. Additional thermal annealing of the thick films increases their piezoelectric response.

Chapter 2

Energy-Storage-Efficient $0.9Pb(Mg_{1/3}Nb_{2/3})O_3$–$0.1PbTiO_3$ Thick Films Integrated Directly onto Stainless Steel

To overcome the obstacles in integrating functional ceramics with metals, a room-temperature AD method was employed. Relaxor-ferroelectric PMN–10PT thick films were aerosol-deposited on low-cost SS substrates to produce energy-storage-efficient thick films.

First, a single-phase PMN–10PT powder was prepared by mechanochemical-activation-assisted synthesis. Heating and planetary ball milling were introduced to the powder and four powder modifications were prepared by varying the heating and milling conditions. To investigate the influence of powder properties on the aerosol deposition behavior, the surface morphology, state of agglomeration and particle size of all four PMN–10PT powder modifications were studied. The first part of our study demonstrated how critical powder preparation is to successful AD. A combination of heating (at 900 °C) and subsequent milling (for 30 min) proved to be important to obtain a PMN–10PT powder with sufficiently large crystallites (181 nm) and an optimized particle size to allow the formation of dense and homogeneous thick films at an increased deposition rate ($0.27\ mm^3 \cdot min^{-1}$).

Due to the typical deposition mechanism of AD, the crystallite size of the aerosol-deposited PMN–10PT thick films on SS substrates decreased to 33 nm ± 1 nm, and the microstrain increased significantly to $25.9 \cdot 10^{-4} \pm 0.3 \cdot 10^{-4}$. Furthermore, the as-deposited thick films were additionally annealed at 500 °C, and the effect of thermal annealing on the structural, microstructural, and energy-storage properties of the PMN–10PT films was investigated. Thermal annealing does not lead to any microstructural changes; the high density (porosity of only ~1.5%) and excellent adhesion are maintained. After thermal annealing, the crystallite size remained similar, while the microstrain decreased by 47%, indicating a partial relaxation of the residual stresses. The stress relaxation is responsible for the evolution of dielectric behavior (in as-deposited films) to relaxor-ferroelectric behavior in thermally annealed PMN–10PT thick films. As a result of the slim *P*–*E* hysteresis loops and high DBS, the thermally annealed films achieve a recoverable energy-storage density (U_{rec}) of $9.8\ J \cdot cm^{-3}$ and an energy-storage efficiency (η) of 79% at $900\ kV \cdot cm^{-1}$. These results are comparable to other energy-storage-efficient thick films prepared by AD on conventional Si substrates. The excellent temperature stability of the energy-storage properties up to 200 °C and the electric-field cycling stability up to $1.6 \cdot 10^7$

cycles make thermally annealed PMN–10PT thick films promising for energy-storage applications.
This chapter addresses thesis objectives 1, 2, 3, 4, 5, and 6.

Published in: M. Sadl, O. Condurache, A. Bencan, M. Dragomir, U. Prah, B. Malic, M. Deluca, U. Eckstein, D. Hausmann, N. H. Khansur, K. G. Webber, and H. Ursic, "Energy-storage-efficient $0.9Pb(Mg_{1/3}Nb_{2/3})O_3$–$0.1PbTiO_3$ thick films integrated directly onto stainless steel," *Acta Mater.*, vol. 221, p. 117403, 2021. (IF = 9.209, 2021)

My contribution: I synthesized the powder and prepared the powder modifications after heating and milling. I optimized the process parameters for the aerosol-deposition process and deposited the thick-film samples on the SS. I performed surface profilometry, scanning electron microscopy, laser granulometry, X-ray diffraction data (XRD) analysis, electrical and impedance characterization and the calculation of the energy-storage properties. I elaborated the concept of the manuscript and wrote the paper, together with the co-authors.

Acta Materialia 221 (2021) 117403

Contents lists available at ScienceDirect

Acta Materialia

journal homepage: www.elsevier.com/locate/actamat

Full length article

Energy-storage-efficient $0.9Pb(Mg_{1/3}Nb_{2/3})O_3$–$0.1PbTiO_3$ thick films integrated directly onto stainless steel

Matej Sadl[a,b], Oana Condurache[a,b], Andreja Bencan[a,b], Mirela Dragomir[a], Uros Prah[a,b], Barbara Malic[a,b], Marco Deluca[c], Udo Eckstein[d], Daniel Hausmann[e], Neamul H. Khansur[d], Kyle G. Webber[d], Hana Ursic[a,b,*]

[a] Electronic Ceramics Department, Jožef Stefan Institute, Jamova cesta 39, 1000 Ljubljana, Slovenia
[b] Jožef Stefan International Postgraduate School, Jamova cesta 39, 1000 Ljubljana, Slovenia
[c] Materials Center Leoben Forschung GmbH (MCL), Roseggerstrasse 12, 8700 Leoben, Austria
[d] Department of Materials Science and Engineering, Friedrich-Alexander-Universität Erlangen-Nürnberg (FAU), 91058 Erlangen, Germany
[e] Institute of General Material Properties, Friedrich-Alexander-Universität Erlangen-Nürnberg (FAU), 91058 Erlangen, Germany

ARTICLE INFO

Article history:
Received 3 March 2021
Revised 20 September 2021
Accepted 12 October 2021
Available online 18 October 2021

Keywords:
Thick film
Aerosol deposition
Low-temperature processing
Energy storage
PMN–PT
Relaxor-ferroelectric
Stainless steel

ABSTRACT

The integration of functional ceramics with metals remains challenging due to the thermally activated processes and the incompatibilities that arise during the high-temperature ceramic sintering process. In order to overcome this, low-temperature processing methods can be employed. In this work, dense $0.9Pb(Mg_{1/3}Nb_{2/3})O_3$–$0.1PbTiO_3$ thick films were deposited on low-cost, stainless-steel substrates at room temperature using an aerosol-deposition method. The key material parameters for a successful aerosol deposition of the powder were identified and used in the process, which resulted in homogeneous 15-µm-thick films. The as-deposited films can withstand electric fields of 900 $kV{\cdot}cm^{-1}$ and exhibit promising room-temperature energy-storage properties: the recoverable energy density reaches 7.0 $J{\cdot}cm^{-3}$ with an energy-storage efficiency of ~70%. A post-deposition stress relaxation by annealing at 500°C further improves the recoverable energy density, leading to 9.8 $J{\cdot}cm^{-3}$ at 900 $kV{\cdot}cm^{-1}$ with an energy-storage efficiency of ~80%. The energy-storage performance exhibits excellent temperature stability up to 200°C and an electric-field cycling stability up to 16 million cycles. The low-temperature integration of energy-storage-efficient thick films onto stainless steel opens up possibilities for numerous new, pulsed-power and power-conditioning electronic applications.

1. Introduction

Ceramic dielectric capacitors can absorb and release large voltage or current pulses in a short timeframe (i.e., between µs and ms), making them promising for energy-storage devices in pulsed-power and power-conditioning electronic applications. These can be found in medical equipment, transportation, avionics, energy systems such as photovoltaics and other commercial systems [1–3]. Ceramic dielectric capacitors, however, possess energy-density values some orders of magnitude lower than supercapacitors or batteries. Increasing the energy density of ceramic dielectric capacitors might thus open up possibilities for new applications in which they could – at least partly – replace long-term, energy-storage devices. Dense materials in the form of films with thicknesses around or above 1 µm show the most promising energy-storage properties so far [4].

The materials used for capacitors in energy-storage applications need to operate under demanding conditions such as high electric fields, a broad temperature range and they need to endure repetitive electric-field cycling. Ceramic thick films based on relaxor-ferroelectrics $(1-x)Pb(Mg_{1/3}Nb_{2/3})O_3$–$xPbTiO_3$ (PMN–100*x*PT) cope well with all these requirements. Among them, PMN–10PT is interesting for such applications as it exhibits small hysteresis losses, which is evident from the slim electric polarization (P) vs. electric field (E) hysteresis loops [5]. The requirements for a large dielectric-breakdown strength of ceramics can be achieved by increasing the material's density and reducing the thickness of the capacitor. As such, dense PMN–10PT thick films have excellent possibilities to achieve a high energy-storage performance in layered ceramic dielectric capacitors.

* Corresponding author.
E-mail address: hana.ursic@ijs.si (H. Ursic).

https://doi.org/10.1016/j.actamat.2021.117403

Conventional thick-film deposition methods, such as screen-printing, tape-casting or electrophoretic deposition, are followed by a high-temperature annealing (often above 1000 °C) to densify the deposited films [6]. However, annealing at such high temperatures imposes many drawbacks. High annealing temperatures increase the production costs and promote the evaporation of volatile components, which can significantly deteriorate the chemical composition of functional layers. Furthermore, annealing at high temperatures restricts the use of substrate materials with a low oxidation resistance and a low melting point, such as metals. This limits the integration possibilities of ceramic layers on metal substrates, which is especially important when designing new applications [6]. In order to overcome these shortcomings, aerosol deposition (AD) can be used. AD is a spray-coating method for preparing dense, several-µm-thick films at room temperature. The deposition mechanism is based on the collision of high-speed particles with the substrate's surface and the densification occurs as a consequence of the high kinetic energies involved [7,8].

Stainless steel is an iron-based alloy containing chromium, which makes it durable and resistant to corrosion and wear. It is a low-cost material that is used in various applications, e.g., in buildings and monuments, manufacturing, medicine, power stations, vehicles, spacecraft and many other appliances and consumer products [9–11]. The integration of functional layers directly onto stainless-steel surfaces is a very important scientific and technological challenge with enormous potential for applications. The processing and characterization of piezoelectric Pb(Zr,Ti)O_3-based [12–16] and lead-free [17–19] thick films on stainless steel have been widely reported; however, no reports of energy-storage-efficient PMN-based thick films on stainless steel are available.

In this work, PMN–10PT thick films were directly deposited by AD on stainless-steel substrates without any additional intermediate layers (electrodes or barrier layers). For the successful deposition of films by AD, the powder properties need to be optimized. According to the literature [8], powders with a particle size ranging between 0.2 µm and 2 µm can be successfully deposited by AD. However, the deposition is not just particle-size dependent; it also depends on the particles' shape, state of agglomeration, hardness, average crystallite size, etc. [8,20,21]. Milling and thermal pre-treatment of the powder are thus crucial for an efficient film deposition. This work investigates the influence of PMN–10PT powder properties on the deposition rate. Four different PMN–10PT powders were prepared and deposited on the stainless-steel substrates. The optimum powder resulted in dense films that were a few µm thick.

According to reports in the literature, the impact of ceramic particles during the AD process creates internal stresses in the deposited material [19,22,23]. The post-deposition annealing of prepared films will induce an increase in the size of the crystallites [24] and the relaxation of internal stresses [19,25], which can lead to improved functional properties. Therefore, in the second part of this work, the influence of thermal annealing on the structural, microstructural and energy-storage properties of PMN–10PT thick films on stainless-steel substrates is discussed.

2. Experimental procedure

For the synthesis of the PMN–10PT ceramic powder, PbO (99.9%, Aldrich), MgO (99.95%, Alfa Aesar), TiO_2 (99.8%, Alfa Aesar) and Nb_2O_5 (99.9%, Aldrich) were employed. Two sets of oxide mixtures corresponding to the stoichiometry of Pb($Mg_{1/3}Nb_{2/3}$)O_3 and $PbTiO_3$ were homogenized separately. The PT powder mixture was calcined at 750°C for 2 h and additionally milled in order to obtain crystalline PT seeds. It was reported that such PT seeds facilitate faster kinetics of the PMN–10PT perovskite-phase formation and shorten the high-energy milling time [26]. PT and PMN powder mixtures were homogenized with a stoichiometry of 0.9Pb($Mg_{1/3}Nb_{2/3}$)O_3–0.1$PbTiO_3$. This mixture was reacted by mechanochemical-activation-assisted synthesis, also known as high-energy milling, after which the synthesized powder was milled. All homogenization and milling processes were carried out in a planetary ball mill (PM 400, Retsch, Germany) at 200 min^{-1} for 2 h, in isopropanol, using yttria-stabilized zirconia (YSZ) milling balls with diameters of 3 mm. The high-energy milling involved the same planetary ball mill, but for 36 h at 300 min^{-1} in a tungsten-carbide milling vial with a volume of 250 cm^3, filled with 10 tungsten-carbide milling balls having diameters of 20 mm. In addition to the thick films, the PMN–10PT bulk ceramic pellets with an average grain size of 4.4 µm were prepared via mechanochemical-activation-assisted synthesis and sintering at 1200°C for 2 h, as previously reported in ref. [27].

The as-synthesized PMN–10PT powder was further processed to obtain four powder modifications, which were used in the AD process. The first powder, here referred to as the non-treated powder (NT), did not receive any post-synthesis treatment. The remaining three powders were thermally treated at 900°C for 1 h. The second powder (H) was subjected only to the heat treatment, while the third (HM30) and fourth (HM60) powders were subjected to an additional ball milling for 30 min and 60 min, respectively. The milling conditions were similar to those used in the previous steps, i.e., milling at 200 min^{-1} in isopropanol using YSZ milling balls with diameters of 3 mm. Prior to the AD, the powders were sieved through a 200-µm mesh and vacuum dried for 12 h at 100°C and at 10 mbar.

The AD equipment was provided by InVerTec, Germany. Commercial stainless steel (SS, no. 304, American Iron and Steel Institute) with a bright, polished surface (A480: No. 8, American Society for Testing and Materials) and dimensions 15 mm × 15 mm × 0.8 mm was used as the substrate. The process parameters during the AD, reported elsewhere [28], were kept the same for the deposition of all four powders. After the AD, the samples were cleaned with ethanol and annealed at 500°C for 1 h using 2 $K \cdot min^{-1}$ heating and cooling rates in order to release the internal stresses developed in the material during deposition.

The X-ray diffraction (XRD) analysis was performed with a high-resolution diffractometer (X'Pert PRO, PANalytical, Netherlands) using Cu–Kα_1 radiation. Diffraction patterns were recorded in the Bragg–Brentano geometry using a 100-channel X'Celerator detector in a 2θ range of 10°–120° with a step of 0.017° and an integration time of 100 s per step. The Topas R package (version 2.1, Bruker AXS GmbH, Germany) was employed for the Rietveld refinement and the Fundamental Parameters Approach (FPA) was used for the line-profile fitting of all the samples [29]. The FPA uses the geometrical properties of the diffraction experiment to build up the instrumental line width from first principles. It thus allows an explicit determination of the sample-dependent line-broadening contributions to the peak profile, which are dominated by the microstrain and broadening due to decrease in the crystallite size [30]. The microstructure effects were modeled using the Double-Voigt approach [31]. The volume-weighted mean crystallite size was calculated based on the integral breath method incorporated in the Topas software. The residual stress analyses of the films in the Bragg–Brentano geometry were performed with a high-resolution XRD diffractometer (Bruker D8 Advance, Bruker AXS GmbH, Germany) using Cu–Kα_1 radiation equipped with a Eulerian cradle.

Particle size analyses were performed using a light-scattering laser granulometer (S3500, Microtrac, USA) with isopropanol (IPA) as a medium. Prior to the measurement the powder in the liquid medium was placed in an ultrasonic bath (PRO 50, ASonic, China) for a few minutes in order to break the agglomerates.

Scanning electron microscopy (SEM) analyses were performed with a field-emission scanning electron microscope (FE-SEM, JSM-7600F, JEOL, Japan) equipped with an energy-dispersive X-ray spectrometer (EDXS, Inca Oxford 350 EDS SSD, Oxford Instruments, UK). For the SEM analyses, the powders were deposited on carbon tape. In the case of the thick films, plain surfaces and polished cross-sections were analysed. For the cross-sectional analyses, the samples were cut, mounted in epoxy resin, ground and fine-polished using a colloidal silica suspension. Prior to the SEM analyses, all the samples were coated with a 3-nm-thick carbon layer using a Precision Etching and Coating System (PECS 682, Gatan, USA).

The porosity of thick films was estimated from SEM cross-sectional images using the Image Tool software (UTHSCSA Image Tool Version 3.00. 2002, [32]). Also the size analyses of the powder particles were based on SEM images with the Image Tool software and measuring more than 150 particles. The data are presented as a number particle size distribution and the particle size is expressed as Feret's diameter [33].

The transmission electron microscopy (TEM), including selected-area electron diffraction (SAED), of the powders dispersed on a grid and the thick films in cross-section were performed using JEM 2100 and JEM 2010F (JEOL, Japan) microscopes, respectively. Prior to the analyses, the thick-film samples were cut, ground, dimpled and finally Ar-ion milled (PIPS 691, Gatan, USA). The SAED patterns were indexed according to the cubic perovskite structure (JCPDS 81-0861, $Pm\bar{3}m$ space group).

Raman measurements of the thick films were performed with a single spectrograph apparatus (LabRAM 300, Horiba Jobin Yvon, France), using an excitation wavelength of 532 nm. The spectra were collected in the backscattered geometry with an edge filter (cut-off: 80 cm^{-1}), 1800 $gr \cdot mm^{-1}$ grating, slit size of 100 µm and a charge-coupled-device camera. The laser beam spot had a diameter of ~1 µm on the specimen's surface.

The film thickness was evaluated from the step height of the line profiles measured with a contact profilometer (DektakXT, Bruker, USA). A quadratic polynomial was used for the curvature removal on the line profiles. For each powder, the deposition rate (DR) was calculated from the film thickness (h), film width (w), sweep speed (v) and number of scans (N), according to the following Eq. (1):

$$DR = \frac{h \cdot w \cdot v}{N} \quad (1)$$

For the electrical measurements, the bulk ceramic pellets were cut to a thickness of ~200 µm and polished, while in the case of the thick films no additional preparation was needed. In both cases, the surfaces were coated with Au electrodes using a RF-magnetron sputtering machine (5 Pascal, Italy). The diameters of the electrodes sputtered on the thick-film and ceramic surfaces were 1.5 mm and 5 mm, respectively. The unipolar polarization–electric field (P–E) hysteresis loops of the films and ceramics were measured using an aixACCT TF analyzer 2000 (aixACCT Systems GmbH, Germany) by applying a single sinusoidal waveform with a frequency of 100 Hz. For the P–E loops that were measured at temperatures ranging from 0°C to 200°C and during room-temperature repetitive electric-field cycling an electric field of 500 $kV \cdot cm^{-1}$ was applied.

3. Results and discussion

3.1. Influence of the powder properties on the AD rate

Initially, the influence of the powder properties on the aerosol-deposition rate was studied. The morphology, state of agglomeration and particle size of all four PMN–10PT powders were investigated using laser granulometry, SEM and TEM. The laser granulometric analyses are shown in Supplementary material S1. The measurements made in isopropanol (IPA) revealed multimodal size distributions and a broad particle size range in all the powders, i.e., between 100 nm and a few tens of micrometers, indicating the formation of agglomerates, presumably partially related to the IPA liquid medium used during the measurements. Note also that the sub-100-nm particles were not detected by laser granulometry, due to the detection limit of the device [34]. On the other hand, the particle size analyses by SEM (Fig. 1) revealed non-agglomerated particles with sizes below 500 nm.

According to data from the SEM analyses (Fig. 1d, h, l, p), the non-treated (NT) powder consists of the smallest particles. These particles are, according to the SEM and TEM, irregularly shaped and their size range is between 20 nm and 120 nm, with a median particle size (d_{50}) of 50 nm (Fig. 1d). Such small particles tend to reduce their surface energy by assembling into agglomerates larger than 200 nm, as observed in Fig. 1b and c.

The thermal treatment completely modifies the powder properties, since the early stages of interparticle sintering occur due to sufficient thermal energy being available. The H powder consists mainly of large, round-like particles with smooth surfaces. According to the particle size distribution determined from the SEM micrographs (Fig. 1h), the size of these particles ranges between 150 nm and 450 nm, with a d_{50} of 250 nm.

Milling influences both the particle size and shape. In comparison to the H powder, the milled HM30 powder contains smaller particles with sizes between 100 nm and 400 nm, and a d_{50} of 220 nm (Fig. 1l). Due to milling, the particles are also more irregularly shaped in comparison to the round-like particles of the H powder.

Further milling leads to the formation of more irregularly shaped particles with fresh surfaces and higher specific surface energies [35]. These particles tend to reduce their surface energy by assembling into large agglomerates, some of them exceeding 2000 nm (Fig. 1m). According to the particle size distribution determined from the SEM micrographs (Fig. 1p), the size of the HM60 powder particles typically ranges between 50 nm and 400 nm, with a d_{50} of 200 nm. Despite progressive milling, these few-hundred-nm-sized particles (Fig. 1o) can be identified as single crystalline particles according to the SAED analysis (Supplementary material S2). Furthermore, in all three heat-treated powders, a few examples of particles with sizes around or below 100 nm were observed with the TEM (Fig. 1g, k and o).

X-ray diffraction analyses (XRD) were performed on all four PMN–10PT powders (Fig. 2). All the powders were indexed to the perovskite structure with the $Pm\bar{3}m$ space group (JCPDS 81-0861). No secondary phases were detected. The XRD patterns reveal a substantial peak broadening of the NT powder compared to other samples. Such broadening is evidence of a reduced crystallite size and/or microstrain. These XRD patterns were examined in detail using Rietveld refinements and the results are shown in Fig. 2c. The smallest average crystallite size of 21 nm ± 1 nm and the largest microstrain of $15.4 \cdot 10^{-4} \pm 0.8 \cdot 10^{-4}$ was found in the NT powder that was high-energy milled, but not thermally treated afterwards. In the other three powders that were exposed to a thermal treatment, the average crystallite size increased to ~190 nm and the microstrain decreased below $2.0 \cdot 10^{-4}$. Note that the crystallite size of the heat-treated powders is comparable to the particle size determined by the SEM analysis (Fig. 1), where d_{50} is slightly above 200 nm. These particles are mainly single crystalline, which was confirmed by the SAED analyses (Supplementary material S2).

Finally, all four powders were deposited on stainless-steel (SS) substrates under similar conditions. Fig. 3a shows photographs of the deposited thick films and their surface line scans, while the SEM images of the films in cross-section are shown in Fig. 3b. The

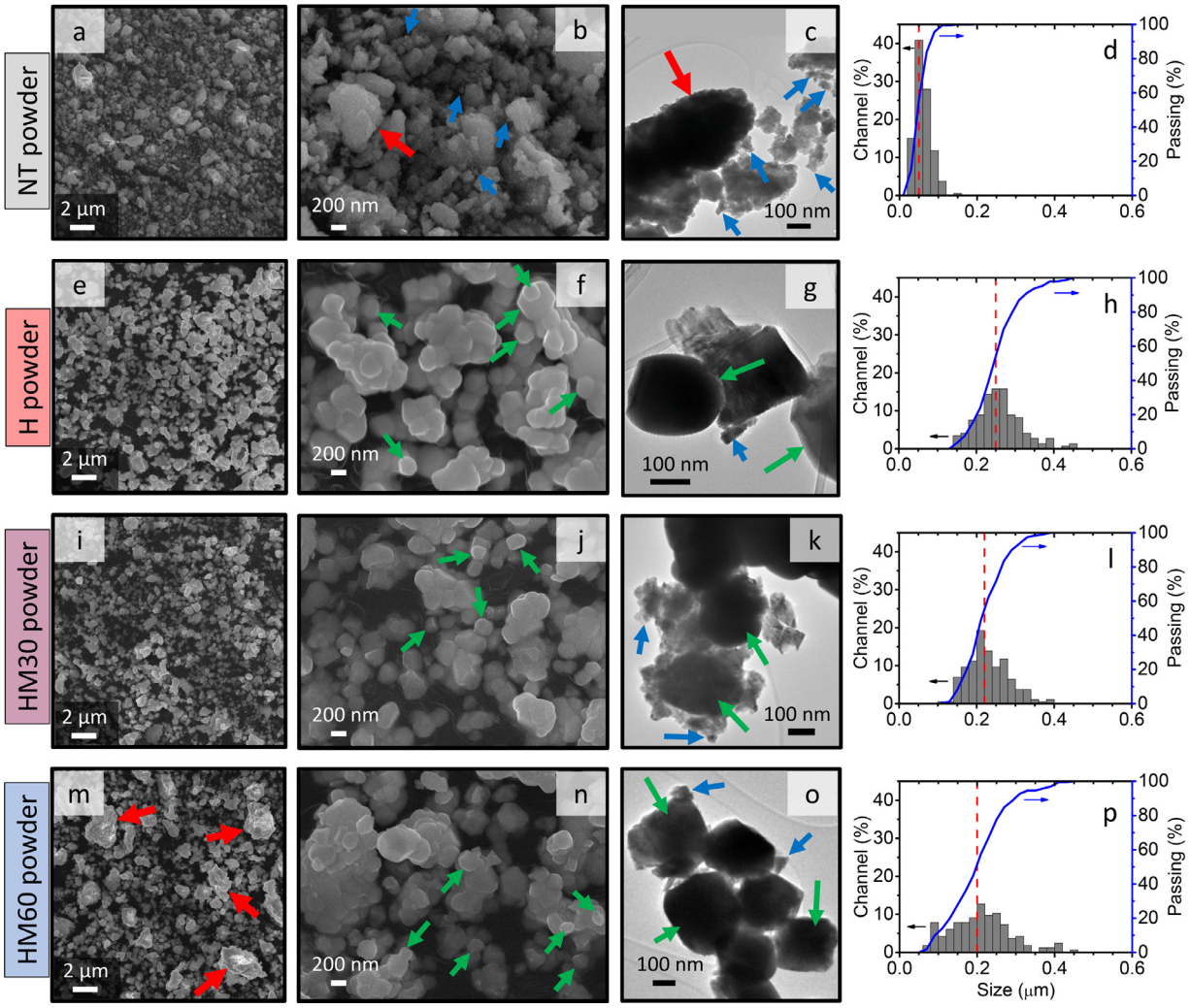

Fig. 1. SEM micrographs (1st and 2nd columns), bright-field TEM micrographs (3rd column) and particle size distribution from SEM micrographs (4th column) of the NT powder (1st row), H powder (2nd row), HM30 powder (3rd row) and HM60 powder (4th row). Blue and green arrows mark clearly visible particles of a few tens and a few hundreds of nm in size, respectively. Red arrows mark agglomerates. Note the different scales of individual panels. The vertical red dashed lines represent d_{50}. (For interpretation of the references to colour in this figure legend, the reader is referred to the web version of this article.)

deposition of the NT powder was not successful. There was only a build-up of a pile of loose powder, which was easily wiped off. Importantly, the NT powder was found to contain relatively small particles in the range of tens of nm. According to the literature, such small particles (< 100 nm) are either deflected during the AD process by bow shocks before reaching the substrate or they elastically bounce off the substrate. Consequently, these particles do not plastically deform or fracture and, therefore, a room-temperature impact consolidation mechanism is not reached [8].

Both the H and HM30 powders resulted in consolidated films with homogeneous thicknesses over the whole deposition area (Fig. 3a). The films' surface profiles indicate that the edge of each film is slightly thicker. A reason for that could be the higher deposition rate that might occur locally due to the mask used for the film edges [36]. The calculated deposition rates of the H and HM30 powders, presented in Fig. 3c, reach 0.15 $mm^3 \cdot min^{-1}$ and 0.27 $mm^3 \cdot min^{-1}$, respectively. Such high deposition rates are typically achieved with the AD method [37,38]. The additional heating of the powder provided sufficiently large particles with a d_{50} of 250 nm, which enabled their successful deposition. Further milling slightly reduced the d_{50} to 220 nm, which correlates with the increasing deposition rate of the HM30 powder. This is in agreement with other reports [39,40], where it was explained that smaller particles can be more easily dispersed in a turbulent gas flow than larger particles. Thus, milling of the powder increases the aerosol concentration in the aerosol-generation process, leading to a higher deposition rate.

With a longer milling time, the HM60 powder resulted in an unsuccessful and uncontrolled film deposition (Fig. 3). After the AD, piles of loose powder were easily wiped off and only a partially covered deposition area remained. The result indicates a dual nature of the HM60 powder. Besides the particles that have a potential to form very dense films, a fraction of the powder is depositing without consolidation. This powder fraction is most likely represented by the large agglomerates that are identified in Fig. 1m. It is known that the presence of agglomerates can disturb successful film formation due to the different impact behaviour of agglomerates in comparison to single-grain particles [8]. During the AD, agglomerates are most likely to accumulate on the surface of the nozzle and pipes until a critical amount is reached and the agglomerates are released in the aerosol flow. Because of the repetitive process, the concentration of agglomerates in the aerosol varies over time, resulting in an inhomogeneous film thickness.

In the first part of our study, it was shown how crucial the powder preparation is for a successful aerosol deposition. A combination of heating and subsequent milling proved to be impor-

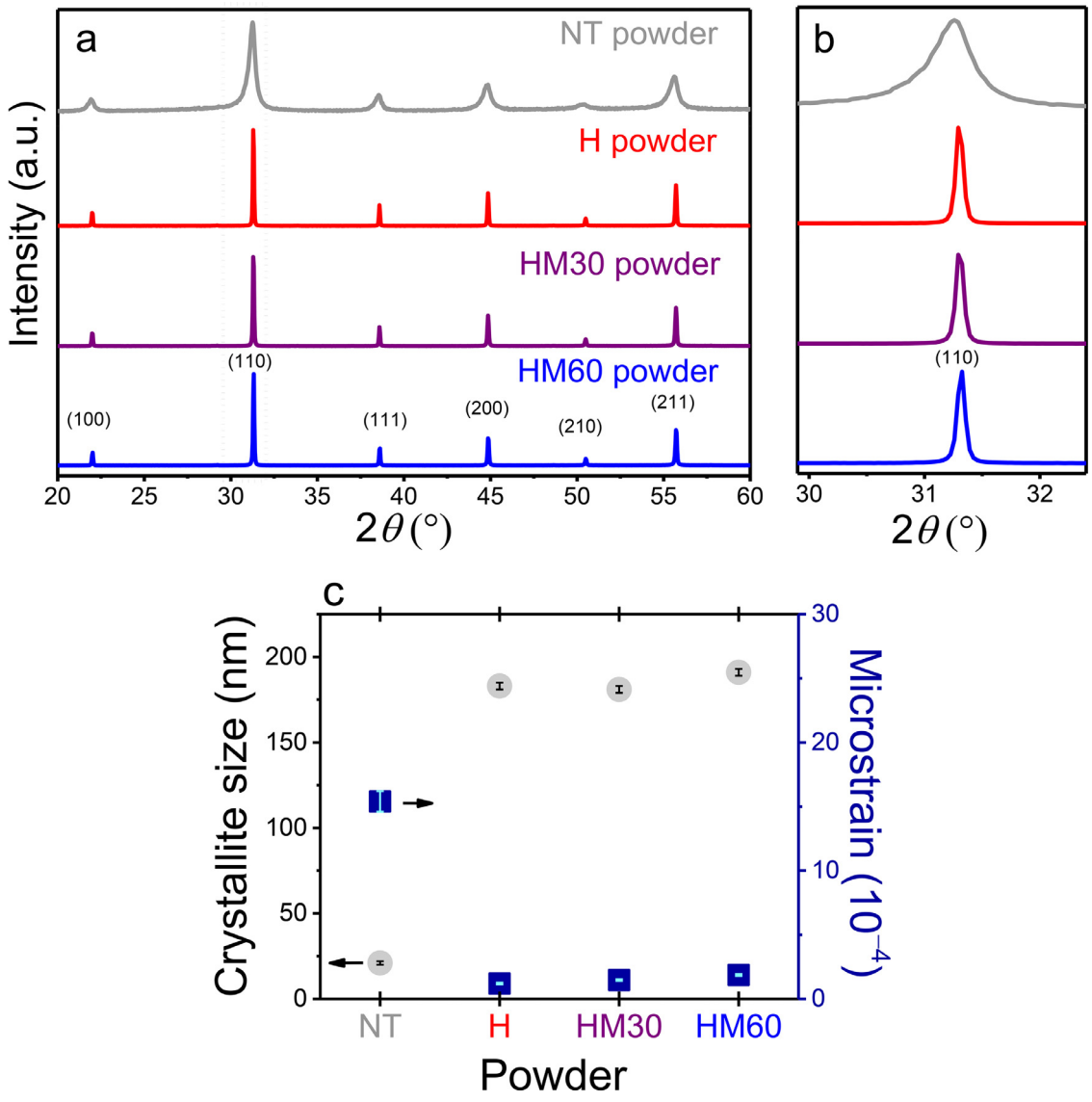

Fig. 2. (a) Zoom-in XRD patterns in the 2θ range 20–60° for powders used in the AD. All the peaks were indexed to a cubic perovskite structure. (b) Enlarged view of (110) cubic reflection. (c) The corresponding crystallite size (grey circles) and microstrain (blue squares) evaluated by Rietveld refinement. (For interpretation of the references to colour in this figure legend, the reader is referred to the web version of this article.)

tant for obtaining a PMN–10PT powder with an optimized particle size, which enables the formation of dense and homogeneous thick films at increased deposition rates. The most successful deposition was achieved with the HM30 powder. Therefore, all the thick films used in subsequent analyses were prepared from this powder. In the next part of this study, the influence of thermal annealing at 500°C on the structural, microstructural and functional properties of the thick films prepared from the HM30 powder on low-cost stainless steel is discussed.

3.2. Influence of annealing on the structural, microstructural, and energy-storage properties of AD films

Next, the influence of annealing on the structural, microstructural, and energy-storage properties of AD thick films is studied. The films are denoted as “as-deposited” or “annealed”. The XRD patterns of the as-deposited and annealed thick films are shown in Fig. 4a. The XRD pattern of the starting HM30 powder is added for comparison. All the samples were indexed to the perovskite structure with the $Pm\bar{3}m$ space group (JCPDS 81-0861). No secondary phases were detected and no peak shift could be observed. In comparison with the HM30 powder, the as-deposited films exhibited a remarkable peak broadening that originates from a reduced crystallite size and/or microstrain. The reduction in the crystallite size and the increased microstrain could be caused by the collision of particles with the substrate during the AD process [8,41]. These XRD patterns were examined in detail using Rietveld refinements and the results are shown in Fig. 4b. As already mentioned, the starting HM30 powder shows intense and sharp reflections with a refined crystallite size of 181 nm ± 2 nm and a microstrain of $1.5 \cdot 10^{-4} \pm 0.1 \cdot 10^{-4}$. The as-deposited film has a reduced crystallite size of 33 nm ± 1 nm and an increased microstrain of $25.9 \cdot 10^{-4} \pm 0.3 \cdot 10^{-4}$, which developed in the films during the aerosol-deposition process. With further annealing at 500°C, the crystallite size does not change significantly and continues at around 38 nm ± 2 nm. On the other hand, annealing seems to reduce the microstrain by 47% (Fig. 4b).

To further investigate the residual stresses developed during the AD, a tilt-angle-dependent XRD analysis, i.e., the $\sin^2\Psi$ method

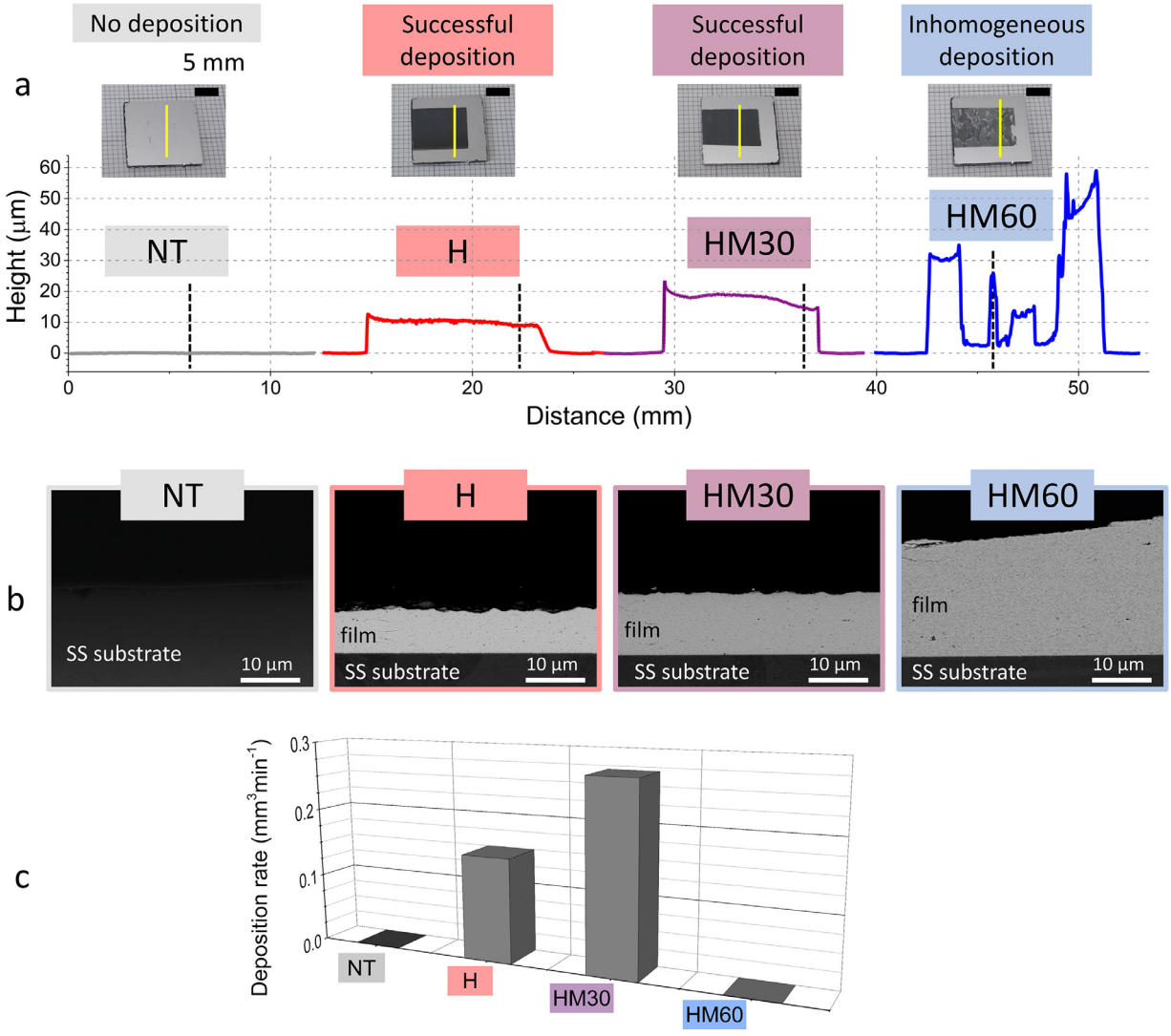

Fig. 3. (a) Photographs with the corresponding line profiles, (b) SEM cross-sectional images and (c) deposition rate of samples with differently modified powders. The measured line profiles are marked on the photographs with yellow lines. The estimated position of the SEM cross-sectional images is marked on the line profiles with black dashed lines. Note that the represented deposition rate of the HM60 powder is zero, due to the inhomogeneous film thickness. (For interpretation of the references to colour in this figure legend, the reader is referred to the web version of this article.)

[42], was performed on the as-deposited and annealed films. The (211) reflection was measured at different sample-tilting angles Ψ. The results shown in Fig. 4c reveal compressive in-plane residual stresses in the as-deposited films. The decrease in the slope indicates that the residual stresses partially relax when annealing the films, a result that is consistent with previous reports on AD thick films [19,43].

Additional stress analyses were performed using Raman spectroscopy. The Raman spectra of the as-deposited and annealed films are shown in Fig. 4d. The as-deposited film displays a slight peak shift towards higher wavenumbers. This is evident from the 270 cm^{-1} band, which is related to the mixed B-O-B-bending and O-B-O-stretching modes [44]. This mode is the only one influenced by temperature variations, and is expected to be sensitive to stress as well [45]. A shift towards higher wavenumbers in the as-deposited films can be associated with a higher compressive stress; recovery of this shift after annealing is thus compatible with a residual stress relaxation during annealing.

SEM images of as-deposited and annealed films are shown in Fig. 5a–d. The cross-sectional view of the as-deposited sample reveals a very dense film with excellent adhesion to the SS substrate (Fig. 5a). There is no apparent damaged layer at the film-substrate interface. The as-deposited film contains nm-sized pores that can be clearly distinguished at higher magnification, as shown in Supplementary material S3. In addition, the microstructure also reveals larger pores, a few tens of nm in size (Fig. 5a). Like the cross-sectional view (Fig. 5a), the surface-view (Fig. 5c) also reveals a very dense film. Excellent adhesion and high density were maintained after the annealing (Fig. 5b, d). Furthermore, no notable microstructural differences were observed between the as-deposited and the annealed films. In addition, the porosity of as-deposited and annealed films, which was estimated from SEM cross-sectional images, reached 1.6% and 1.5%, respectively. TEM images of the as-deposited films are shown in Fig. 5e, f. The SAED analyses of the film reveal its polycrystalline nature (inset of Fig. 5e). A clearly visible film-substrate interface in Fig. 5e confirms the excellent adhesion. The as-deposited film contains grains from 10 nm (Fig. 5f) to 200 nm in size (Fig. 5a, c, e).

Unipolar *P–E* hysteresis loops of the as-deposited and annealed films are shown in Fig. 6a. The as-deposited films exhibit a dielectric-like behavior at 300 $kV{\cdot}cm^{-1}$. By increasing the electric field up to 900 $kV{\cdot}cm^{-1}$, the *P–E* loop of the as-deposited film

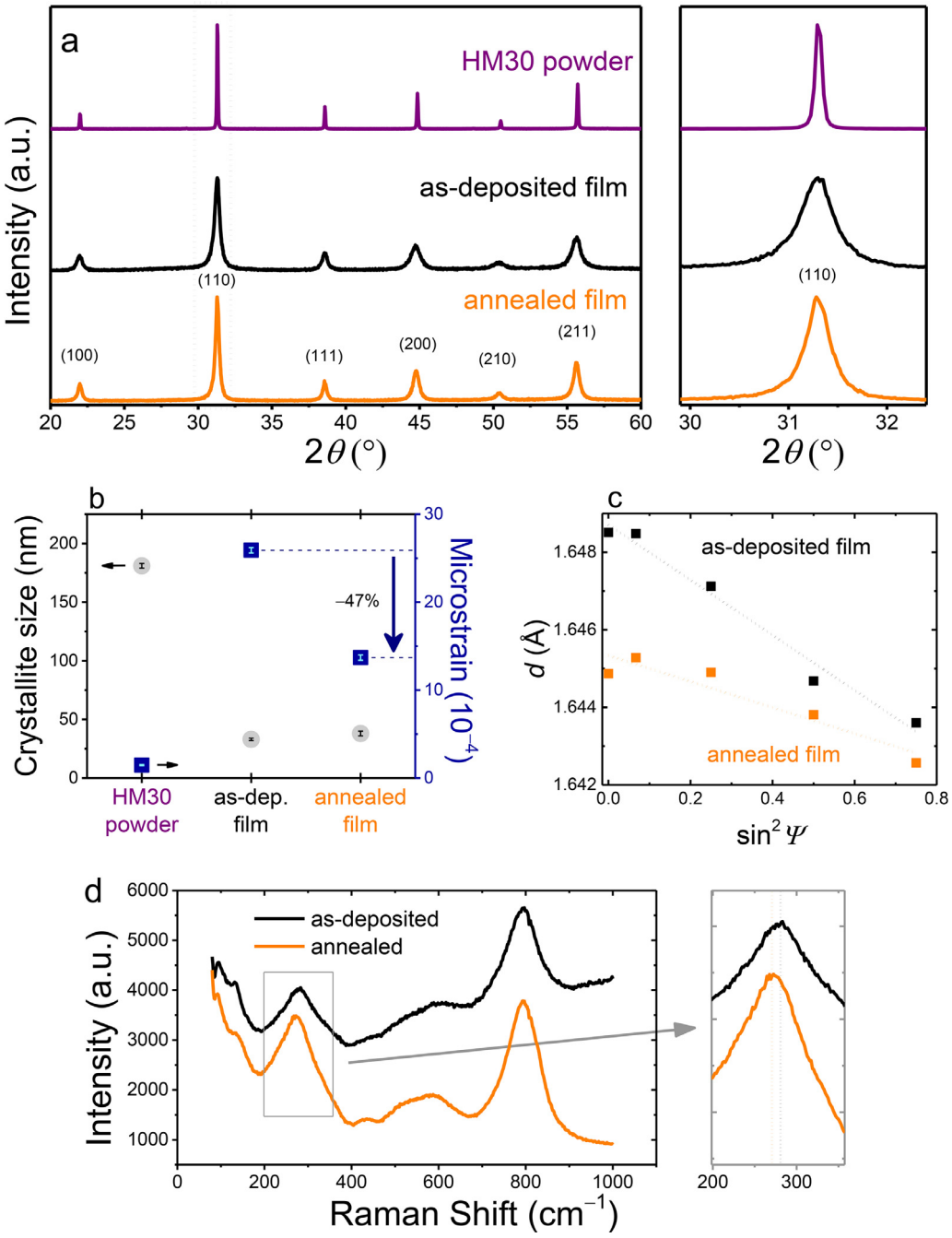

Fig. 4. (a) Zoom-in XRD patterns in the 2θ range 20–60° for HM30 powder and as-deposited and annealed films (left); enlarged view of (110) cubic reflection (right). (b) The corresponding crystallite size (grey circles) and microstrain (blue squares) evaluated using Rietveld refinement. (c) d-spacing of the (211) reflection plotted with respect to $\sin^2\Psi$ for as-deposited and annealed films. Dotted lines represent a linear fit to a measured data set. (d) Raman spectra of as-deposited and annealed thick films. The right panel shows an enlarged view of the 270 cm^{-1} peak. (For interpretation of the references to colour in this figure legend, the reader is referred to the web version of this article.)

opens slightly. By annealing the films at 500°C and thus partially releasing the stresses, the *P–E* loops develop a relaxor-ferroelectric character, reaching a maximum polarization (P_{max}) of 39 μC·cm^{-2} at 900 kV·cm^{-1}. Relaxor-like behavior is typical for PMN-rich compositions as well as for other PMN-PT compositions with the grain size in the range of hundreds of nm [46]. Such high polarization and low hysteresis losses make aerosol-deposited PMN–10PT films especially interesting for energy-storage applications.

In non-linear dielectrics, the recoverable energy density (U_{rec}) is calculated by integrating the area between the discharge curve and the polarization axis. An example of U_{rec} is shown by the orange patterned area in Fig. 6a. The charging-discharging of a ferroelectric-like capacitor is, in practice, associated with hysteresis, which represents the polarization losses. The energy-loss density (U_{loss}) is calculated by integrating the area between the charge and discharge curves. An example of U_{loss} is represented with the black patterned area in Fig. 6a. In addition to U_{rec}, the energy-storage efficiency (η) is an important parameter for evaluating the performance of materials used in energy-storage capacitors. η is defined as the ratio between the recovered and stored energy: $\eta = U_{rec}/(U_{rec}+U_{loss})$ [1].

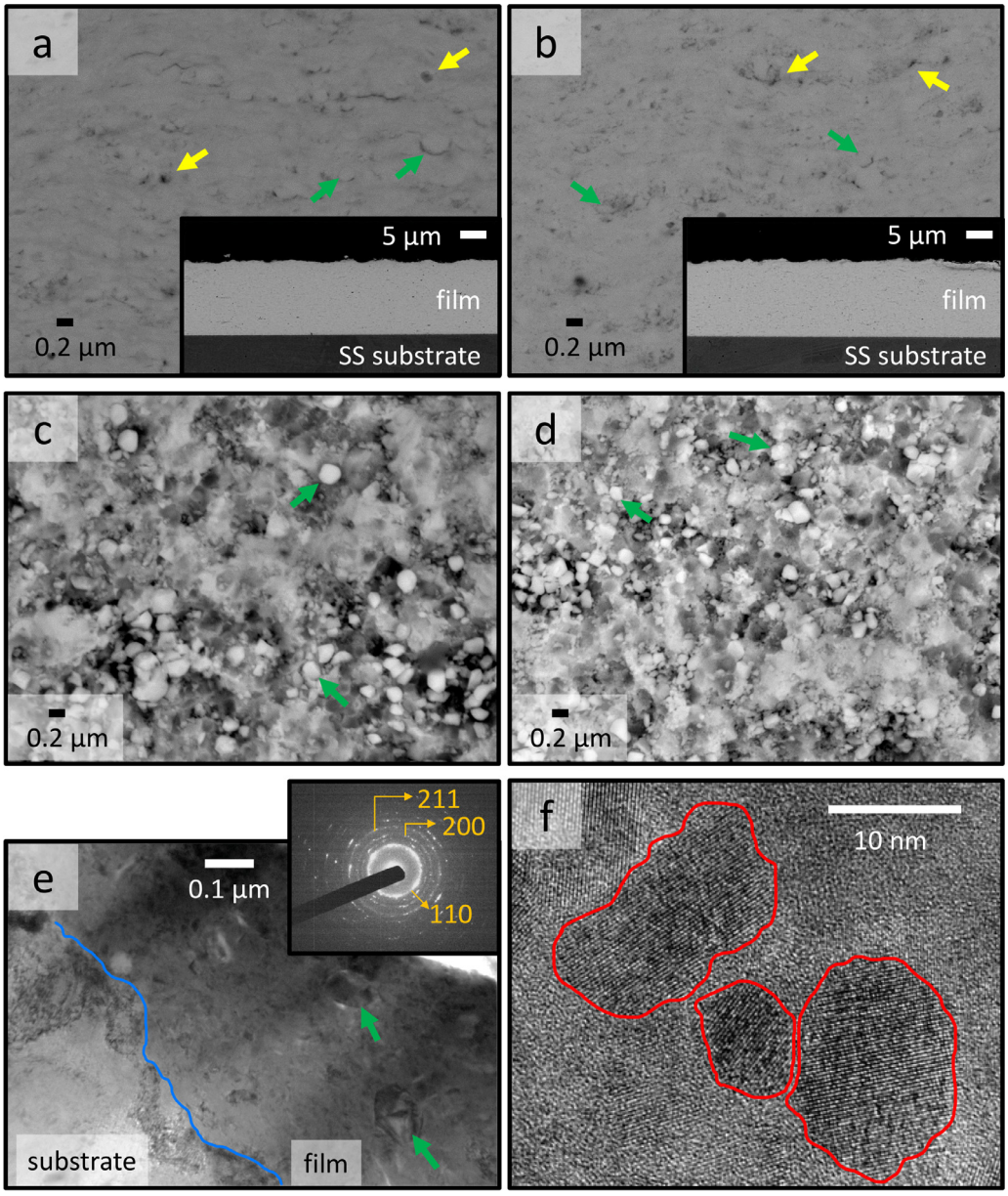

Fig. 5. SEM images of aerosol-deposited thick films (from the HM30 powder) in cross-section (a, b) and surface (c, d) views. SEM images represent as-deposited (a, c) and annealed (c, d) films. Bright-field TEM image (e) and high-resolution TEM image (f) of as-deposited thick film are shown in cross-sectional view. A SAED pattern of the film is shown in the inset (e). Pores, a few tens of nm large, and ~200-nm-large grains are marked with yellow and green arrows, respectively. The film-substrate interface and the grain boundaries are marked with blue and red lines, respectively. (For interpretation of the references to colour in this figure legend, the reader is referred to the web version of this article.)

The electric-field dependence of the energy-storage properties of the as-deposited and annealed films is shown in Fig. 6b. At low electric fields of 100 kV·cm^{-1}, the as-deposited and annealed films reach U_{rec} of 0.1 J·cm^{-3} and 0.4 J·cm^{-3}, respectively. These values are comparable with the U_{rec} values of PMN–10PT bulk ceramics that were prepared in our laboratory via mechanochemically assisted synthesis, followed by sintering (blue stars in Fig. 6b), as well as with the results of other reported aerosol-deposited thick films [47–49]. Furthermore, as-deposited and annealed films exhibit a similar η of ~85%, which is much higher than for bulk ceramics (~66%). The thickness of bulk ceramics is limited, typically down to few hundred µm, because of the mechanical thinning process. On the other hand, a-few-µm-thick films are ~100 times thinner than bulk ceramics and thus they require ~100-times-smaller applied voltages to reach the same electric field as the bulk ceramics.

U_{rec} shows a linear increase with the electric field, reaching a value of 7.0 J·cm^{-3} at 900 kV·cm^{-1} for the as-deposited films. This value is comparable to the aerosol-deposited PMN-based films [49] and magnetron sputtered PMN–10PT films [50], both deposited on conventional and costly Si substrates. Furthermore, the annealed films exhibit even higher U_{rec} values of 9.8 J·cm^{-3} at 900 kV·cm^{-1}. These results are comparable to other energy-storage-efficient AD thick films prepared on Si substrates [47-49,51,52] (Supplementary material S4). In comparison to screen-printed thick films [53] and bulk ceramics [54], the aerosol-deposited PMN–10PT thick films exhibit a significantly higher dielectric breakdown strength (DBS) and, consequently, a higher U_{rec}. Note that the dielectric breakdown of PMN–10PT bulk ceramics

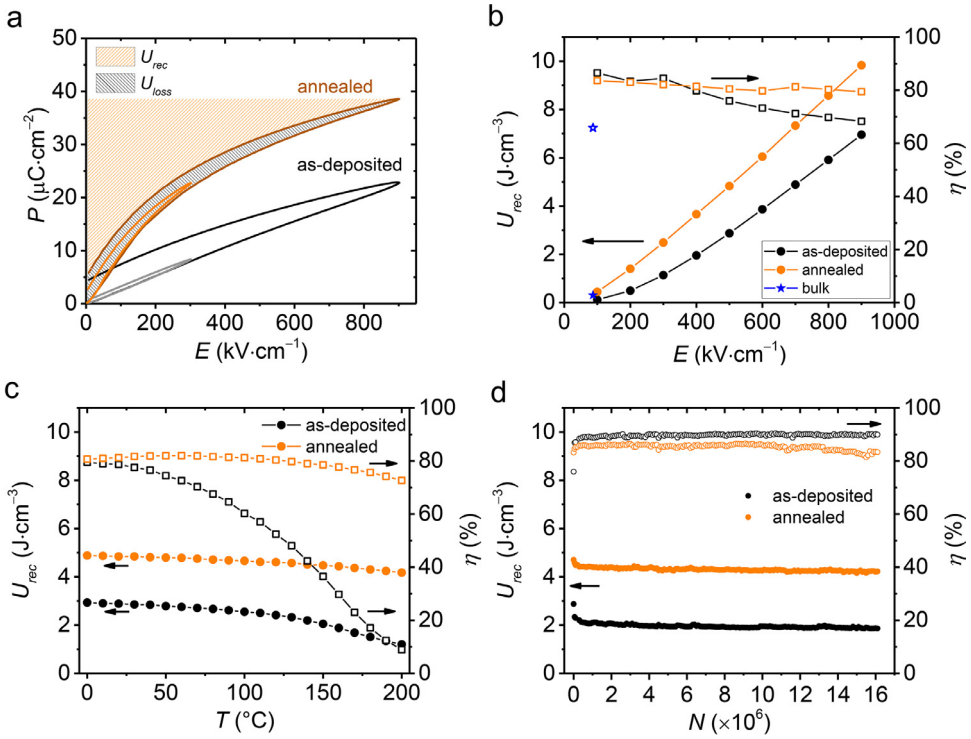

Fig. 6. (a) Unipolar *P–E* hysteresis loops of as-deposited and annealed thick films. Light- and dark-colored lines represent *P–E* loops measured up to 300 kV·cm^{-1} and 900 kV·cm^{-1}, respectively. The U_{rec} and U_{loss} of the annealed film are represented by the orange and black patterned areas, respectively. (b) The electric-field dependence of U_{rec} and η for the as-deposited and annealed thick films and the bulk ceramic. (c) The temperature dependence and (d) electric-field cycling dependence of U_{rec} and η for as-deposited and annealed thick films at 500 kV·cm^{-1}. Lines between the values are just a guide to the eye. (For interpretation of the references to colour in this figure legend, the reader is referred to the web version of this article.)

occurs already at ~100 kV·cm^{-1} (Fig. 6b). According to Weibull analysis, the DBS of as-deposited and annealed PMN-10PT thick films reaches 992 kV·cm^{-1} and 1106 kV·cm^{-1}, respectively (Supplementary material S5). The efficiency of energy-storage materials tends to decrease with the electric field [1]. In as-deposited films, η decreases from 87% at 100 kV·cm^{-1} to 68% at 900 kV·cm^{-1} ($\Delta\eta$ = 19%). On the other hand, the efficiency remains constant in annealed films, where η decreases from 84% at 100 kV·cm^{-1} to 79% at 900 kV·cm^{-1} ($\Delta\eta$ = 5%). The efficiency of our annealed thick films is similar to the most efficient PMN-based thick films deposited on Si substrates [49]. Additionally, a comparison of their stabilities, $\Delta\eta$, with an increasing electric field reveals the superior performance of our films.

The energy-storage properties of the as-deposited and annealed films at different temperatures and increasing numbers of electric-field cycles are shown in Fig. 6c and d, respectively. The U_{rec} and especially η of the as-deposited films decrease with increasing temperature. A reason for this decrease is related to the opening of the *P–E* hysteresis loops (Supplementary material S6), which is most probably associated with an increased electrical conductivity at elevated temperatures. At room temperature, sharp *P–E* loops are observed, while with increasing temperature, *P–E* loops become more rounded, indicating the presence of a leakage current. The increase in the electrical conductivity of the as-deposited films at elevated temperatures is evident from the increase in the dielectric losses *tan δ* (Supplementary material S7) and the local electrical current (Supplementary material S8) with increasing temperature. On the other hand, the annealed films exhibit sharp *P–E* loops even at elevated temperatures. These films also exhibit a sufficient temperature stability up to 200°C. Both the as-deposited and annealed films exhibit sufficient electric-field cycling stability until the occurrence of dielectric breakdown after 1.6·10^7 cycles (Fig. 6d).

4. Summary and conclusions

The room-temperature deposition of PMN–10PT thick films on low-cost stainless-steel substrates was investigated for the first time. Prior to the aerosol deposition, the properties of the PMN–10PT powder were optimized through heating and milling processes. A successful deposition of 15-μm-thick and very dense films on stainless-steel substrates was achieved with powder containing particles of a few hundreds of nanometres. The films exhibited excellent energy-storage properties already in the as-deposited forms, reaching 7.0 J·cm^{-3} of recoverable energy density and 68% of energy-storage efficiency at 900 kV·cm^{-1}.

The post-deposition thermal annealing of films at 500°C resulted in a significant stress relaxation of the deposited layers, which improved the U_{rec} and η, reaching 9.8 J·cm^{-3} and 79% at 900 kV·cm^{-1}, respectively. Furthermore, the excellent temperature stability of U_{rec} and η up to 200°C and the electric-field cycling stability up to 1.6·10^7 cycles make the films promising for energy-storage applications. To conclude, we successfully prepared energy-storage-efficient, 15-μm-thick films integrated directly onto more affordable stainless-steel substrates without any additional intermediate electrode layer, which opens up possibilities for new, integrated energy-storage applications. A low-cost AD method with a fast deposition rate has the potential to be used in mass production processes, which could significantly impact the availability and affordability of future electronic devices. Further research in the field of energy storage capacitors could target efficient lead-free materials [55] that are compatible with stainless-steel applications for everyday use, such as stainless-steel medical devices, smart buildings, vehicles and other stainless steel consumer products. Very promising groups of materials are antiferroelectrics and relaxor-antiferroelectrics, which combine relaxor and antiferroelectric properties [56–59].

Declaration of Competing Interest

The authors declare that they have no known competing financial interests or personal relationships that could have appeared to influence the work reported in this paper.

Acknowledgments

This work was funded by the Slovenian Research Agency (bilateral project BI-DE-20/21-012, young researcher project M. Sadl, research project N2-0212 and programme P2-0105) and Ultracool Directorś fund 2017. M. Deluca acknowledges funding from the European Research Council (ERC) under the European Union's Horizon 2020 research and innovation programme (grant agreement No 817190). U. Eckstein, N. H. Khansur, K. G. Webber acknowledge the financial support for their contributions to this work from the Deutsche Forschungsgemeinschaft under GRK2495/F as well as the travel support of the DAAD under project 57402168 as part of the PPP Slovenian Programme. N. H. Khansur acknowledges the financial support for this work from the Deutsche Forschungsgemeinschaft under grant No KH 471/2-1. The authors thank J. Cilenšek, S. Drnovšek and V. Fišinger for assistance in the laboratory.

Supplementary materials

Supplementary material associated with this article can be found, in the online version, at doi:10.1016/j.actamat.2021.117403.

References

[1] H. Palneedi, M. Peddigari, G.T. Hwang, D.Y. Jeong, J. Ryu, High-performance dielectric ceramic films for energy storage capacitors: progress and outlook, Adv. Funct. Mater. 28 (42) (2018) 1–33.
[2] V.K.Thakur Prateek, V.K. Thakur, R.K. Gupta, Recent progress on ferroelectric polymer-based nanocomposites for high energy density capacitors: synthesis, dielectric properties, and future aspects, Chem. Rev. 116 (7) (2016) 4260–4317.
[3] C.A. Randall, H. Ogihara, J.-R. Kim, G.-Y. Yang, C.S. Stringer, S. Trolier-McKinstry, M. Lanagan, High temperature and high energy density dielectric materials, in: 2009 IEEE Pulsed Power Conference, 2009, pp. 346–351.
[4] X. Hao, A review on the dielectric materials for high energy-storage application, J. Adv. Dielectr. 03 (01) (2013) 1330001.
[5] T.F. Zhang, X.G. Tang, Q.X. Liu, Y.P. Jiang, X.X. Huang, Q.F. Zhou, Energy-storage properties and high-temperature dielectric relaxation behaviors of relaxor ferroelectric Pb($Mg_{1/3}$ $Nb_{2/3}$)O_3–$PbTiO_3$ ceramics, J. Phys. D. Appl. Phys. 49 (9) (2016) 095302.
[6] M. Kosec, D. Kuscer, J. Holc, Processing of ferroelectric ceramic thick films, Multifunctional Polycrystalline Ferroelectric Materials, Springer, Dordrecht, 2011.
[7] J. Akedo, Room temperature impact consolidation (RTIC) of fine ceramic powder by aerosol deposition method and applications to microdevices, J. Therm. Spray Technol. 17 (2) (2008) 181–198.
[8] D. Hanft, J. Exner, M. Schubert, T. Stöcker, P. Fuierer, R. Moos, An overview of the aerosol deposition method: process fundamentals and new trends in materials applications, J. Ceram. Sci. Technol. 6 (3) (2015) 147–181.
[9] A. Garner, Stainless Steels and Specialty Alloys for Pulp, and Biomass Conversion, Durham: Nickel institute, 2017 vol. 2.
[10] P. Snelgrove, Stainless steel automotive and transport developments, Int. Stainl. Steel Forum (2016) 1–5 [Online]. Available https://www.worldstainless.org/Files/issf/non-image-files/PDF/Stainlesssteelautomotiveandtransportdevelopments.pdf.
[11] G. Gedge, Structural uses of stainless steel - buildings and civil engineering, J. Constr. Steel Res. 64 (11) (2008) 1194–1198.
[12] J. Akedo, M. Lebedev, Effects of annealing and poling conditions on piezoelectric properties of Pb($Zr_{0.52}$,$Ti_{0.48}$)O_3 thick films formed by aerosol deposition method, J. Cryst. Growth 235 (1–4) (2002) 415–420.
[13] J. Akedo, M. Lebedev, H. Sato, J. Park, High-speed optical microscanner driven with resonation of lam waves using Pb(Zr,Ti)O_3 thick films formed by aerosol deposition, Jpn. J. Appl. Phys. 44 (9B) (2005) 7072–7077.
[14] S.-C. Lin, W.-J. Wu, Fabrication of PZT MEMS energy harvester based on silicon and stainless-steel substrates utilizing an aerosol deposition method, J. Micromech. Microeng. 23 (12) (2013) 125028.
[15] Y. Kawakami, H. Yoshikawa, K. Komagata, J. Akedo, Powder preparation for 0.5 Pb($Ni_{1/3}Nb_{2/3}$)O_3-0.15 $PbZrO_3$-0.35$PbTiO_3$ thick films by the aerosol deposition method, J. Cryst. Growth 275 (1–2) (2005) 1295–1300.
[16] S. Baba, J. Akedo, Damage-free and short annealing of Pb(Zr,Ti)O_3 thick films directly deposited on stainless steel sheet by aerosol deposition with CO_2 laser radiation, J. Am. Ceram. Soc. 88 (6) (2005) 1407–1410.
[17] S.W. Oh, J. Akedo, J.H. Park, Y. Kawakami, Fabrication and evaluation of lead-free piezoelectric ceramic LF4 thick film deposited by aerosol deposition method, Jpn. J. Appl. Phys. 45 (9B) (2006) 7465–7470.
[18] Y. Kawakami, M. Watanabe, K.I. Arai, S. Sugimoto, Effects of substrate materials on piezoelectric properties of $BaTiO_3$ thick films deposited by aerosol deposition, Jpn. J. Appl. Phys. 55 (10) (2016) 10TA10.
[19] N.H. Khansur, U. Eckstein, L. Benker, U. Deisinger, B. Merle, K.G. Webber, Room temperature deposition of functional ceramic films on low-cost metal substrate, Ceram. Int. 44 (14) (2018) 16295–16301.
[20] J. Exner, M. Schubert, D. Hanft, J. Kita, R. Moos, How to treat powders for the room temperature aerosol deposition method to avoid porous, low strength ceramic films, J. Eur. Ceram. Soc. 39 (2–3) (2019) 592–600.
[21] R. Saunders, S.D. Johnson, D. Schwer, E.A. Patterson, H. Ryou, E.P. Gorzkowski, A self-consistent scheme for understanding particle impact and adhesion in the aerosol deposition process, J. Therm. Spray Technol. (2021).
[22] M. Schubert, J. Exner, R. Moos, Influence of carrier gas composition on the stress of Al_2O_3 coatings prepared by the aerosol deposition method, Materials 7 (8) (2014) 5633–5642.
[23] G. Han, J. Ryu, W.-H. Yoon, J.-J. Choi, B.-D. Hahn, J.-W. Kim, D.-S. Park, C.-W. Ahn, S. Priya, D.-Y. Jeong, Stress-controlled Pb($Zr_{0.52}Ti_{0.48}$)O_3 thick films by thermal expansion mismatch between substrate and Pb($Zr_{0.52}Ti_{0.48}$)O_3 film, J. Appl. Phys. 110 (12) (2011) 124101.
[24] J. Akedo, M. Lebedev, Microstructure and electrical properties of lead zirconate titanate (Pb(Zr_{52}/Ti_{48})O_3) thick films deposited by aerosol deposition method, Jpn. J. Appl. Phys. 38 (9B) (1999) 5397–5401.
[25] N.H. Khansur, U. Eckstein, K. Riess, A. Martin, J. Drnec, U. Deisinger, K.G. Webber, Synchrotron x-ray microdiffraction study of residual stresses in $BaTiO_3$ films deposited at room temperature by aerosol deposition, Scr. Mater. 157 (2018) 86–89.
[26] M. Dragomir, M. Otoničar, M. Vrabelj, L. Fulanović, S. Drnovšek, T. Rojac, B. Malič, Seeding effects on the mechanochemical synthesis of 0.9Pb($Mg_{1/3}Nb_{2/3}$)O_3–0.1$PbTiO_3$, J. Eur. Ceram. Soc. 39 (5) (2019) 1837–1845.
[27] M. Vrabelj, H. Uršič, Z. Kutnjak, B. Rožič, S. Drnovšek, A. Benčan, V. Bobnar, L. Fulanović, B. Malič, Large electrocaloric effect in grain-size-engineered 0.9Pb($Mg_{1/3}Nb_{2/3}$)O_3 –0.1$PbTiO_3$, J. Eur. Ceram. Soc. 36 (1) (2016) 75–80.
[28] M. Sadl, U. Tomc, U. Prah, H. Ursic, Protective Alumina coatings prepared by aerosol deposition on magnetocaloric gadolinium elements, Inf. MIDEM - J. Microelectron. Electron. Components Mater. 49 (3) (2019) 177–182.
[29] R.W. Cheary, A. Coelho, A fundamental parameters approach to X-ray line-profile fitting, J. Appl. Crystallogr. 25 (2) (1992) 109–121.
[30] H.P. Klug, L.E. Alexander, X-Ray Diffraction Procedures: For Polycrystalline and Amorphous Materials, 2nd Ed., John Wiley & Sons, New York, 1974.
[31] D. Balzar, N. Audebrand, M.R. Daymond, A. Fitch, A. Hewat, J.I. Langford, A.Le Bail, D. Louër, O. Masson, C.N. McCowan, N.C. Popa, P.W. Stephens, B.H. Toby, Size-strain line-broadening analysis of the ceria round-robin sample, J. Appl. Crystallogr. 37 (6) (2004) 911–924.
[32] D. Wilcox, B. Dove, B. McDavid, D. Greer, UTHSCSA Image Tool for Windows, Version 3.0, University of Texas Health Science Center, San Antonio, 2002.
[33] W.H. Walton, Feret's statistical diameter as a measure of particle size, Nature 162 (4113) (1948) 329–330.
[34] Microtrac Inc., "Microtrac S3500 particle size analyzer operation and maintenance manual," Largo, 2007.
[35] P. Baláž, et al., Hallmarks of mechanochemistry: from nanoparticles to technology, Chem. Soc. Rev. 42 (18) (2013) 7571–7637.
[36] P. Nieke, J. Kita, M. Häming, R. Moos, Manufacturing dense thick films of lunar regolith simulant EAC-1 at room temperature, Materials 12 (3) (2019) 487.
[37] D. Hanft, P. Glosse, S. Denneler, T. Berthold, M. Oomen, S. Kauffmann-Weiss, F. Weis, W. Häßler, B. Holzapfel, R. Moos, The aerosol deposition method: a modified aerosol generation unit to improve coating quality, Materials 11 (9) (2018) 5–6.
[38] J. Exner, M. Hahn, M. Schubert, D. Hanft, P. Fuierer, R. Moos, Powder requirements for aerosol deposition of alumina films, Adv. Powder Technol. 26 (4) (2015) 1143–1151.
[39] J. Akedo, M. Lebedev, Powder preparation in aerosol deposition method for lead zirconate titanate thick films, Jpn. J. Appl. Phys. 41 (11B) (2002) 6980–6984.
[40] K. Mihara, T. Hoshina, H. Takeda, T. Tsurumi, Controlling factors of film-thickness in improved aerosol deposition method, J. Ceram. Soc. Japan 117 (1368) (2009) 868–872.
[41] J. Akedo, Aerosol deposition of ceramic thick films at room temperature: densification mechanism of ceramic layers, J. Am. Ceram. Soc. 89 (6) (2006) 1834–1839.
[42] I.C. Noyan, T.C. Huang, B.R. York, Residual stress/strain analysis in thin films by X-ray diffraction, Crit. Rev. Solid State Mater. Sci. 20 (2) (1995) 125–177.
[43] M. Nakada, K. Ohashi, J. Akedo, Electro-optical properties and structures of (Pb, La)(Zr, Ti)O_3 and $PbTiO_3$ films prepared using aerosol deposition method, Jpn. J. Appl. Phys. 43 (9B) (2004) 6543–6548.
[44] A. Slodczyk, P. Daniel, A. Kania, Local phenomena of $(1-x)PbMg_{1/3}Nb_{2/3}O_3$-$xPbTiO_3$ single crystals ($0<x<0.38$) studied by Raman scattering, Phys. Rev. B 77 (18) (2008) 1–16.
[45] H. Idink, W.B. White, Raman spectroscopic study of order–disorder in lead magnesium niobate, J. Appl. Phys. 76 (3) (1994) 1789–1793.
[46] M. Algueró, J. Ricote, R. Jiménez, P. Ramos, J. Carreaud, B. Dkhil, J.M. Kiat, J. Holc, M. Kosec, Size effect in morphotropic phase boundary Pb($Mg_{1/3}Nb_{2/3}$)O_3–$PbTiO_3$, Appl. Phys. Lett. 91 (11) (2007) 112905.

[47] M. Peddigari, H. Palneedi, G.T. Hwang, K.W. Lim, G.Y. Kim, D.Y. Jeong, J. Ryu, Boosting the Recoverable Energy Density of Lead-Free Ferroelectric Ceramic Thick Films through Artificially Induced Quasi-Relaxor Behavior, ACS Appl. Mater. Interfaces 10 (24) (2018) 20720–20727.

[48] H.-B. Jung, J.-H. Lim, M. Peddigari, J. Ryu, D.H. Choi, D.-Y. Jeong, Enhancement of energy storage and thermal stability of relaxor $Pb_{0.92}La_{0.08}Zr_{0.52}Ti_{0.48}O_3$-$Bi(Zn_{0.66}Nb_{0.33})O_3$ thick films through aerosol deposition, J. Eur. Ceram. Soc. 40 (1) (2020) 63–70.

[49] C.K. Park, S.H. Lee, J.H. Lim, J. Ryu, D.H. Choi, D.Y. Jeong, Nano-size grains and high density of 65PMN-35PT thick film for high energy storage capacitor, Ceram. Int. 44 (16) (2018) 20111–20114.

[50] X. Wang, L. Zhang, X. Hao, S. An, High energy-storage performance of $0.9Pb(Mg_{1/3}Nb_{2/3})O_3$-$0.1PbTiO_3$ relaxor ferroelectric thin films prepared by RF magnetron sputtering, Mater. Res. Bull. 65 (2015) 73–79.

[51] S. Bin Kang, M.G. Choi, D.Y. Jeong, Y.M. Kong, J. Ryu, Energy storage properties of nano-grained antiferroelectric (Pb, La)(Zr, Ti)O_3 films prepared by aerosol-deposition method, IEEE Trans. Dielectr. Electr. Insul. 22 (3) (2015) 1477–1482.

[52] A. Kumar, S.H. Kim, A. Thakre, G. Lee, Y.G. Chae, J. Ryu, Increased energy-storage density and superior electric field and thermally stable energy efficiency of aerosol-deposited relaxor $(Pb_{0.89}La_{0.11})(Zr_{0.70}Ti_{0.30})O_3$ Films, J. Therm. Spray Technol. 30 (3) (2020) 591–602.

[53] X. Hao, P. Wang, X. Zhang, J. Xu, Microstructure and energy-storage performance of $PbO–B_2O_3–SiO_2–ZnO$ glass added $(Pb_{0.97}La_{0.02})(Zr_{0.97}Ti_{0.03})O_3$ antiferroelectric thick films, Mater. Res. Bull. 48 (1) (2013) 84–88.

[54] P. Zhao, H. Wang, L. Wu, L. Chen, Z. Cai, L. Li, X. Wang, High-performance relaxor ferroelectric materials for energy storage applications, Adv. Energy Mater. 9 (17) (2019) 1803048.

[55] V. Veerapandiyan, F. Benes, T. Gindel, M. Deluca, Strategies to improve the energy storage properties of perovskite lead-free relaxor ferroelectrics: a review, Materials 13 (24) (2020) 1–47.

[56] P. Zhao, S. Wang, H. Tang, X. Jian, X. Zhao, Y. Yao, T. Tao, B. Liang, S.-G. Lu, Superior energy storage density and giant negative electrocaloric effects in $(Pb_{0.98}La_{0.02})(Zr, Sn)O_3$ antiferroelectric ceramics, Scr. Mater. 200 (2021) 113920.

[57] J. Li, Z. Shen, X. Chen, S. Yang, W. Zhou, M. Wang, L. Wang, Q. Kou, Y. Liu, Q. Li, Z. Xu, Y. Chang, S. Zhang, F. Li, Grain-orientation-engineered multilayer ceramic capacitors for energy storage applications, Nat. Mater. 19 (9) (2020) 999–1005.

[58] J. Li, F. Li, Z. Xu, S. Zhang, Multilayer lead-free ceramic capacitors with ultrahigh energy density and efficiency, Adv. Mater. 30 (32) (2018) 1802155.

[59] H. Wang, Y. Liu, T. Yang, S. Zhang, Ultrahigh energy-storage density in antiferroelectric ceramics with field-induced multiphase transitions, Adv. Funct. Mater. 29 (7) (2019) 1807321.

Supplementary material

Energy-storage-efficient 0.9Pb($Mg_{1/3}Nb_{2/3}$)O_3–0.1$PbTiO_3$ thick films integrated directly onto stainless steel

Matej Sadl[1,2], Oana Andreea Condurache[1,2], Andreja Bencan[1,2], Mirela Dragomir[1], Uros Prah[1,2], Barbara Malic[1,2], Marco Deluca[3], Udo Eckstein[4], Daniel Hausmann[5], Neamul Hayet Khansur[4], Kyle G. Webber[4], and Hana Ursic[1,2,*]

[1]Electronic Ceramics Department, Jožef Stefan Institute, Jamova cesta 39, 1000 Ljubljana, Slovenia;

[2]Jožef Stefan International Postgraduate School, Jamova cesta 39, 1000 Ljubljana, Slovenia;

[3]Materials Center Leoben Forschung GmbH (MCL), Roseggerstrasse 12, 8700 Leoben, Austria;

[4]Department of Materials Science and Engineering, Friedrich-Alexander-Universität Erlangen-Nürnberg (FAU), 91058 Erlangen, Germany;

[5]Institute of General Material Properties, Friedrich-Alexander-Universität Erlangen-Nürnberg (FAU), 91058 Erlangen, Germany;

*Correspondence: hana.ursic@ijs.si

S1: Particle size analysis performed by laser granulometry

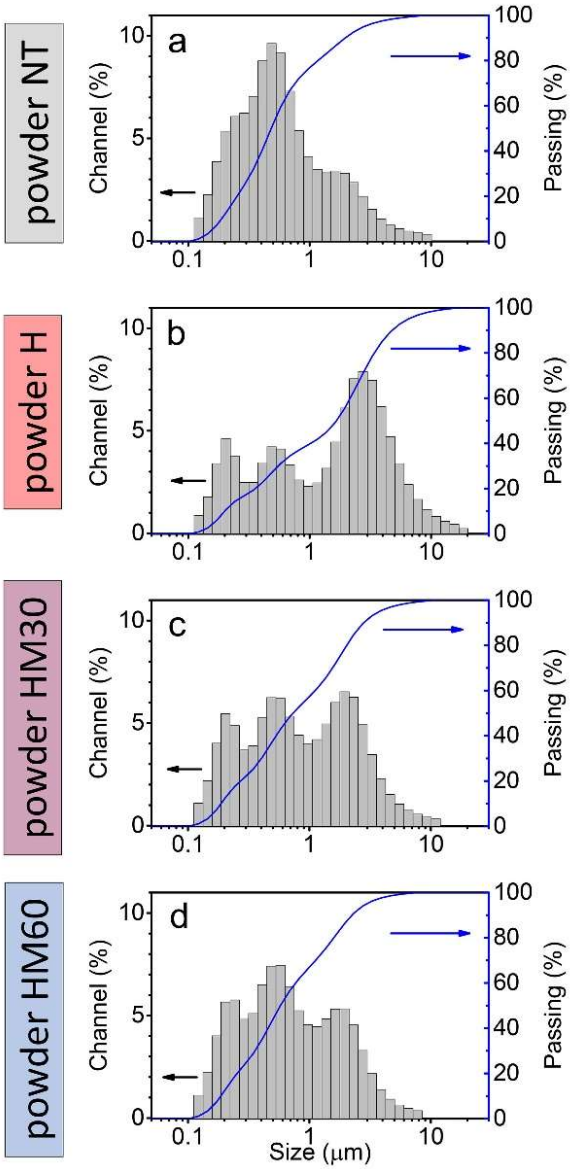

Figure S1: Volume particle size distributions (grey) and the cumulative curves (blue) of (a) NT, (b) H, (c) HM30 and (d) HM60 powders. The measurements were performed by laser granulometry.

S2: Selected-area electron diffraction analysis of HM60 powder

The transmission electron microscopy (TEM) and selected-area electron diffraction (SAED) analyses of the powders dispersed on a grid were performed with a JEM-2100 (Jeol, Japan).

A bright-field TEM image and a SAED pattern of the HM60 powder are shown in Figure S2. According to the SAED analysis, the selected few-hundred-nm-large powder particle is single crystalline [RS1], while its crystal structure matches best with the cubic Pb($Mg_{1/3}Nb_{2/3}$)O_3 structure (JCPDS 81-0861, $Pm\bar{3}m$ space group).

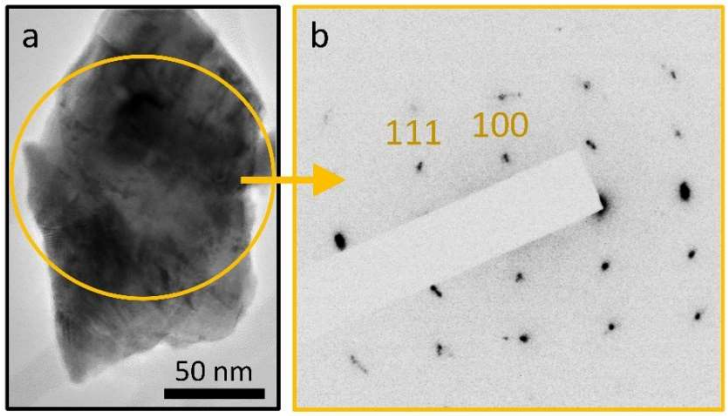

Figure S2: (a) Bright-field TEM and (b) SAED pattern of a single-crystalline particle in HM60 powder. The SAED pattern was taken from the circled area.

S3: Scanning electron microscopy of as-deposited and annealed films

Scanning electron microscopy (SEM) images of nano-porous regions in as-deposited and annealed PMN–10PT thick films in a cross-section view are shown in Figure S3a and S3b, respectively.

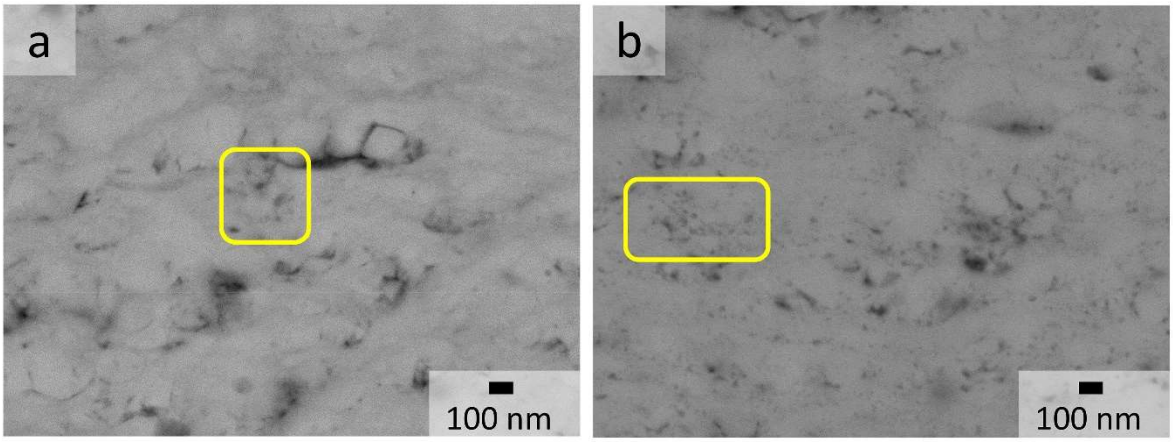

Figure S3: SEM images of (a) as-deposited and (b) annealed PMN–10PT thick films in cross-section with clearly visible nano-porous regions (marked with yellow rectangles).

S4: A comparison of energy storage properties in thick films

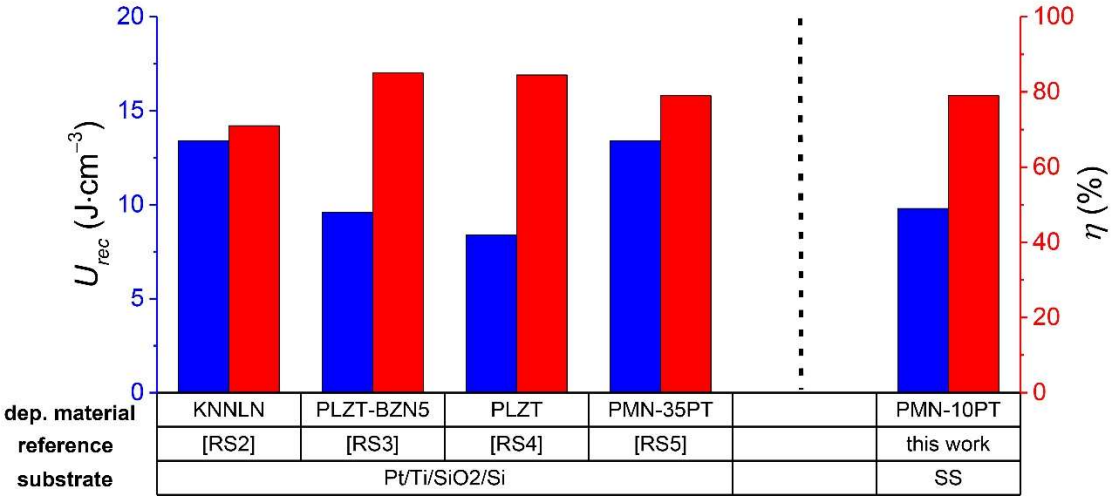

Figure S4: A comparison of energy storage properties in thick films from the literature. The graph shows the U_{rec} and η of annealed thick films at 900 kVcm^{-1}. In this work thick films were deposited on low-cost stainless-steel (SS), while other used platinized silicon (Pt/Ti/SiO_2/Si) as a substrate. Deposited thick films were 0.942[$Na_{0.535}K_{0.48}0NbO_3$]−0.058$LiNbO_3$ (KNNLN), 0.95($Pb_{0.92}La_{0.08}Zr_{0.52}Ti_{0.48}O_3$)-0.05Bi($Zn_{0.66}Nb_{0.33}O_3$) (PLZT-BZN5), ($Pb_{0.89}La_{0.11}$)($Zr_{0.70}Ti_{0.30}$)$O_3$ (PLZT), 0.65Pb($Mg_{1/3}Nb_{2/3}$)O_3-0.35$PbTiO_3$ (PMN-35PT) and 0.90Pb($Mg_{1/3}Nb_{2/3}$)O_3-0.10$PbTiO_3$ (PMN-10PT).

S5: Dielectric breakdown measurements

Dielectric breakdown measurements of as-deposited and annealed PMN–10PT thick films were performed using an aixACCT TF analyzer 2000 (aixACCT Systems GmbH, Germany) by applying a single sinusoidal unipolar waveform with a frequency of 100 Hz. To evaluate the dielectric breakdown fields (E_i), 7 electrodes of each sample were tested. The evaluated E_i follow the two-parameter Weibull distribution described by [RS6, RS7]:

$$X_i = \ln(E_i) \tag{S5.1}$$

$$Y_i = \ln(-\ln(1 - p_i)) \tag{S5.2}$$

$$p_i = \frac{i - 0.3}{N + 0.4} \tag{S5.3}$$

Here i, N and p_i represent the specimen sequential number, the sum of the tested specimens and the cumulative probability of dielectric breakdown, respectively. A high shape factor of Weibull distribution ($\beta > 1$) indicates low fluctuations of E_i in the as-deposited and annealed samples. Dielectric breakdown strength (DBS) is extracted from the intersection of the linear regression curve and the horizontal line ln(–ln(1–p_i)) = 0. It represents the electric field at which the breakdown probability is 63.2 %.

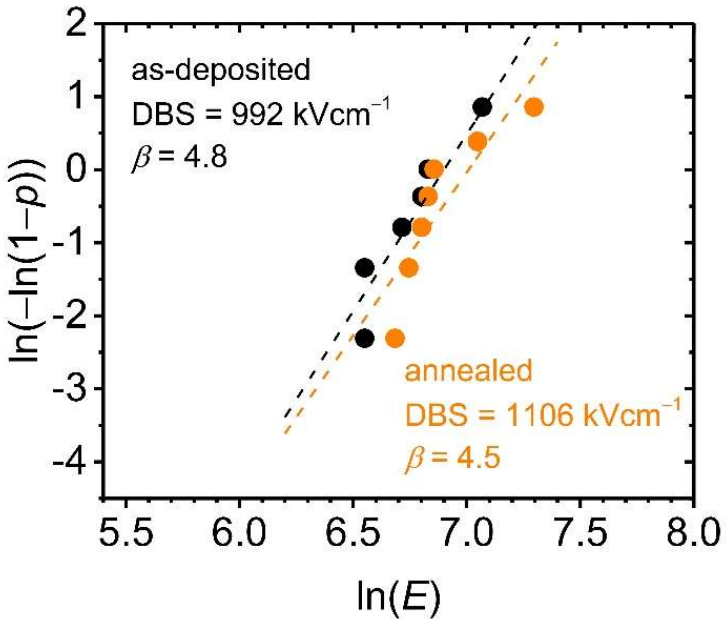

Figure S5: Weibull distribution of the dielectric breakdown field of as-deposited (black) and annealed (orange) PMN–10PT thick films. The dashed lines represent linear regression.

S6: Electric polarization vs. electric field hysteresis loops at varying temperature

Unipolar polarization–electric field (*P*–*E*) hysteresis loops of as-deposited and annealed PMN–10PT thick films at temperatures from 0 °C to 200 °C were measured at 500 kV·cm^{-1} and 100 Hz (Figure S6). The hysteresis losses of as-deposited film increase remarkably with increasing temperature, while in the annealed film the effect is far less evident.

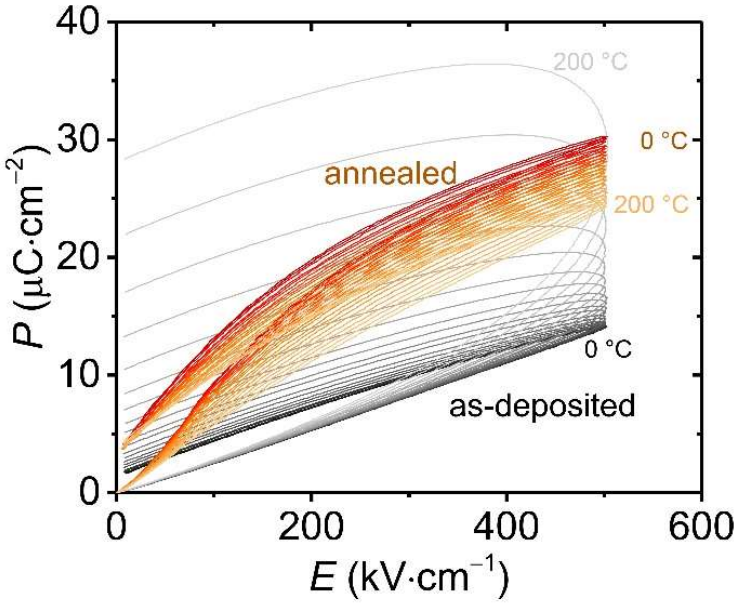

Figure S6: *P*–*E* loops of as-deposited (black-grey) and annealed (red-orange) PMN–10PT thick films at different temperatures (from 0 °C to 200 °C).

S7: Dielectric properties as a function of temperature

The dielectric losses (*tan δ*) and relative dielectric permittivity were measured between −50 °C and 150 °C with a Precision LCR impedance meter (HP 4284A, Hewlett-Packard, USA) in the frequency range 0.1–10 kHz (Figure S7).

Figure S7 reveals a remarkable increase of *tan δ* with increasing temperature in as-deposited films. This behavior is in agreement also with other aerosol deposited $BaTiO_3$ thick films [RS8]. The electrical response of as-deposited films is dominated by the defects, which are generated after AD. The reason for increase of *tan δ* with increasing temperature can be attributed to the relaxation of space charges, which become mobile at higher temperature. In this way, the AD process overshadows the electrical response of the material, which is recovered after annealing at 500 °C. The annealed films exhibit a decrease of *tan δ* in temperature range from −50 °C to 150 °C and a broad frequency-dependent dielectric permittivity maximum, which is also consistent with the material response of bulk PMN-10PT [RS9]. Similar decrease of *tan δ* is also observed in aerosol deposited $BaTiO_3$ thick films after annealing at 1000 °C [RS10].

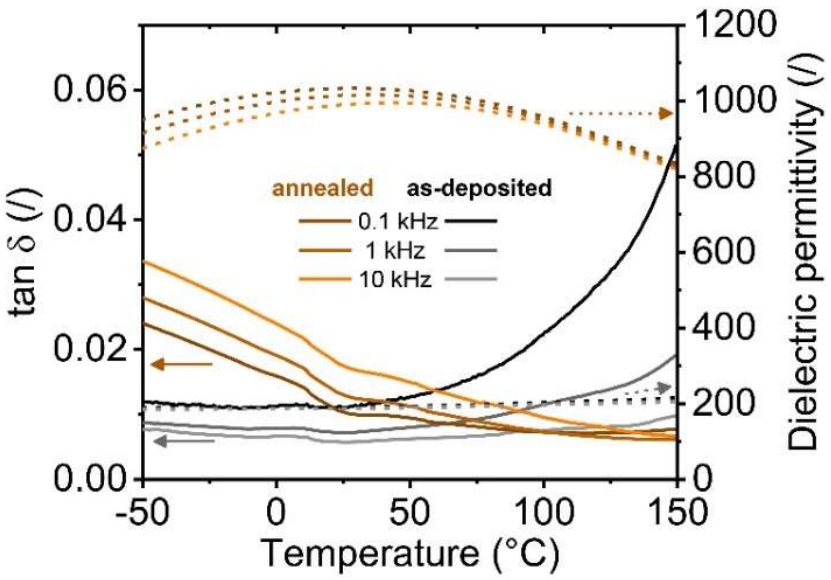

Figure S7: The *tan δ* (solid line) and relative dielectric permittivity (dashed line) vs. temperature of as-deposited (black-grey) and annealed (brown-orange) PMN–10PT films.

S8: Temperature-dependent conductive atomic force microscopy

Topography (height) and conductive atomic force microscopy (cAFM) images of as-deposited and annealed films were recorded with an atomic force microscope (AFM, Molecular Force Probe 3D, Asylum Research, USA) equipped with an ORCA mode. Prior to the cAFM experiment, the surface of the thick-film samples was fine-polished using a colloidal silica suspension. The final thicknesses of the as-deposited and annealed films were ~5 µm. Tetrahedral Si tips on Si cantilevers coated with Ti/Ir (Asyelec, AtomicForce F&E GmbH, Germany; curvature diameter of ~15 nm) were used. cAFM measurements were conducted by applying a DC voltage of 60 V between the tip and the SS substrate.

The cAFM images of as-deposited films (Figure S8) reveal an increase in the local electrical conductivity with increasing temperature. Up to 100 °C, the local electrical current flowing through the sample was below the detection limit of the cAFM technique (below ~1 pA) [RS11]. A rise in the local electrical current is visible above 100 °C, where the bright areas in Figures S8d and S8e represent the regions with an enhanced electrical current. Note that there is no signal correlation between the cAFM and topography images. In contrast, in annealed films, no increase in the local electrical current with increasing temperature is observed (Figure S8g–j).

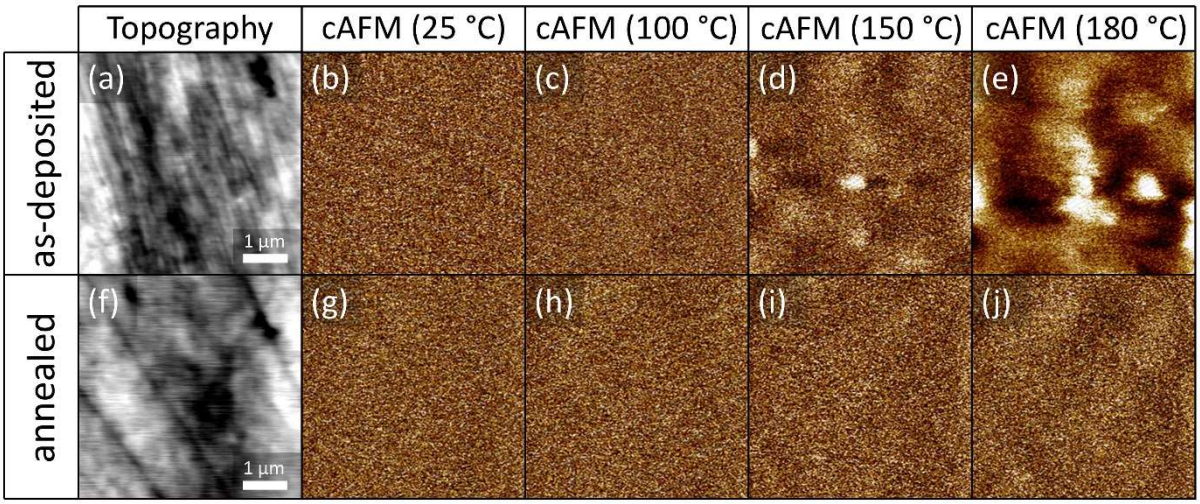

Figure S8: Topography (height) and cAFM images of (a–e) as-deposited and (f–j) annealed PMN–10PT films.

References

[RS1] D. B. Williams, and C. B. Carter, *Transmission Electron Microscopy: A Textbook for Materials Science*, Springer, 2009.

[RS2] M. Peddigari, H. Palneedi, G. T. Hwang, K. W. Lim, G. Y. Kim, D. Y. Jeong, and J. Ryu, "Boosting the Recoverable Energy Density of Lead-Free Ferroelectric Ceramic Thick Films through Artificially Induced Quasi-Relaxor Behavior," ACS Appl. Mater. Interfaces, vol. 10, no. 24, pp. 20720–20727, 2018.

[RS3] H.-B. Jung, J.-H. Lim, M. Peddigari, J. Ryu, D. H. Choi, and D.-Y. Jeong, "Enhancement of energy storage and thermal stability of relaxor $Pb_{0.92}La_{0.08}Zr_{0.52}Ti_{0.48}O_3$-$Bi(Zn_{0.66}Nb_{0.33})O_3$ thick films through aerosol deposition," J. Eur. Ceram. Soc., vol. 40, no. 1, pp. 63–70, 2020.

[RS4] A. Kumar, S. H. Kim, A. Thakre, G. Lee, Y. G. Chae, and J. Ryu, "Increased Energy-Storage Density and Superior Electric Field and Thermally Stable Energy Efficiency of Aerosol-Deposited Relaxor $(Pb_{0.89}La_{0.11})(Zr_{0.70}Ti_{0.30})O_3$ Films," J. Therm. Spray Technol., 2020.

[RS5] C. K. Park, S. H. Lee, J. H. Lim, J. Ryu, D. H. Choi, and D. Y. Jeong, "Nano-size grains and high density of 65PMN-35PT thick film for high energy storage capacitor," Ceram. Int., vol. 44, no. 16, pp. 20111–20114, 2018.

[RS6] E. Tuncer, D. R. James, I. Sauers, A. R. Ellis, and M. O. Pace, "On dielectric breakdown statistics," *J. Phys. D: Appl. Phys.*, vol. 39, no. 19, pp. 4257–4268, 2006.

[RS7] J. Li, Z. Shen, X. Chen, S. Yang, W. Zhou, M. Wang, L. Wang, Q. Kou, Y. Liu, Q. Li, Z. Xu, Y. Chang, S. Zhang, and F. Li, "Grain-orientation-engineered multilayer ceramic capacitors for energy storage applications," *Nat. Mater.*, vol. 19, no. 9, pp. 999–1005, 2020.

[RS8] N. H. Khansur, U. Eckstein, L. Benker, U. Deisinger, B. Merle, and K. G. Webber, "Room temperature deposition of functional ceramic films on low-cost metal substrate," *Ceram. Int.*, vol. 44, no. 14, pp. 16295–16301, 2018.

[RS9] M. Vrabelj, H. Uršič, Z. Kutnjak, B. Rožič, S. Drnovšek, A. Benčan, V. Bobnar, L. Fulanović, and B. Malič, "Large Electrocaloric Effect in Grain-Size-Engineered $0.9Pb(Mg_{1/3}Nb_{2/3})O_3$ –$0.1PbTiO_3$," *J. Eur. Ceram. Soc.*, vol. 36, no. 1, pp. 75–80, 2016.

[RS10] M. Suzuki, and J. Akedo, "Temperature Dependence of Dielectric Properties of Barium Titanate Ceramic Films Prepared by Aerosol Deposition Method" Jpn. J. Appl. Phys., Vol. 49, pp. 09MA10, 2010.

[RS11] Conductive AFM (ORCA), Asylum Research. Available online: https://afm.oxinst.com/products/mfp-3d-nanoelectrical-accessories/mfp-3d-orca-conductive-afm (accessed on 11 October 2020).

Chapter 3

Flexible Energy-Storage Ceramic Thick-Film Structures with High Flexural Fatigue Endurance

The integration of functional ceramics on flexible materials represents a major challenge in the development of flexible energy-storage devices. In this study, the relaxor-ferroelectric PMN–10PT thick films were aerosol-deposited on PI substrates coated with gold. The as-deposited and flexible PMN–10PT thick films were also thermally annealed at 400 °C. The effect of thermal annealing on the structural, microstructural and energy-storage properties as well as the bending tolerance of the thick films was investigated.

Thermal annealing had no effect on the grain size and porosity, which remained at 2% for both the as-deposited and the annealed thick films. The as-deposited thick films typically contained small crystallites (49 nm ± 13 nm) and a large amount of microstrain ($34.4 \cdot 10^{-4} \pm 6.3 \cdot 10^{-4}$). Thermal annealing did not increase the crystallite size but rather reduced the microstrain by 30%. The stress relaxation through thermal annealing is responsible for an established relaxor-ferroelectric behavior in the annealed films. The achieved high electric polarization, low hysteresis losses and high electric fields lead to promising energy-storage properties of the annealed thick films. The U_{rec} reaches 10 J · cm^{-3} and the η reaches 73% at 1000 kV · cm^{-1}.

The as-deposited and the annealed thick films were subjected to bending tests and the results showed high bendability and durability. The excellent stability of the energy-storage properties was confirmed after tensile bending to a radius of 3 mm (1.1% bending strain) and after repeating 10^5 bending cycles. The PMN–10PT thick films presented in this study are one of the first ceramic-polymer layered structures to provide high energy-storage performance and flexural endurance for future flexible energy-storage devices.

This chapter addresses thesis objectives 2, 3, 4, 5, 6 and 8.

Published in: M. Sadl, A. Lebar, J. Valentincic, and H. Ursic, "Flexible Energy-Storage Ceramic Thick-Film Structures with High Flexural Fatigue Endurance," *ACS Appl. Energy Mater.*, vol. 5, no. 6, pp. 6896–6902, 2022. (IF = 6.959, 2021)

My contribution: I synthesized the powder and used it in the aerosol-deposition process to prepare thick-film samples on PI foils. I annealed and prepared the samples, performed optical and scanning electron microscopy, XRD, Rietveld refinement analysis, static bending tests, electrical characterization and calculation of the energy-storage properties.

I elaborated the concept of the manuscript and wrote the paper, together with the co-authors.

ACS APPLIED ENERGY MATERIALS

www.acsaem.org Article

Flexible Energy-Storage Ceramic Thick-Film Structures with High Flexural Fatigue Endurance

Matej Sadl, Andrej Lebar, Josko Valentincic, and Hana Ursic*

Cite This: ACS Appl. Energy Mater. 2022, 5, 6896–6902 Read Online

ACCESS | Metrics & More | Article Recommendations | Supporting Information

ABSTRACT: When developing flexible electronic devices, trade-offs between desired functional properties and sufficient mechanical flexibility must often be considered. The integration of functional ceramics on flexible materials is a major challenge. However, aerosol deposition (AD), a room-temperature deposition method, has gained a reputation for its ability to combine ceramics with polymers previously considered incompatible with the conventional high-temperature sintering process. In this work, $0.9Pb(Mg_{1/3}Nb_{2/3})O_3–0.1PbTiO_3$ (PMN−10PT) thick films were deposited directly on a polyimide substrate using the AD method. As a result, dense and flexible relaxor-ferroelectric thick films were produced by a one-step direct-integration, suitable for large-scale production. After annealing of as-deposited PMN−10PT films at 400 °C, stress-relaxation occurs, which is responsible for the development of a relaxor-ferroelectric character. Achieved high polarization (38 $\mu C \cdot cm^{-2}$), high dielectric breakdown strength (~1000 $kV \cdot cm^{-1}$), and low hysteresis losses lead to improved recoverable energy density and energy-storage efficiency of the annealed thick films, reaching 10 $J \cdot cm^{-3}$ and 73% (at 1000 $kV \cdot cm^{-1}$), respectively. The thick films were subjected to flexural bending tests, which showed high flexibility (1.1% bending strain) and high durability (10^5 bending cycles). This stable energy-storage operation makes ceramic-polymer layered structures promising for integration into a wide range of flexible electronic devices.

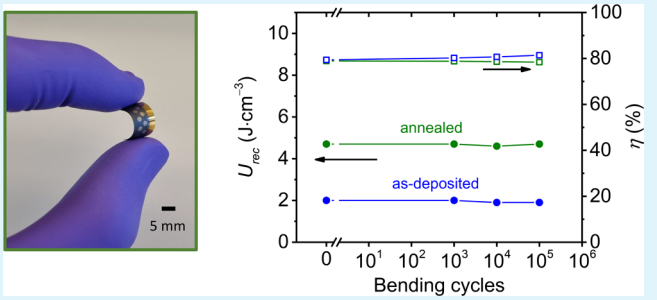

KEYWORDS: *flexible electronics, ceramic thick films, energy storage, aerosol deposition method, polyimide substrate, relaxor-ferroelectrics*

INTRODUCTION

For the transition to a low-carbon footprint society, the development of sustainable electrical energy-storage systems, such as batteries, electrochemical and dielectric capacitors, is of great importance. Electrical energy storage is becoming increasingly important because of the ever-increasing generation of electrical energy from intermittent renewable sources and the electrification of our energy-intensive world. Among electrical energy-storage systems, dielectric ceramic capacitors are simply structured and offer the fastest charge/discharge speed and powder density. These characteristics make them attractive for energy-storage devices in electronic applications requiring power in very short pulses and conditioning of large electric signals.[1]

Dielectric ceramic capacitors in the form of films have proven to be particularly advantageous as they offer very high energy density while allowing mechanical flexibility at the same time. By integrating films with high energy-storage performance on flexible substrates, one could meet the energy conversion needs for numerous flexible applications like electronic textiles, wearable and implantable medical electronics, easily integrable solar cells, and conformable sensor arrays.[2] To fabricate flexible energy-storage devices, high-energy storage films must be integrated on sufficiently flexible substrates. To ensure good flexibility, bendability, and pliability, polymers are often chosen as substrate materials. Applying rigid and brittle functional ceramics to flexible electronic devices represents a major challenge.

In general, two very different approaches can be used to fabricate functional films on flexible substrates: (1) transfer and bonding or (2) direct deposition.[2,3] The disadvantages of the first approach are the low surface area coverage and the high cost of the process, which makes it unsuitable for large-scale production. For this reason, many flexible electronic devices will tend to be fabricated by direct deposition.[3] Deposition of functional films on polymers by the latter approach is problematic because high annealing temperatures are required for densification and crystallization of the deposited films.[4] However, a relatively new method, aerosol deposition (AD), is gaining importance as it allows the deposition of fully dense

Received: February 17, 2022
Accepted: May 24, 2022
Published: June 7, 2022

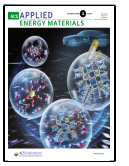

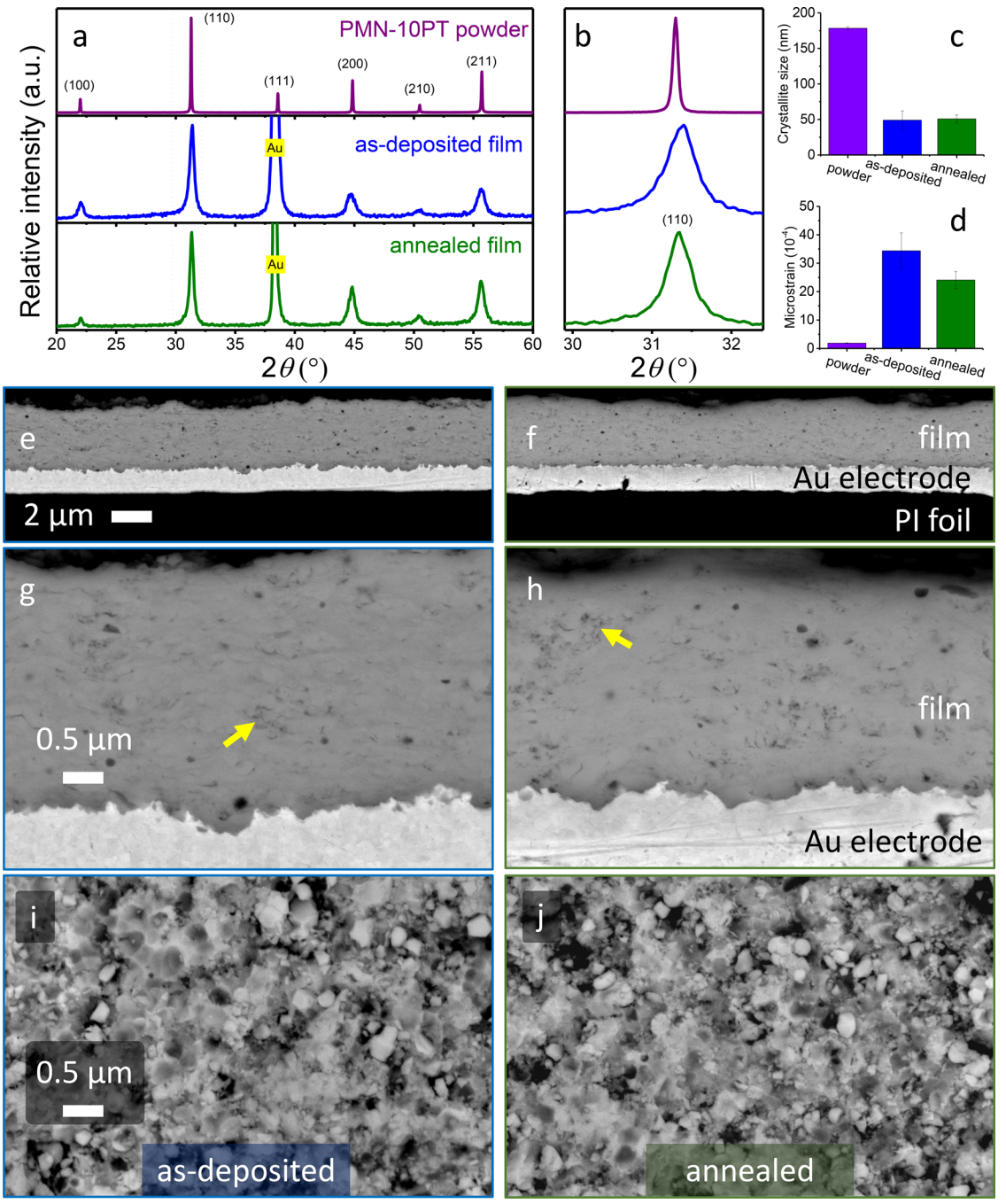

Figure 1. (a) XRD patterns of PMN−10PT powder and as-deposited and annealed thick films in the 2θ range of 20°−60° for; (b) (110) cubic reflection shown in close-up view. The corresponding (c) crystallite size and (d) microstrain calculated using Rietveld refinement. The SEM images in cross-section (e−h) and surface (i,j) views show as-deposited (e,g,i) and annealed (f,h,j) thick films. A few tens of nm sized pores are marked with yellow arrows.

ceramic films onto any substrate materials at room temperature.[5]

AD is a spray coating method viable of integrating ceramic thick films on polymers, thus enabling together the functionality of ceramics and the flexibility of polymers. AD is a rapid deposition method capable of depositing micrometer thick films in a matter of minutes.[5] In addition, this method can also be used to produce multilayers[6,7] and has the potential to be implemented on a large scale. In the AD process, dry and fine high-velocity particles are deposited onto the substrate by high-energy collisions. The bonding of the particles and densification are not achieved by thermal energy, but by a sufficiently high kinetic energy.[8,9] By mixing a desired powder with a carrier gas, an aerosol is formed. The deposition of aerosol occurs in the vacuum chamber by ejecting the aerosol through a micro-orifice nozzle.[5,10] Typically, AD thick films have very high density and exceptional adhesive properties. However, because of the particle consolidation through impacting, the films exhibit reduced crystallinity (on the order of tens of nanometers) and increased build-in compressive stresses.[11−13] Ceramic functional layers deposited using AD therefore often require a postdeposition annealing

https://doi.org/10.1021/acsaem.2c00518
ACS Appl. Energy Mater. 2022, 5, 6896−6902

step to increase crystallinity and reduce internal stresses in the film. However, the dielectric, ferroelectric, and other functional properties of the deposited materials improve significantly even when annealed at low temperatures (below 500 °C),[14] enabling the integration of inorganic materials even on polymer substrates. For this reason, AD can become a substantial process in the fabrication of flexible energy-storage devices.

In this work, we have developed flexible energy-storage ceramic thick-film structures with high flexural fatigue endurance. The relaxor-ferroelectric $0.9Pb(Mg_{1/3}Nb_{2/3})O_3-0.1PbTiO_3$ (PMN−10PT) material offers promising energy-storage performance because of low hysteresis loss, low remanent polarization, and high spontaneous polarization.[15,16] We have employed the AD method, which enables a room-temperature ceramic densification and integration with polymers; as a result, energy-storage thick films were produced on flexible foils. The newly fabricated thick film structures can withstand bending up to 3 mm bending radius and 10^5 bending cycles without noticeable degradation of energy-storage properties.

MATERIALS AND METHODS

The $0.9Pb(Mg_{1/3}Nb_{2/3})O_3-0.1PbTiO_3$ ceramic powder was prepared by mechanochemical-activation-assisted synthesis as described in ref 17. After the synthesis, the PMN−10PT powder was milled for 2 h, at 200 rpm in a planetary ball mill (PM 400, Retsch, Germany) using isopropanol and yttria-stabilized zirconia milling balls (diameters of 3 mm). After milling, the powder was heated at 900 °C (with 5 K·min^{-1} heating and cooling rates) for 1 h. After that, the powder was milled again for 1 h.

A commercial polyimide (PI) foil (Kapton HN, DuPont, Wilmington, Delaware, US) with a thickness of 125 μm was chosen as the substrate. The bottom Cr/Au electrode was deposited on the substrate (first 30 nm Cr, then ∼1 μm Au) using an RF-magnetron sputtering machine (5 Pascal, Italy). The PMN−10PT powder was sieved through a mesh (with 80 μm sized openings) and vacuum-dried at 100 °C for 12 h, before being aerosol deposited onto the substrate. The AD equipment was provided by InVerTec, Germany. The AD setup is presented in ref 18, while the process parameters of the AD are given in Supporting information S1. The deposited thick-film samples were cleaned with ethanol and annealed at 400 °C (with 2 K·min^{-1} heating and cooling rates) for 1 h. The annealing step is intended to release internal stresses developed in the thick films during AD. Further on, the samples are referred to as "as-deposited" and "annealed".

The powder and thick-film samples were analyzed by X-ray diffraction (XRD), which was carried out with a high-resolution diffractometer (X'Pert PRO, PANalytical, Netherlands) using Cu-Kα_1 radiation, Bragg−Brentano geometry, and a 100-channel X'Celerator detector. Diffraction patterns were recorded in a 2θ range of 10°−120° with a step of 0.017° and an integration time of 100 s per step. The Rietveld refinement of the diffraction patterns was performed by a Topas R package (version 2.1, Bruker AXS GmbH, Germany) with the details described in ref 17. The Fundamental Parameters Approach (FPA) was used to fit the line-profile of the powder and thick-film samples.[19] The FPA uses the geometrical properties of the diffraction experiment to build up the instrumental line width from first principles. It thus allows an explicit determination of the sample-dependent line-broadening contributions to the peak profile, which are dominated by the microstrain and broadening due to a decrease in the crystallite size.[20] The microstructure effects were modeled using the Double-Voigt approach.[21] The volume-weighted mean crystallite size was calculated based on the integral breath method incorporated in the Topas software.

The microstructures of the thick films were analyzed using a field-emission scanning electron microscope (FE SEM, JSM-7600F, JEOL, Japan). To analyze the thick films in cross-section, the samples were prepared by cutting, mounting in epoxy resin, grinding, and fine-polishing using a colloidal SiO_2 suspension. To prevent charging during the SEM analysis, a 3 nm-thick carbon coating was deposited on the samples using a Precision Etching and Coating System (PECS 682, Gatan, USA). Images of the thick films in cross-section were used to evaluate the film porosity and thickness. Image Tool software (ImageTool Version 3.00 UTHSCSA 2002)[22] was used to estimate the film porosity.

For the electrical measurements, the top Au electrodes (1.5 mm diameter) were deposited by RF-magnetron sputtering. The aixACCT TF analyzer 2000 (aixACCT Systems GmbH, Germany) was used to measure the polarization−electric field ($P-E$) hysteresis loops of the films. The waveform of the applied electric field was single, unipolar, and sinusoidal at 100 Hz. The $P-E$ loops were measured after bending tests were performed with an electric field of 500 kV·cm^{-1}.

The static tensile bending tests of thick-film samples were performed by conforming the thick film samples to steel cylinders with specific radii (ranging from 12 to 3 mm). The bending strain was calculated from the bend curvature using the multilayer model,[23,24] which is described in detail in Supporting information S2. The fatigue tensile bending tests were performed on a linear sliding moving stage. The custom-made sample holder enabled bending of free-standing samples (see Supporting Video). The minimum bending radius and bending frequency were kept constant at 3 mm and 1 Hz, respectively. The minimum bending radius was set using a 2D laser displacement sensor (sensor head LJ-G080, controller LJ-G5001, Keyence, Japan). The maximum bending cycles were 1×10^5.

RESULTS

At first, the as-deposited and annealed thick films were analyzed using SEM and XRD. The resulting XRD patterns of the PMN−10PT powder and as-deposited and annealed thick films are shown in Figure 1a,b. Every sample was indexed by a perovskite crystal structure, more exactly by $Pb(Mg_{1/3}Nb_{2/3})O_3$ with the $Pm\bar{3}m$ space group (JCPDS 81-0861). In addition, the XRD patterns of thick-film samples exhibit also Au reflections coming from the Au bottom electrode. A careful inspection of the XRD patterns did not reveal any secondary phases. Compared to the PMN−10PT powder, a remarkable broadening of the peaks is observed in the XRDs of the thick films. Such broadening originates from a microstrain and/or reduced crystallite size, often found in AD thick films due to collisions of powder particles during the AD process. A Rietveld refinement analysis of the XRD patterns was used to calculate the crystallite size and microstrain of the samples (Figure 1c,d). For the PMN−10PT powder, the crystallite size is 178 nm ± 2 nm and the microstrain is insignificant, that is, $1.9 \times 10^{-4} \pm 0.1 \times 10^{-4}$. These results are in agreement with the powder processing procedure.[17] After the AD process, which involves highly energetic particle collisions, the crystallite size of as-deposited films decreases to 49 nm ± 13 nm and the microstrain increases to $34.4 \times 10^{-4} \pm 6.3 \times 10^{-4}$. Further annealing of the films does not affect the crystallite size (51 nm ± 6 nm), but rather the microstrain, which decreases remarkably by 30% (to $24.1 \times 10^{-4} \pm 3.0 \times 10^{-4}$). Such a decrease in microstrain indicates significant stress relaxation. It is worth noting that stress relaxation also occurs in other aerosol-deposited ceramic thick films between the thermal annealing temperatures of 300[14] and 500 °C.[12,17,25−27] The crystallite size of the PMN−10PT powder and as-deposited thick films evaluated here by the Rietveld refinement method is consistent with previously reported transmission electron microscopy analysis.[17]

https://doi.org/10.1021/acsaem.2c00518
ACS Appl. Energy Mater. 2022, 5, 6896−6902

ACS Applied Energy Materials www.acsaem.org Article

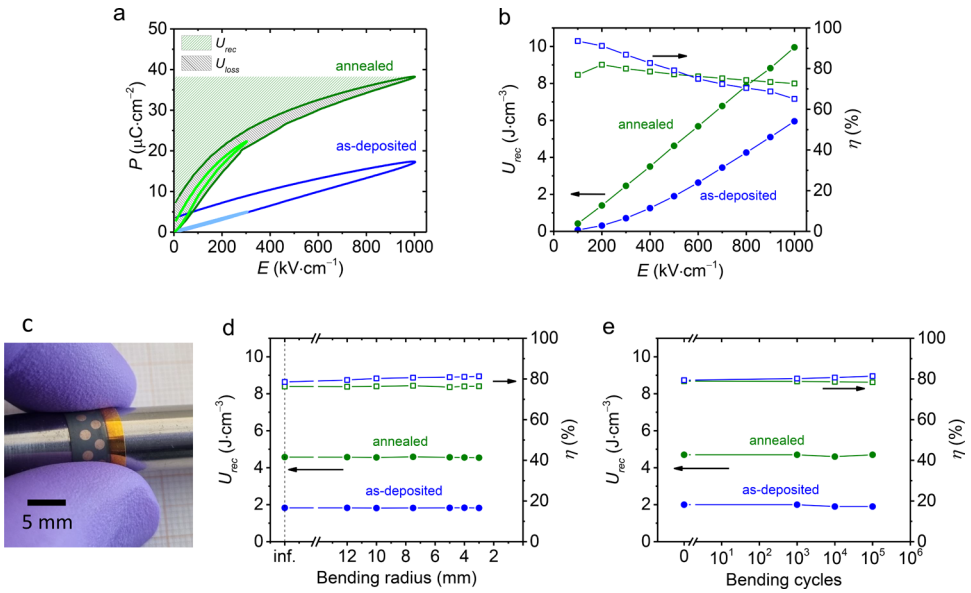

Figure 2. (a) Unipolar P–E hysteresis loops of as-deposited and annealed PMN–10PT thick films. The P–E loops measured up to 300 and 1000 kV·cm^{-1} are represented by light- and dark-colored curves, respectively. The U_{rec} and U_{loss} of the annealed film are represented by the green and gray patterned areas, respectively. (b) Electric-field dependence of U_{rec} and η for the as-deposited and annealed thick films. (c) Photograph of the sample under a tensile bending test. (d) U_{rec} and η values (at 500 kV·cm^{-1}) reaching different bend radii. (e) U_{rec} and η values (at 500 kV·cm^{-1}) as a function of bending cycles measured after the fatigue test (repetitive bending down to a radius of 3 mm). Lines between the data points are just a guide to the eye.

The SEM images of as-deposited (Figure 1e,g,i) and annealed films (Figure 1f,h,j) are shown in cross-sectional (Figure 1e–h) and surface view (Figure 1i,j). The cross-sectional images exhibit a high contrast, which allows easy distinction of the layered structure. Black, white, and gray layers represent the PI substrate, Au bottom electrode, and PMN–10PT films, respectively (Figure 1e,f). The thickness of the Au bottom electrode and PMN–10PT films is 1.3 and 3.4 μm, respectively. The as-deposited and the annealed films did not exhibit any notable difference in the microstructure. Both samples reveal high film density (the porosity reaches 2%) and excellent adhesion because there are no signs of delamination. The microstructure of both films includes nm-sized pores, which are designated by yellow arrows in Figure 1g,h. The SEM images in the surface view reveal dense films with an apparent surface roughness (Figure 1i,j).

Unipolar P–E hysteresis loops of the as-deposited and annealed films are shown in Figure 2a. The as-deposited films exhibit almost a linear dielectric behavior at a relatively low electric field of 300 kV·cm^{-1}. By increasing the electric field at 1000 kV·cm^{-1}, the P–E loop slightly opens, indicating increased hysteresis losses. The P–E characteristics of thick films are much different after annealing, which is a consequence of stress relaxation. The polarization increases and the loops obtain a relaxor-ferroelectric character. At 1000 kV·cm^{-1}, the P–E loop of annealed thick films exhibits a maximum polarization of 38 μC·cm^{-2} and slightly higher hysteresis losses compared to lower electric fields (300 kV·cm^{-1}), but opening of the hysteresis loop is not so extensive as for as-deposited films. Both, as-deposited and annealed thick films, exhibit P–E characteristics, which are promising for energy storage. In addition, both exhibit high dielectric breakdown strength (DBS), that is, 1085 and 986 kV·cm^{-1} in as-deposited and annealed thick films, respectively. More details about the DBS measurements can be found in Supporting information S3. Depending on the electric field range, each thick film can be used in specific applications. At high electric fields, annealed films exhibit especially high polarization, while as-deposited films show low hysteresis losses at low electric fields (up to 300 kV·cm^{-1}).

To evaluate the energy-storage performance of PMN–10PT thick films, we have calculated the recoverable energy density (U_{rec}) and energy storage efficiency (η). The U_{rec} represents the integrated area between the discharge curve and the ordinate, E = 0 (shown by the green patterned area in Figure 2a). However, the charging and discharging cycle is associated also with hysteresis losses, represented by the gray patterned area in Figure 2a. The η accounts also for the energy losses (U_{loss}) and is defined as the ratio between the recovered and stored energy: $\eta = U_{rec}/(U_{rec} + U_{loss})$.[1]

The dependence of the energy-storage properties (U_{rec} and η) on the electric field is shown in Figure 2b. For both samples, U_{rec} increases linearly with electric field. The as-deposited films exhibit very high efficiency at low electric fields. Up to 300 kV·cm^{-1}, the η exceeds 86%, but U_{rec} remains below 0.8 J·cm^{-3}. On the contrary, at high electric fields of 1000 kV·cm^{-1} the U_{rec} reaches 6.0 J·cm^{-3}, but the η drops to 65%. The annealing of the films stabilizes the drop of η with increasing electric field. In the electric field range from 300 to 1000 kV·cm^{-1}, the η decreases from 80 to 73%. The annealed thick films are interesting for energy storage at high fields because of their excellent U_{rec} performance, which reaches 10 J·cm^{-3} at 1000 kV·cm^{-1}. It should be noted that we have studied two extreme cases: as-deposited PMN–10PT thick films and films annealed at 400 °C. By annealing the films at a temperature lower than 400 °C, one can produce films with properties spanning between those of the as-deposited and annealed samples.

The flexibility of the thick films was evaluated by measuring the energy-storage properties after tensile bending of the thick films (Figure 2c). Visual inspection did not reveal any physical damage to the thick films after bending (Supporting information S4). Figure 2d shows U_{rec} and η (at 500 kV·

https://doi.org/10.1021/acsaem.2c00518
ACS Appl. Energy Mater. 2022, 5, 6896–6902

cm^{-1}) after reaching different bending radii. The results show excellent energy storage performance, which does not deteriorate after bending down to a radius of 3 mm, that is, a bending strain of 1.1%.

To evaluate the flexural fatigue tolerance of the films, additional repetitive tensile bending tests (down to a radius of 3 mm) were performed. The energy-storage properties were measured (at 500 kV·cm^{-1}) after 10^3, 10^4, and 10^5 repetitions (Figure 2e). The results show that U_{rec} and η remain very stable, that is, without any distinct fluctuations. The values remain almost constant with increasing bending cycles up to 10^5. After extensive bending tests, the as-deposited and annealed PMN−10PT thick films showed no performance degradation, which remarkably increases their potential for integration into a wide range of flexible electronic devices, especially as high-energy storage capacitors.

There are many reports in the literature about thin or thick films for energy storage, especially on rigid substrates, which are not suitable for flexible applications.[28−35] Another approach for designing flexible energy-storage devices is to use organic materials in the form of composite films[36−43] or other inorganic nonperovskites, such as fluorophlogopite mica.[44] The organic films perform well in mechanical tests but often require extremely high electric fields (i.e., several thousand kV·cm^{-1}) to achieve the same U_{rec} as ceramic perovskite films.[45] Some reports even address the integration of promising energy-storage materials on flexible substrates via a transfer and bonding approach.[46−50] The drawback of such an approach is the use of expensive and sophisticated methods that are difficult to integrate into large-scale production processes. For this reason, future research should focus on a direct deposition approach.

To compare the energy-storage performance of deposited films, one must also consider the film thickness, which has a significant impact on device design and operating conditions. Thin films less than 1 μm thick are often performing well, delivering very high volume-specific recoverable energy densities (U_{rec} reaches up to several tens of J·cm^{-3}), but their absolute recovered energy is rather low due to the thin film thickness.[1] Currently, there is a lack of scientific reports dealing with the integration of flexible thick-film structures (film thickness of at least several μm) for energy storage. To date, there is only one report on the fabrication of thick films for energy storage. In the mentioned report, the AD method enabled the integration of 8 μm-thick lanthanum-doped lead zirconate titanate on a flexible PI foil.[51] The U_{rec} values at 1000 kV·cm^{-1} reach about 7.3 J·cm^{-3}, which is lower than that of our PMN−10PT thick film after annealing (10 J·cm^{-3}). Other properties such as energy-storage efficiency and mechanical flexibility, which are important factors for the operation of flexible capacitors, were not evaluated in the mentioned report. Thus, a comprehensive review shows that the PMN−10PT thick films reported here are one of the first flexible thick films to provide high energy storage performance and mechanical reliability in flexible applications.

CONCLUSIONS

In this work, it was demonstrated that the integration of ceramic thick films on polymers is possible using the AD method, which attracts much attention nowadays because it operates at room temperature. We have adopted a novel and unique one-step direct-integration approach that allows combining electrical functionality and mechanical flexibility in integrated energy-storage devices. The AD of a few μm thick PMN−10PT films on a flexible PI substrate was successful. The SEM analysis shows a single-phase and dense microstructure with a porosity of only 2%. After annealing at 400 °C, the microstructure is preserved and the internal stresses relax. The Rietveld refinement shows no crystallite growth (the crystallite size remains at 50 nm), while the microstrain decreases by 30%. The AD enables high DBS (~1000 kV·cm^{-1}) in flexible PMN−10PT thick films, while stress relaxation after annealing is responsible for the development of a relaxor-ferroelectric character leading to high polarization of 38 μC·cm^{-2} at 1000 kV·cm^{-1}. Such high electric fields, high polarization, and low hysteresis losses result in promising energy-storage properties. In annealed films, the recoverable energy density reaches 10 J·cm^{-3} and an energy storage efficiency of 73% (at 1000 kV·cm^{-1}). The as-deposited and annealed thick film samples were subjected to bending tests, and the results showed high bendability and durability. The excellent stability of energy-storage properties was confirmed after tensile bending to a radius of 3 mm (1.1% bending strain) and after repeating 10^5 bending cycles. To conclude, the PMN−10PT thick-film structures presented here are one of the first ceramic-polymer layered structures to provide high energy storage performance and flexural endurance for future flexible energy-storage devices.

ASSOCIATED CONTENT

Supporting Information

The Supporting Information is available free of charge at https://pubs.acs.org/doi/10.1021/acsaem.2c00518.

(S1) AD process parameters, (S2) Bending strain, (S3) Dielectric breakdown measurements—Weibull analysis, and (S4) Optical micrographs of thick films surfaces (PDF)

Supporting video of repetitive tensile bending tests (MP4)

AUTHOR INFORMATION

Corresponding Author

Hana Ursic − *Electronic Ceramics Department, Jožef Stefan Institute, Ljubljana 1000, Slovenia; Jožef Stefan International Postgraduate School, Ljubljana 1000, Slovenia;* orcid.org/0000-0003-4525-404X; Email: hana.ursic@ijs.si

Authors

Matej Sadl − *Electronic Ceramics Department, Jožef Stefan Institute, Ljubljana 1000, Slovenia; Jožef Stefan International Postgraduate School, Ljubljana 1000, Slovenia;* orcid.org/0000-0003-1497-5610

Andrej Lebar − *Laboratory for Alternative Technologies, Faculty of Mechanical Engineering, University of Ljubljana, Ljubljana 1000, Slovenia; Faculty of Health Sciences, University of Ljubljana, Ljubljana 1000, Slovenia*

Josko Valentincic − *Laboratory for Alternative Technologies, Faculty of Mechanical Engineering, University of Ljubljana, Ljubljana 1000, Slovenia;* orcid.org/0000-0002-4911-1196

Complete contact information is available at: https://pubs.acs.org/10.1021/acsaem.2c00518

Notes

The authors declare no competing financial interest.

■ ACKNOWLEDGMENTS

The authors acknowledge the Slovenian Research Agency (research project J2-3058, young researcher project PR-08977, research core funding P2-0105 and P2-0248) and JSI Director's fund 2017-ULTRACOOL. They thank J. Cilenšek for the sample preparation for electron microscopy.

■ REFERENCES

(1) Palneedi, H.; Peddigari, M.; Hwang, G. T.; Jeong, D. Y.; Ryu, J. High-Performance Dielectric Ceramic Films for Energy Storage Capacitors: Progress and Outlook. *Adv. Funct. Mater.* **2018**, *28*, 1−33.

(2) Khanna, V. K. The Flexible Electronics Paradigm. In *Flexible Electronics*, vol *1*; IOP Publishing, 2019.

(3) Cheng, I.-C.; Wagner, S. Overview of Flexible Electronics Technology. In *Flexible Electronics: Materials and Applications*; Springer, 2009; pp 1−28.

(4) Han, S. T.; Peng, H.; Sun, Q.; Venkatesh, S.; Chung, K. S.; Lau, S. C.; Zhou, Y.; Roy, V. A. L. An Overview of the Development of Flexible Sensors. *Adv. Mater.* **2017**, *29*, 1−22.

(5) Hanft, D.; Exner, J.; Schubert, M.; Stöcker, T.; Fuierer, P.; Moos, R. An Overview of the Aerosol Deposition Method: Process Fundamentals and New Trends in Materials Applications. *J. Ceram. Sci. Technol.* **2015**, *6*, 147−181.

(6) Sadl, M.; Tomc, U.; Ursic, H. Investigating the Feasibility of Preparing Metal−Ceramic Multi-Layered Composites Using Only the Aerosol-Deposition Technique. *Materials* **2021**, *14*, 4548.

(7) Leupold, N.; Denneler, S.; Rieger, G.; Moos, R. Powder Treatment for Increased Thickness of Iron Coatings Produced by the Powder Aerosol Deposition Method and Formation of Iron−Alumina Multilayer Structures. *J. Therm. Spray Technol.* **2020**, *30*, 480−487.

(8) Chun, D.; Ahn, S. Deposition Mechanism of Dry Sprayed Ceramic Particles at Room Temperature Using a Nano-Particle Deposition System. *Acta Mater.* **2011**, *59*, 2693−2703.

(9) Saunders, R.; Johnson, S. D.; Schwer, D.; Patterson, E. A.; Ryou, H.; Gorzkowski, E. P. A Self-Consistent Scheme for Understanding Particle Impact and Adhesion in the Aerosol Deposition Process. *J. Therm. Spray Technol.* **2021**, *30*, 523−541.

(10) Akedo, J. Room Temperature Impact Consolidation (RTIC) of Fine Ceramic Powder by Aerosol Deposition Method and Applications to Microdevices. *J. Therm. Spray Technol.* **2008**, *17*, 181−198.

(11) Akedo, J.; Lebedev, M. Microstructure and Electrical Properties of Lead Zirconate Titanate ($Pb(Zr_{52}/Ti_{48})O_3$) Thick Films Deposited by Aerosol Deposition Method. *Jpn. J. Appl. Phys.* **1999**, *38*, 5397−5401.

(12) Khansur, N. H.; Eckstein, U.; Benker, L.; Deisinger, U.; Merle, B.; Webber, K. G. Room Temperature Deposition of Functional Ceramic Films on Low-Cost Metal Substrate. *Ceram. Int.* **2018**, *44*, 16295−16301.

(13) Schubert, M.; Exner, J.; Moos, R. Influence of Carrier Gas Composition on the Stress of Al_2O_3 Coatings Prepared by the Aerosol Deposition Method. *Materials* **2014**, *7*, 5633−5642.

(14) Khansur, N. H.; Eckstein, U.; Riess, K.; Martin, A.; Drnec, J.; Deisinger, U.; Webber, K. G. Synchrotron X-Ray Microdiffraction Study of Residual Stresses in $BaTiO_3$ Films Deposited at Room Temperature by Aerosol Deposition. *Scr. Mater.* **2018**, *157*, 86−89.

(15) Zhang, T. F.; Tang, X. G.; Liu, Q. X.; Jiang, Y. P.; Huang, X. X.; Zhou, Q. F. Energy-Storage Properties and High-Temperature Dielectric Relaxation Behaviors of Relaxor Ferroelectric $Pb(Mg_{1/3}Nb_{2/3})O_3$−$PbTiO_3$ Ceramics. *J. Phys. D: Appl. Phys.* **2016**, *49*, No. 095302.

(16) Uršič, H.; Vrabelj, M.; Otoničar, M.; Fulanović, L.; Rožič, B.; Kutnjak, Z.; Bobnar, V.; Malič, B. Influence of Synthesis-Related Microstructural Features on the Electrocaloric Effect for 0.9Pb-$(Mg_{1/3}Nb_{2/3})O_3$−$0.1PbTiO_3$ Ceramics. *Crystals* **2021**, *11*, 372.

(17) Sadl, M.; Condurache, O.; Bencan, A.; Dragomir, M.; Prah, U.; Malic, B.; Deluca, M.; Eckstein, U.; Hausmann, D.; Khansur, N. H.; Webber, K. G.; Ursic, H. Energy-Storage-Efficient 0.9Pb-$(Mg_{1/3}Nb_{2/3})O_3$−$0.1PbTiO_3$ Thick Films Integrated Directly onto Stainless Steel. *Acta Mater.* **2021**, *221*, No. 117403.

(18) Sadl, M.; Tomc, U.; Prah, U.; Ursic, H. Protective Alumina Coatings Prepared by Aerosol Deposition on Magnetocaloric Gadolinium Elements. *Inf. MIDEM - J. Microelectron. Electron. Components Mater.* **2019**, *49*, 177−182.

(19) Cheary, R. W.; Coelho, A. A Fundamental Parameters Approach to X-Ray Line-Profile Fitting. *J. Appl. Crystallogr.* **1992**, *25*, 109−121.

(20) Klug, H. P.; Alexander, L. E. *X-Ray Diffraction Procedures: For Polycrystalline and Amorphous Materials*, 2nd ed.; John Wiley & Sons: New York, 1974.

(21) Balzar, D.; Audebrand, N.; Daymond, M. R.; Fitch, A.; Hewat, A.; Langford, J. I.; Le Bail, A.; Louër, D.; Masson, O.; McCowan, C. N.; Popa, N. C.; Stephens, P. W.; Toby, B. H. Size-Strain Line-Broadening Analysis of the Ceria Round-Robin Sample. *J. Appl. Crystallogr.* **2004**, *37*, 911−924.

(22) Wilcox, D.; Dove, B.; McDavid, B.; Greer, D. *UTHSCSA Image Tool for Windows Version 3.0*; University of Texas Health Science Center: San Antonio, 2002.

(23) Mao, L.; Meng, Q.; Ahmad, A.; Wei, Z. Mechanical Analyses and Structural Design Requirements for Flexible Energy Storage Devices. *Adv. Energy Mater.* **2017**, *7*, No. 1700535.

(24) Park, S.; Xiong, Y.; Kim, R.-H.; Elvikis, P.; Meitl, M.; Kim, D.; Wu, J.; Yoon, J.; Yu, C.; Liu, Z.; Huang, Y.; Hwang, K.; Ferreira, P.; Li, X.; Choquette, K.; Rogers, J. A. Printed Assemblies of Inorganic Light-Emitting Diodes for Deformable and Semitransparent Displays. *Science* **2009**, *325*, 977−981.

(25) Zhuo, F.; Eckstein, U. R.; Khansur, N. H.; Dietz, C.; Urushihara, D.; Asaka, T.; Kakimoto, K.; Webber, K. G.; Fang, X.; Rödel, J. Temperature-induced Changes of the Electrical and Mechanical Properties of Aerosol-deposited $BaTiO_3$ Thick Films for Energy Storage Applications. *J. Am. Ceram. Soc.* **2022**, *105*, 4108−4121.

(26) Sadl, M.; Nadaud, K.; Bah, M.; Levassort, F.; Eckstein, U.; Khansur, N. H.; Webber, K. G.; Ursic, H. Multifunctional Energy Storage and Piezoelectric Properties of $0.65Pb(Mg_{1/3}Nb_{2/3})O_3$−$0.35PbTiO_3$ Thick Films on Stainless-Steel Substrates. *J. Phys. Energy* **2022**, *4*, No. 024004.

(27) Nadaud, K.; Sadl, M.; Bah, M.; Levassort, F.; Ursic, H. Effect of Thermal Annealing on Dielectric and Ferroelectric Properties of Aerosol-Deposited $0.65Pb(Mg_{1/3}Nb_{2/3})O_3$-$0.35PbTiO_3$ Thick Films. *Appl. Phys. Lett.* **2022**, *120*, 112902.

(28) Zhang, T.; Li, W.; Zhao, Y.; Yu, Y.; Fei, W. High Energy Storage Performance of Opposite Double-Heterojunction Ferroelectricity−Insulators. *Adv. Funct. Mater.* **2018**, *28*, 1−9.

(29) Lin, Z.; Chen, Y.; Liu, Z.; Wang, G.; Rémiens, D.; Dong, X. Large Energy Storage Density, Low Energy Loss and Highly Stable $(Pb_{0.97}La_{0.02})(Zr_{0.66}Sn_{0.23}Ti_{0.11})O_3$ Antiferroelectric Thin-Film Capacitors. *J. Eur. Ceram. Soc.* **2018**, *38*, 3177−3181.

(30) Fan, Q.; Liu, M.; Ma, C.; Wang, L.; Ren, S.; Lu, L.; Lou, X.; Jia, C.-L. Significantly Enhanced Energy Storage Density with Superior Thermal Stability by Optimizing $Ba(Zr_{0.15}Ti_{0.85})O_3/Ba(Zr_{0.35}Ti_{0.65})$-$O_3$ Multilayer Structure. *Nano Energy* **2018**, *51*, 539−545.

(31) Wang, Y.; Hao, X.; Yang, J.; Xu, J.; Zhao, D. Fabrication and Energy-Storage Performance of $(Pb,La)(Zr,Ti)O_3$ Antiferroelectric Thick Films Derived from Polyvinylpyrrolidone-Modified Chemical Solution. *J. Appl. Phys.* **2012**, *112*, No. 034105.

(32) Wang, X.; Zhang, L.; Hao, X.; An, S.; Song, B. Dielectric Properties and Energy-Storage Performances Films. *J. Mater. Sci.: Mater. Electron.* **2015**, *26*, 9583−9590.

(33) Peddigari, M.; Palneedi, H.; Hwang, G. T.; Lim, K. W.; Kim, G. Y.; Jeong, D. Y.; Ryu, J. Boosting the Recoverable Energy Density of Lead-Free Ferroelectric Ceramic Thick Films through Artificially Induced Quasi-Relaxor Behavior. *ACS Appl. Mater. Interfaces* **2018**, *10*, 20720−20727.

(34) Park, C. K.; Lee, S. H.; Lim, J. H.; Ryu, J.; Choi, D. H.; Jeong, D. Y. Nano-Size Grains and High Density of 65PMN-35PT Thick

https://doi.org/10.1021/acsaem.2c00518
ACS Appl. Energy Mater. 2022, 5, 6896−6902

Film for High Energy Storage Capacitor. *Ceram. Int.* **2018**, *44*, 20111−20114.
(35) Jung, H.-B.; Lim, J.-H.; Peddigari, M.; Ryu, J.; Choi, D. H.; Jeong, D.-Y. Enhancement of Energy Storage and Thermal Stability of Relaxor $Pb_{0.92}La_{0.08}Zr_{0.52}Ti_{0.48}O_3$-$Bi(Zn_{0.66}Nb_{0.33})O_3$ Thick Films through Aerosol Deposition. *J. Eur. Ceram. Soc.* **2020**, *40*, 63−70.
(36) Li, Q.; Liu, F.; Yang, T.; Gadinski, M. R.; Zhang, G.; Chen, L. Q.; Wang, Q. Sandwich-Structured Polymer Nanocomposites with High Energy Density and Great Charge-Discharge Efficiency at Elevated Temperatures. *Proc. Natl. Acad. Sci. U. S. A.* **2016**, *113*, 9995−10000.
(37) Luo, B.; Wang, X.; Wang, Y.; Li, L. Fabrication, Characterization, Properties and Theoretical Analysis of Ceramic/PVDF Composite Flexible Films with High Dielectric Constant and Low Dielectric Loss. *J. Mater. Chem. A* **2014**, *2*, 510−519.
(38) Jung, H. B.; Kim, J. W.; Lim, J. H.; Kwon, D. K.; Choi, D. H.; Jeong, D. Y. Energy Storage Properties of Blended Polymer Films with Normal Ferroelectric P(VDF-HFP) and Relaxor Ferroelectric P(VDF-TrFE-CFE). *Electron. Mater. Lett.* **2020**, *16*, 47−54.
(39) Li, Q.; Chen, L.; Gadinski, M. R.; Zhang, S.; Zhang, G.; Li, H. U.; Iagodkine, E.; Haque, A.; Chen, L.-Q.; Jackson, T. N.; Wang, Q. Flexible High-Temperature Dielectric Materials from Polymer Nanocomposites. *Nature* **2015**, *523*, 576−579.
(40) Hu, P.; Shen, Y.; Guan, Y.; Zhang, X.; Lin, Y.; Zhang, Q.; Nan, C.-W. Topological-Structure Modulated Polymer Nanocomposites Exhibiting Highly Enhanced Dielectric Strength and Energy Density. *Adv. Funct. Mater.* **2014**, *24*, 3172−3178.
(41) Luo, H.; Zhang, D.; Wang, L.; Chen, C.; Zhou, J.; Zhou, K. Highly Enhanced Dielectric Strength and Energy Storage Density in Hydantoin@$BaTiO_3$−P(VDF-HFP) Composites with a Sandwich-Structure. *RSC Adv.* **2015**, *5*, 52809−52816.
(42) Singh, P.; Borkar, H.; Singh, B. P.; Singh, V. N.; Kumar, A. Ferroelectric Polymer-Ceramic Composite Thick Films for Energy Storage Applications. *AIP Adv.* **2014**, *4*, No. 087117.
(43) Zhang, X.; Shen, Y.; Shen, Z.; Jiang, J.; Chen, L.; Nan, C. W. Achieving High Energy Density in PVDF-Based Polymer Blends: Suppression of Early Polarization Saturation and Enhancement of Breakdown Strength. *ACS Appl. Mater. Interfaces* **2016**, *8*, 27236−27242.
(44) Xu, X.; Liu, W.; Li, Y.; Wang, Y.; Yuan, Q.; Chen, J.; Ma, R.; Xiang, F.; Wang, H. Flexible Mica Films for High-Temperature Energy Storage. *J. Mater.* **2018**, *4*, 173−178.
(45) Yao, Z.; Song, Z.; Hao, H.; Yu, Z.; Cao, M.; Zhang, S.; Lanagan, M. T.; Liu, H. Homogeneous/Inhomogeneous-Structured Dielectrics and Their Energy-Storage Performances. *Adv. Mater.* **2017**, *29*, No. 1601727.
(46) Gao, W.; Zhu, Y.; Wang, Y.; Yuan, G.; Liu, J. M. A Review of Flexible Perovskite Oxide Ferroelectric Films and Their Application. *J. Mater.* **2020**, *6*, 1−16.
(47) Azizi, A.; Gadinski, M. R.; Li, Q.; AlSaud, M. A.; Wang, J.; Wang, Y.; Wang, B.; Liu, F.; Chen, L. Q.; Alem, N.; Wang, Q. High-Performance Polymers Sandwiched with Chemical Vapor Deposited Hexagonal Boron Nitrides as Scalable High-Temperature Dielectric Materials. *Adv. Mater.* **2017**, *29*, 1−7.
(48) Michael-Sapia, E. K.; Li, H. U.; Jackson, T. N.; Trolier-McKinstry, S. Nanocomposite Bismuth Zinc Niobate Tantalate for Flexible Energy Storage Applications. *J. Appl. Phys.* **2015**, *118*, 234102.
(49) Li, Y.; Geng, W.; Zhang, L.; Yang, X.; Qiao, X.; Zheng, D.; Zhang, L.; He, J.; Hou, X.; Chou, X. Flexible PLZT Antiferroelectric Film Capacitor for Energy Storage in Wide Temperature Range. *J. Alloys Compd.* **2021**, *868*, No. 159129.
(50) Peddigari, M.; Park, J. H.; Han, J. H.; Jeong, C. K.; Jang, J.; Min, Y.; Kim, J. W.; Ahn, C. W.; Choi, J. J.; Hahn, B. D.; Park, S. Y.; Yoon, W. H.; Park, D. S.; Jeong, D. Y.; Ryu, J.; Lee, K. J.; Hwang, G. T. Flexible Self-Charging, Ultrafast, High-Power-Density Ceramic Capacitor System. *ACS Energy Lett.* **2021**, *6*, 1383−1391.
(51) Ma, B.; Lee, T. H.; Dorris, S. E.; Koritala, R. E.; Balachandran, U. Flexible Ceramic Film Capacitors for High-Temperature Power Electronics. *Mater. Sci. Energy Technol.* **2019**, *2*, 96−103.

https://doi.org/10.1021/acsaem.2c00518
ACS Appl. Energy Mater. 2022, 5, 6896−6902

Supporting Information

Flexible energy-storage ceramic thick-film structures with high flexural fatigue endurance

Matej Sadl[1,2], Andrej Lebar[3,4], Josko Valentincic[3] and Hana Ursic[1,2,*]

[1]Electronic Ceramics Department, Jožef Stefan Institute, Jamova cesta 39, 1000 Ljubljana, Slovenia;

[2]Jožef Stefan International Postgraduate School, Jamova cesta 39, 1000 Ljubljana, Slovenia;

[3]Laboratory for Alternative Technologies, Faculty of Mechanical Engineering, University of Ljubljana, Aškerčeva cesta 6, 1000 Ljubljana, Slovenia;

[4]Faculty of Health Sciences, University of Ljubljana, Zdravstvena pot 5, 1000 Ljubljana, Slovenia.

*Correspondence: hana.ursic@ijs.si

S1: Aerosol deposition process parameters

Table S1. Process parameters used during the AD.

Process Parameters	
Carrier gas species	N_2
Nozzle geometry (slit size)	(0.5 × 10) mm^2
Distance between nozzle and substrate	5 mm
Sweep speed	5 $mm \cdot s^{-1}$
Gas flow rate	4 $L \cdot min^{-1}$
Pressure in aerosol chamber	180 mbar
Pressure in deposition chamber	2 mbar

S2: Bending strain

The bending strain of the thick film surface dependents on the bend curvature and was calculated by using the multilayer model.[1,2] In the thick film multilayer structure there is a neutral mechanical plane, where the bending strain is zero. The distance between the neutral mechanical plane and the film surface is given by equation (1):

$$b = \frac{\sum_{i=1}^{N} \bar{E}_i \, h_i \left[\left(\sum_{j=1}^{i} h_j \right) - \frac{h_i}{2} \right]}{\sum_{i=1}^{N} \bar{E}_i \, h_i} \quad (1)$$

where N is the total number of layers and h_i is the thickness of the i^{th} layer (from the top). $\bar{E}_i$ is equal to $E_i/(1-\nu_i^2)$, where E_i and ν_i are Young's modulus and Poisson's ratio of the i^{th} layer, respectively. The bending strain in the multilayer structure can be calculated by equation (2):

$$\varepsilon = \frac{y}{R} \tag{2}$$

where R is the bend radius and y the distance from the neutral mechanical plane. Thus, the highest bending strains are on the film's surface, where y equals b. All parameters needed for the calculation of the bending strain are given in the Table S2. E_i and ν_i values were taken from the given references. Note, that the Young's modulus of AD thick films depends on the thermal treatment, which was confirmed for aerosol-deposited $BaTiO_3$ thick films thermally annealed at 500 °C.[3] After thermal annealing of $BaTiO_3$ thick films at 500 °C, the Young's modulus increased by about 15%. However, since there are no similar studies on aerosol-deposited PMN–10PT thick films, we did not consider the changes in Young's modulus after thermal annealing. The calculated bending strain for different bending radii used in the evaluation of flexibility can be found in Table S3.

Table S2. Elastic properties and layer thicknesses.

i	1	2	3
layer	PMN–10PT thick film	Au bottom electrode	polyimide substrate (Kapton® HN)
h_i (µm)	3.4	1.3	125
E_i (GPa)	90	78	2.76
ν_i	0.30	0.43	0.34
reference	[4]	[5]	[6]

Table S3. The calculated bending strain for different bending radii.

Bending radius (mm)	Bending strain (%)
12	0.27
10	0.32
7.5	0.43
5.0	0.64
4.0	0.80
3.0	1.07

S3: Dielectric breakdown measurements – Weibull analysis

Dielectric breakdown measurements of as-deposited and annealed PMN–10PT thick films were performed using an aixACCT TF analyzer 2000 (aixACCT Systems GmbH, Germany) by applying a single sinusoidal unipolar waveform with a frequency of 100 Hz. To evaluate the dielectric breakdown fields (E_i), 12 Au top electrodes (1.5 mm diameter) of each sample were used. The evaluated E_i follow the two-parameter Weibull distribution described by:[7,8]

$$X_i = \ln(E_i) \tag{3}$$

$$Y_i = \ln(-\ln(1 - p_i)) \tag{4}$$

$$p_i = \frac{i - 0.3}{N + 0.4} \tag{5}$$

Here i, N and p_i represent the specimen sequential number, the sum of the tested specimens and the cumulative probability of dielectric breakdown, respectively. A high shape factor ($\beta > 1$), determined from the slope of the Weibull distribution, indicates low fluctuations of E_i in the as-deposited and annealed samples. The dielectric breakdown strength (DBS) is extracted from the intersection of the linear regression curve and the horizontal line $\ln(-\ln(1-p_i)) = 0$. It represents the electric field at which the breakdown probability is 63.2%.

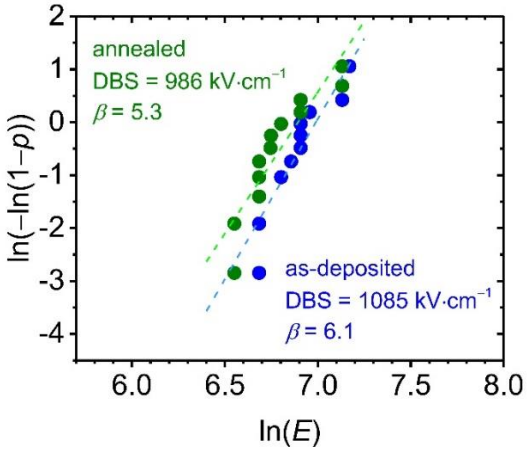

Figure S1: Weibull distribution of the dielectric breakdown field of as-deposited (blue) and annealed (green) PMN–10PT thick films. The dashed lines represent linear regression.

S4: Optical micrographs of thick films surfaces

Optical micrographs of the thick film surfaces were taken using an optical microscope Axio Imager A1 m, Carl Zeiss, Germany. Figure S2 shows micrographs of the as-deposited and annealed thick films before and after bending to a minimum radius of 3 mm and 10^5 cycles. No obvious cracks or other damage could be detected after bending.

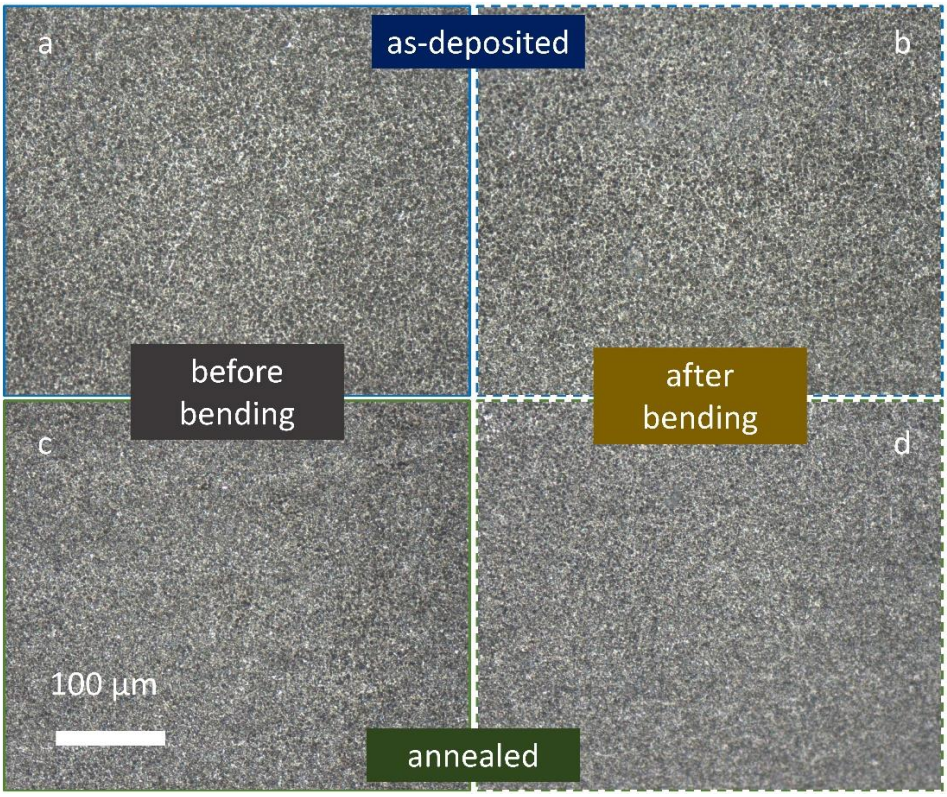

Figure S2: Micrographs of the surface of as-deposited (a, b) and annealed (c, d) thick films before (a, c) and after (b, d) bending.

Supporting video

The supporting video shows fatigue tensile bending tests of PMN–10PT thick films performed on a linear sliding moving stage and a custom made sample holder.

References

(1) Mao, L.; Meng, Q.; Ahmad, A.; Wei, Z. Mechanical Analyses and Structural Design Requirements for Flexible Energy Storage Devices. *Adv. Energy Mater.* **2017**, *7* (23), 1700535. https://doi.org/10.1002/aenm.201700535.

(2) Park, S. Il; Xiong, Y.; Kim, R. H.; Elvikis, P.; Meitl, M.; Kim, D. H.; Wu, J.; Yoon, J.; Chang-Jae, Y.; Liu, Z.; Huang, Y.; Hwang, K. C.; Ferreira, P.; Xiuling, L.; Choquette, K.; Rogers, J. A. Printed Assemblies of Inorganic Light-Emitting Diodes for Deformable and Semitransparent Displays. *Science* **2009**, *325* (5943), 977–981. https://doi.org/10.1126/science.1175690.

(3) Zhuo, F.; Eckstein, U.; Khansur, N. H.; Dietz, C.; Urushihara, D.; Asaka, T.; Kakimoto, K.; Webber, K. G.; Fang, X.; Rödel, J. Temperature-induced Changes of the Electrical and Mechanical Properties of Aerosol-deposited $BaTiO_3$ Thick Films for Energy Storage Applications. *J. Am. Ceram. Soc.* **2022**, *105* (6), 4108–4121. https://doi.org/10.1111/jace.18377.

(4) Uršič, H.; Hrovat, M.; Holc, J.; Zarnik, M. S.; Drnovšek, S.; Maček, S.; Kosec, M. A Large-Displacement $65Pb(Mg_{1/3}Nb_{2/3})O_3$–$35PbTiO_3$/Pt Bimorph Actuator Prepared by Screen Printing. *Sensors Actuators B Chem.* **2008**, *133* (2), 699–704. https://doi.org/10.1016/j.snb.2008.04.004.

(5) Faurie, D.; Renault, P.-O.; Le Bourhis, E.; Villain, P.; Goudeau, P.; Badawi, F. Measurement of Thin Film Elastic Constants by X-Ray Diffraction. *Thin Solid Films* **2004**, *469–470*, 201–205. https://doi.org/10.1016/j.tsf.2004.08.097.

(6) DuPont. DuPont™ Kapton® HN https://www.dupont.com/content/dam/dupont/amer/us/en/products/ei-transformation/documents/DEC-Kapton-HN-datasheet.pdf. (last accessed 25.1.2022)

(7) Tuncer, E.; James, D. R.; Sauers, I.; Ellis, A. R.; Pace, M. O. On Dielectric Breakdown Statistics. *J. Phys. D. Appl. Phys.* **2006**, *39* (19), 4257–4268. https://doi.org/10.1088/0022-3727/39/19/020.

(8) Li, J.; Shen, Z.; Chen, X.; Yang, S.; Zhou, W.; Wang, M.; Wang, L.; Kou, Q.; Liu, Y.; Li, Q.; Xu, Z.; Chang, Y.; Zhang, S.; Li, F. Grain-Orientation-Engineered Multilayer Ceramic Capacitors for Energy Storage Applications. *Nat. Mater.* **2020**, *19* (9), 999–1005. https://doi.org/10.1038/s41563-020-0704-x.

Chapter 4

Multifunctional Energy Storage and Piezoelectric Properties of $0.65Pb(Mg_{1/3}Nb_{2/3})O_3$–$0.35PbTiO_3$ Thick Films on Stainless-Steel Substrates

In this study, ferroelectric PMN–35PT thick films were deposited on SS substrates using the room-temperature AD method. After deposition, the thick films were thermally annealed at 500 °C and the structural, microstructural, energy-storage and piezoelectric properties of the as-deposited and the annealed thick films were investigated. Thermal annealing did not result in any microstructural changes; the density of the films remained very high (porosity of only ~3%). The high-impact particle collisions in the AD process are responsible for an 8-fold decrease of the crystallite size in the as-deposited thick films (from 146 nm ± 3 nm in the powder to 17.2 nm ± 0.3 nm in the as-deposited films). Thermal annealing of the films has little effect on the crystallite size, but a remarkable one on the microstrain, which decreases by 41% (from $22.7 \cdot 10^{-4} \pm 2.1 \cdot 10^{-4}$ in the as-deposited films to $13.4 \cdot 10^{-4} \pm 1.2 \cdot 10^{-4}$ in the annealed films).

Due to the similar and dense microstructure, both the as-deposited and annealed PMN–35PT thick films achieve similar and very high electric fields (1350 $kV \cdot cm^{-1}$). However, the stress relaxation after thermal annealing is responsible for the evolution from a lossy dielectric behavior in the as-deposited films to a relaxor-ferroelectric behavior in the annealed films. The thermally annealed thick films achieve a U_{rec} of 15.1 $J \cdot cm^{-3}$ and an η of 55% at 1350 $kV \cdot cm^{-1}$, while both the as-deposited and annealed films exhibit an electric-field cycling stability of 5 million cycles.

A piezoelectric response was confirmed throughout the thickness of both the as-deposited and annealed PMN–35PT thick films. Macroscopic electromechanical measurements on the annealed films revealed a maximum strain response of 0.38% and an inverse effective piezoelectric coefficient ($d^*_{33\,eff}$) of 41 $pm \cdot V^{-1}$ at 1000 $kV \cdot cm^{-1}$. However, this piezoelectric coefficient is lower than that of PMN–35PT ceramics (typically above 525 $pC \cdot N^{-1}$) and screen-printed PMN–35PT thick films (typically between 130 and 170 $pC \cdot N^{-1}$), which is due to a strong film-substrate clamping effect and a much smaller grain size in AD thick films.

In summary, it has been shown that the integration of PMN–35PT thick films on SS is possible and that such integration enables multifunctional ceramic-metal structures, since the deposited PMN–35PT thick films exhibit an energy-storage capability and piezoelectric properties.

This chapter addresses thesis objectives 2, 3, 4, 5, 6 and 7.

Published in: M. Sadl, K. Nadaud, M. Bah, F. Levassort, U. Eckstein, N. H. Khansur, K. G. Webber, and H. Ursic, "Multifunctional energy storage and piezoelectric properties of $0.65Pb(Mg_{1/3}Nb_{2/3})O_3$–$0.35PbTiO_3$ thick films on stainless-steel substrates," *J. Phys. Energy*, vol. 4, no. 2, p. 024004, 2022. (IF = 7.528, 2021)

My contribution: I synthesized the powder and used it in the aerosol-deposition process to prepare thick-film samples on SS. I annealed and prepared the samples, performed scanning electron microscopy, XRD, Rietveld refinement analysis, electrical, electro-mechanical and impedance characterization and calculation of the energy-storage properties. I elaborated the concept of the manuscript and wrote the paper, together with the co-authors.

IOP Publishing J. Phys. Energy 4 (2022) 024004 https://doi.org/10.1088/2515-7655/ac5fd5

Journal of Physics: Energy

OPEN ACCESS

RECEIVED
23 December 2021

REVISED
8 March 2022

ACCEPTED FOR PUBLICATION
22 March 2022

PUBLISHED
7 April 2022

PAPER

Multifunctional energy storage and piezoelectric properties of $0.65Pb(Mg_{1/3}Nb_{2/3})O_3$–$0.35PbTiO_3$ thick films on stainless-steel substrates

Matej Sadl[1,2], Kevin Nadaud[3], Micka Bah[3], Franck Levassort[3], Udo Eckstein[4], Neamul H Khansur[4], Kyle G Webber[4] and Hana Ursic[1,2,*]

[1] Electronic Ceramics Department, Jožef Stefan Institute, Jamova cesta 39, 1000 Ljubljana, Slovenia
[2] Jožef Stefan International Postgraduate School, Jamova cesta 39, 1000 Ljubljana, Slovenia
[3] GREMAN UMR 7347, Université de Tours, CNRS, INSA CVL, 16 rue Pierre et Marie Curie, 37071 Tours Cedex 2, France
[4] Department of Materials Science and Engineering, Friedrich-Alexander-Universität Erlangen-Nürnberg (FAU), 91058 Erlangen, Germany
* Author to whom any correspondence should be addressed.

E-mail: hana.ursic@ijs.si

Keywords: multifunctional, piezoelectric, energy storage, aerosol deposition, stainless steel, PMN-PT

Supplementary material for this article is available online

Abstract

The miniaturization of electronic devices and power systems requires the fabrication of functional components in the form of micrometer-sized thick films. A major challenge is the integration of functional ceramics with metals, which are considered incompatible with high-temperature ceramic processing. To overcome the integration barrier, an aerosol deposition (AD) spray-coating method based on room temperature deposition can be used. By employing the AD method, we were able to deposit relaxor-ferroelectric $0.65Pb(Mg_{1/3}Nb_{2/3})O_3$–$0.35PbTiO_3$ ceramic thick films on low-cost stainless-steel substrates. The as-deposited films were dense, with ∼97% of the theoretical density. Moreover, the post-deposition annealing at 500 °C did not result in any microstructural changes. Compared to the as-deposited films, the annealed films exhibit improved energy storage and electromechanical properties. The annealed thick films achieve a recoverable energy density of 15.1 $J{\cdot}cm^{-3}$ at an electric field of 1350 $kV{\cdot}cm^{-1}$ and an electric-field cycling stability of 5 million cycles. A piezoelectric response was detected through the entire film thickness by piezoelectric force microscopy. Macroscopic displacement measurements revealed a maximum relative strain of 0.38% at 1000 $kV{\cdot}cm^{-1}$, corresponding to inverse effective piezoelectric coefficient of ∼40 $pm{\cdot}V^{-1}$. In this study, we overcame the integration challenges and demonstrated the multifunctionalization of future ceramic-metal structures, as the deposited thick films on stainless steel exhibit energy storage capability and piezoelectric properties.

1. Introduction

Ceramic perovskite materials are featuring many promising characteristics for use in electronic applications [1]. One of the most promising materials are relaxor-ferroelectrics with a $(100–x)Pb(Mg_{1/3}Nb_{2/3})O_3$ $–xPbTiO_3$ (PMN–100*x*PT) solid solution, as they exhibit versatile dielectric, piezoelectric and relaxor-ferroelectric properties [2]. Of particular interest is the $0.65Pb(Mg_{1/3}Nb_{2/3})O_3$–$0.35PbTiO_3$ (PMN–35PT) material with a composition close to the morphotropic phase boundary due to its high piezoelectric performance in bulk form [3–5]. PMN–35PT possesses all the attributes that are important for electrical energy storage devices in pulsed-power and power-conditioning electronic applications and for electromechanical energy conversion in energy harvesting applications. Both energy storage and energy harvesting are crucial for the efficient use and management of electrical energy, which can ensure the sustainability of integrated electronic systems in the increasingly connected internet of things [6–8].

To miniaturize energy systems, functional components need to be fabricated in the form of thick films. Ceramic thick films with a thickness of a few micrometers enable device miniaturization and are a good compromise between the high volume-specific energy conversion performance offered by ceramic thin films and the large absolute energy conversion offered by conventional bulk ceramics [9]. However, integrating ceramic thick films into everyday devices is challenging. The fabrication of dense and high quality ceramic thick films by conventional thick-film deposition methods, such as screen-printing, tape-casting, or electrophoretic deposition consists of high temperature processes that often exceed 1000 °C [10]. The required high temperature treatment is a limiting factor as it prevents the integration of ceramics with materials that cannot withstand high temperatures, such as polymers and metals.

To overcome the integration barrier, a so-called aerosol deposition (AD) can be used. AD is a room temperature spray-coating method for the deposition of dense, several-μm-thick films on any type of substrate. The deposition mechanism is based on the collision of high-speed particles with the substrate's surface and the densification occurs as a result of high kinetic energies involved [11–13].

Metals and their alloys are frequently considered as substrate materials in the electronics industry because they offer both heat sink and electrode functionality. As such, various metal substrates can expand the range of applications (actuators, sensors, transducers, energy harvesters and energy storage systems) [14, 15]. Metals as substrates offer good electrical conductivity and mechanical stability, which makes them a promising choice also for the field of flexible electronics [16]. Stainless steel (SS) is a versatile metal, durable, and resistant to corrosion and wear. As a low-cost material, it is in everyday use. However, little research has been done on the integration of ferroelectric ceramics on SS. Currently, there are few reports on the deposition of $Pb(Zr,Ti)O_3$-based [14, 17–21], $BaTiO_3$-based [22–24] and $(K,Na)NbO_3$-based [25] thick films on SS. In our previous work, energy storage-efficient PMN–10PT thick films were integrated on SS substrates [26], while this study focuses on a ferroelectric PMN–35PT with a composition close to the morphotropic phase boundary responsible for high piezoelectric response in bulk ceramics [3–5].

In this work, we have deposited ceramic PMN–35PT thick films on SS substrate by employing the AD method, which allows densification of ceramics at room-temperature. We have shown that the integration of ceramic thick films on metals is possible and that such integration enables the multifunctionalization of future ceramic-metal structures, since the deposited PMN–35PT thick films exhibit energy storage capabilities and piezoelectric properties.

2. Materials and methods

PbO (99.9%, Aldrich), MgO (99.95%, Alfa Aesar), TiO_2 (99.8%, Alfa Aesar) and Nb_2O_5 (99.9%, Aldrich) were used for the synthesis of PMN–35PT ceramic powder. Two sets of oxide mixtures corresponding to the stoichiometry of $Pb(Mg_{1/3}Nb_{2/3})O_3$ and $PbTiO_3$ were separately homogenized for 2 h in a planetary ball mill (PM 400, Retsch, Germany) at 200 min^{-1}, in isopropanol, using milling balls made of yttria-stabilized zirconia (YSZ) with diameter of 3 mm. After that, the powder mixture corresponding to the stoichiometry of $PbTiO_3$ was calcined at 750 °C for 2 h as previously suggested by Dragomir *et al* [27] and additionally milled for 2 h in a planetary ball mill (PM 400, Retsch, Germany) under the same conditions. Eventually, both powder mixtures were mixed together and homogenized for 2 h with a stoichiometry of $0.65Pb(Mg_{1/3}Nb_{2/3})O_3$–$0.35PbTiO_3$. The homogenization was carried out in a planetary ball mill (PM 400, Retsch, Germany) under the same conditions as before. This mixture was reacted for 24 h by mechanochemical-activation-assisted synthesis, using the same planetary ball mill, but at 300 min^{-1} in a tungsten-carbide milling vial with a volume of 250 cm^3, filled with 10 tungsten-carbide milling balls with a diameter of 20 mm. After synthesis, the powder was milled for 2 h, heated in a furnace at 900 °C for 1 h (with heating and cooling rates of 5 $K{\cdot}min^{-1}$), and finally milled for 0.5 h. The milling processes were carried out in a planetary ball mill (PM 400, Retsch, Germany) at 200 min^{-1}, in isopropanol, using milling balls made of yttria-stabilized zirconia (YSZ) with diameter of 3 mm.

Prior to AD of the PMN–35PT powder on the substrate, the powder was sieved through an 80 μm mesh and vacuum dried for 12 h at 100 °C and 10 mbar. The substrate used was a commercial SS No. 304 (American Iron and Steel Institute) with a bright, polished surface A480: No. 8 (American Society for Testing and Materials) with dimensions 15 mm × 15 mm × 0.8 mm. The AD equipment was provided by InVerTec, Germany and the scheme of the set-up is represented elsewhere [28]. The process parameters during AD are listed in (supplementary material S1 available online at stacks.iop.org/JPEnergy/6/024004/mmedia). After AD, the samples were cleaned with ethanol and annealed at 500 °C for 1 h with heating and cooling rates of 2 $K{\cdot}min^{-1}$. From now on, the samples will be referred to as 'as-deposited' and 'annealed'.

The x-ray diffraction (XRD) analysis was performed with a high-resolution diffractometer (X'Pert PRO, PANalytical, Netherlands) using Cu–Kα_1 radiation. Diffraction patterns were recorded in the Bragg–Brentano geometry using a 100-channel X'Celerator detector in a 2θ range of 10°–120° with a step of

0.017° and an integration time of 100 s per step. For the Rietveld refinement, the Topas R package (version 2.1, Bruker AXS GmbH, Germany) was employed as described elsewhere [26]. According to the literature, a tetragonal (*P4mm*) and a monoclinic (*Pm*) crystal structure co-exist in the PMN–35PT solid solution [2, 3]. However, to calculate the crystallite size and microstrain of the film only the *P4mm* structure was selected. To fit the SS reflections originating from the substrate a cubic (*Fm*-3 *m*) crystal structure was used. The fundamental parameters approach (FPA) was used to fit the line-profile of the samples [29]. The FPA uses the geometrical properties of the diffraction experiment to build up the instrumental linewidth from first principles. Therefore, the FPA allows determination of the sample-dependent line-broadening contributions to the peak profile, which are dominated by microstrain and crystallite size broadening [30]. The effects of the microstructure were modeled using the Double-Voigt approach [31]. The volume-weighted mean crystallite size was calculated based on the integral breath method integrated in the Topas software. The calculated peak profiles and the agreement factors of the Rietveld refinement are listed in supplementary material S2.

Scanning electron microscopy (SEM) analyses of thick films' surfaces and cross-sections were performed with a field-emission scanning electron microscope (FE-SEM, JSM-7600F, JEOL, Japan). For the cross-sectional analyses, the samples were cut, mounted in epoxy resin, ground and fine-polished using a colloidal silica suspension. Prior to the SEM analyses, the samples were coated with a 3 nm thick carbon layer using a Precision Etching and Coating System (PECS 682, Gatan, USA). The thickness and the porosity of thick films were evaluated from SEM cross-sectional images. For the estimation of porosity, the Image Tool software (UTHSCSA Image Tool Version 3.00. 2002 [32]) was used.

Piezoelectric force microscopy (PFM) was performed on two types of thick film samples; first, on the polished surface and second, on the polished cross-section of the thick films. The samples were polished as described above. An atomic force microscope (AFM; MFP-3D, Asylum Research, USA) and Ti/Ir coated silicon tips (Asyelec_01_R2, Oxford Instruments, Germany) were used for the analysis. To examine the polished surface, the electric voltage of 25 V and a frequency of ∼350 kHz were applied between a conductive AFM tip and the bottom electrode of the films. To examine the samples in cross-section, electric voltage of 30 V and a frequency of ∼350 kHz were applied to the thick film/epoxy resin composite in the virtual ground regime as previously described in [33, 34]. After PFM scans, the PFM phase hysteresis loops were measured on the polished surface samples in the switching spectroscopy off-electric-field mode with the pulsed DC step signal and the superimposed AC drive signal, as described in [35]. The waveform parameters were as follows: The sequence of rising steps of the DC electric field was driven at 20 Hz and a maximum amplitude of 100 V; the frequency of the triangular envelope was 0.99 Hz; a superimposed sinusoidal AC signal with an amplitude of 25 V and a frequency of ∼350 kHz was used. Three cycles were measured in an off-electric-field mode.

For the electrical and electro-mechanical measurements, the top Au electrodes with a diameter of 1.5 mm were deposited by RF-magnetron sputtering. Measurements of dielectric permittivity and dielectric losses versus temperature are given in supplementary material S3. The unipolar polarization–electric field (*P*–*E*) hysteresis loops and bipolar strain–electric field (*S*–*E*) hysteresis loops of the films were measured at room temperature using an aixACCT TF analyzer 2000 (aixACCT Systems GmbH, Germany) equipped with a single beam laser interferometer. The applied electric field had a single sinusoidal waveform with a frequency of 100 Hz. In the electric-field fatigue cycling experiment the *P*–*E* loops were measured at an electric field of 500 kV·cm^{-1}. The direct piezoelectric coefficient ($d_{33\,eff}$) measurements of annealed thick films were performed using a Berlincourt piezometer (Take Control PM10, UK). Prior to the measurements, the samples were polarized by applying a DC electric field of 200 kV·cm^{-1} at 160 °C for 15 min and then field-cooled to 30 °C.

3. Results

The structural and microstructural properties of as-deposited and annealed PMN–35PT thick films were investigated by XRD and SEM. The XRD patterns of the thick films and the PMN–35PT starting powder are shown in figures 1(a) and (b). None of the secondary phases were detected. The thick film samples exhibit additional minor SS reflections originating from the surrounding substrate. The perovskite reflections showed no significant peak shift after film deposition or after further annealing of the film. However, compared to the PMN–35PT powder, the as-deposited thick films exhibit a remarkable peak broadening. This broadening is due to reduced crystallite size and/or microstrain, and is typically observed in aerosol-deposited thick films, as the AD process involves cracking and fragmentation of colliding powder particles. Importantly, the broadening decreases slightly after annealing of thick films, indicating stress relaxation, which can occur even at moderate temperatures such as 500 °C [23, 36, 37].

The XRD patterns were examined in detail using Rietveld refinement, which quantitatively evaluates the crystallite size and microstrain of the samples (figures 1(c) and (d)). The calculated crystallite size of the PMN–35PT powder is 146 nm ± 3 nm and the microstrain is $8.4 \times 10^{-4} \pm 0.3 \times 10^{-4}$. After the AD process

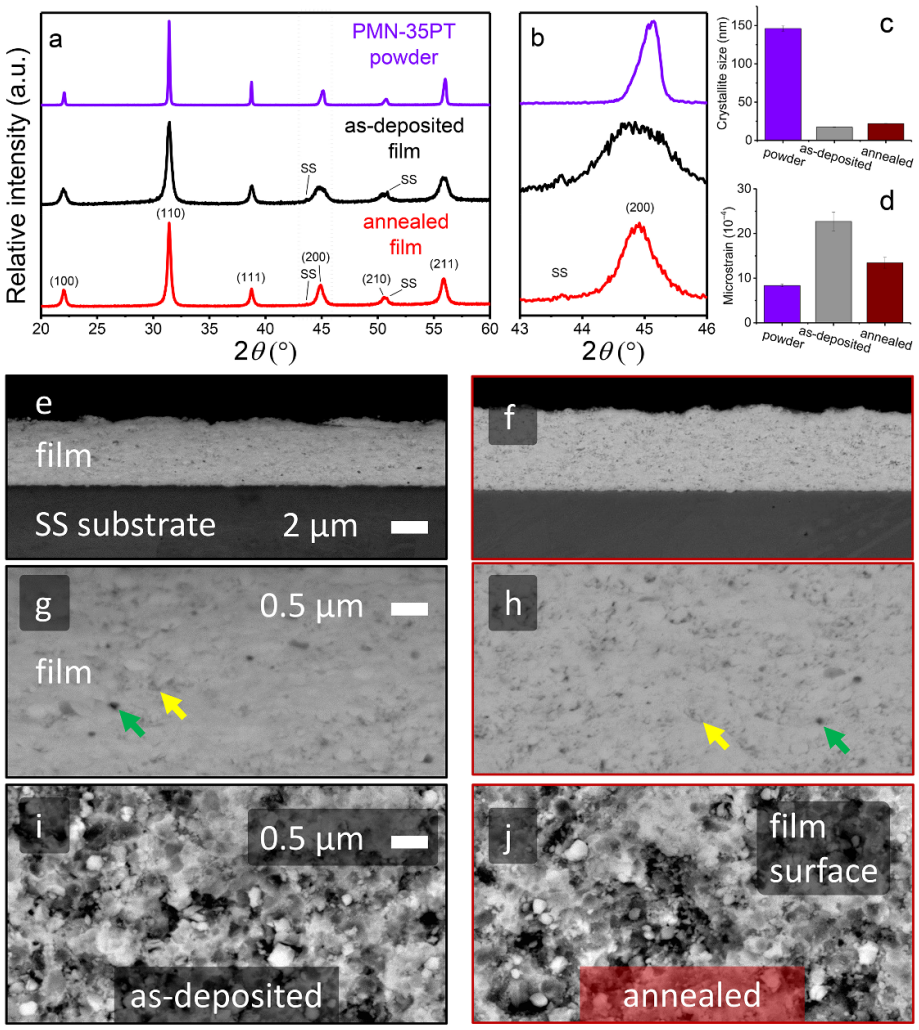

Figure 1. (a) XRD patterns in the 2θ range of 20°–60° for PMN–35PT powder, as-deposited and annealed thick films; (b) enlarged view of (200) reflection. Diffraction peaks corresponding to perovskite phase are indexed according to the cubic notation (JCPDS 81–0861). The corresponding (c) crystallite size and (d) microstrain evaluated using Rietveld refinement. SEM micrographs of as-deposited (e), (g), (i) and annealed (f), (h), (j) films in cross-section (e)–(h) and surface (i), (j) views. Green and yellow arrows mark pores several tens of nm in size and smaller pores in the nm-range, respectively.

the crystallite size of as-deposited thick films decreases to 17.2 nm ± 0.3 nm and the microstrain increases to $22.7 \times 10^{-4} \pm 2.1 \times 10^{-4}$. These results indicate a remarkable (8-fold) decrease in crystallite size that occurs during the high-energy particle collisions in the AD process. According to Exner *et al* [38] significant crystallite size reduction is a prerequisite for successful film consolidation. A crystallite size reduction is indicating the extent of converted kinetic energy into fracture energy, forming new surfaces that allow the particles to rebond and consolidate into a film [38]. Further annealing of the thick films has a minor effect on the crystallite size (21.9 nm ± 0.3 nm), but much more on the microstrain, which decreases significantly by 41% (down to $13.4 \times 10^{-4} \pm 1.2 \times 10^{-4}$).

The as-deposited and annealed thick films were analyzed by SEM in cross-sectional (figures 1(e)–(h)) and surface view (figures 1(i) and (j)). Both samples exhibit similar microstructure, despite the difference in the annealing process. Figures 1(e) and (f) reveals around 4 μm thick films firmly attached to SS substrates. The film-substrate interface does not show any damaging effects or any signs of chemical reaction between the film and the substrate. The polished cross-sections (figures 1(g) and (h)) show a crack free microstructure with a density of 97% ± 1%. The remaining porosity of 3% ± 1% is similar in as-deposited and annealed films and consists of isolated pores of several tens of nm in size (green arrows) and smaller pores in the nm-range (yellow arrows). The SEM micrographs of films' surfaces confirm (figures 1(i) and (j)) a high film density.

Figure 2(a) shows the unipolar *P*–*E* hysteresis loops of the as-deposited and annealed films. The as-deposited films exhibit linear dielectric-like behavior at low electric field (300 kV·cm^{-1}), while a more lossy, round-like behavior is observed at high electric fields (1350 kV·cm^{-1}). The annealing of the films leads

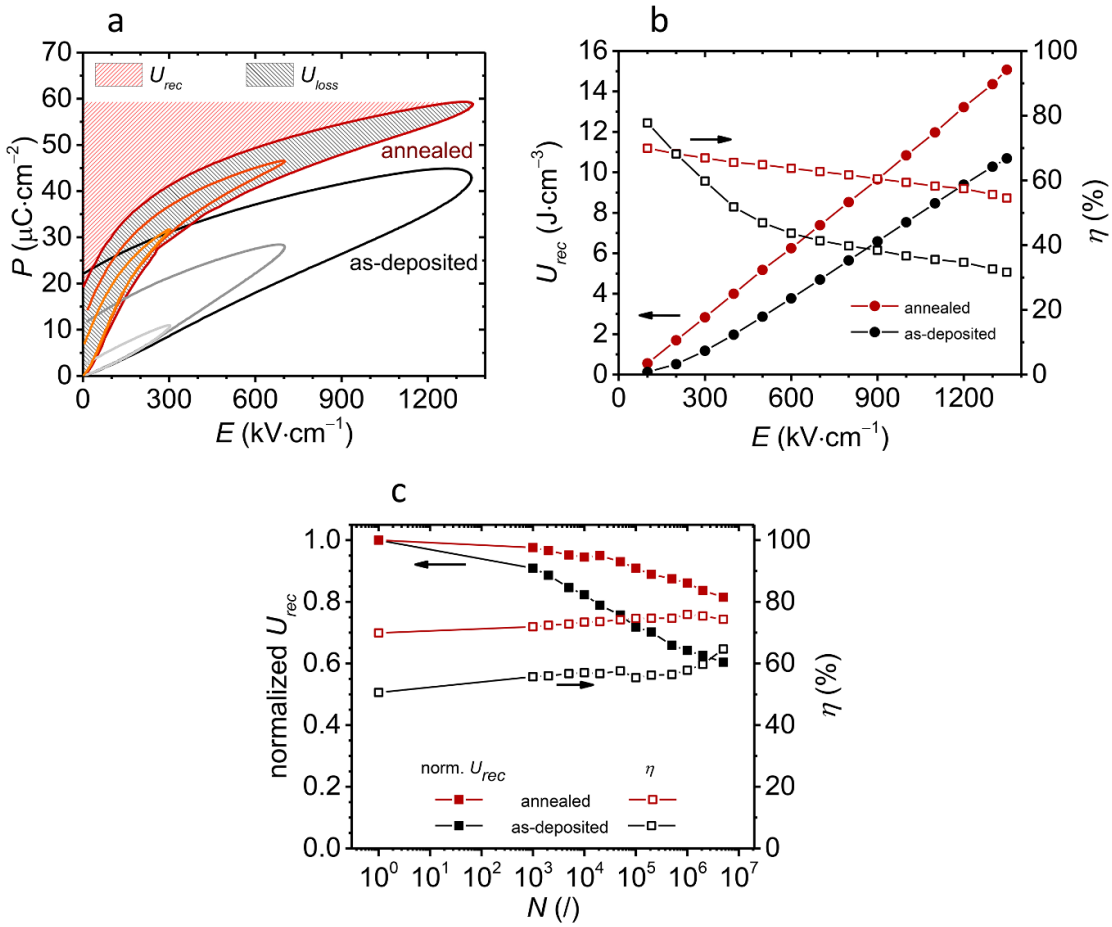

Figure 2. (a) Unipolar *P–E* hysteresis loops of as-deposited (grey to black lines) and annealed (orange to red lines) thick films. *P–E* loops measured up to 300, 700 and 1350 kV·cm^{-1} are shown in light to dark shades. U_{rec} and U_{loss} of the annealed film are represented by the red and grey patterned areas, respectively. (b) The electric-field dependence of U_{rec} and η for the as-deposited and annealed thick films. (c) The electric-field cycling dependence of a normalized U_{rec} and η for the as-deposited and annealed thick films at 500 kV·cm^{-1}. The lines between the values are only a guide for the eye.

to a relaxor-ferroelectric character of the *P–E* loop. Moreover, the shape of the *P–E* loop remains similar with decreasing frequency (supplementary material S4). As we have seen in the SEM analysis (figures 1(e)–(j)), the microstructure is preserved after annealing the films. Therefore, one of the possible reasons for the changes in *P–E* behavior after annealing is related to stress relaxation, as previously shown for PMN–10PT thick films on SS [26]. Dielectric breakdown strength (DBS) was evaluated using Weibull analysis (supplementary material S5). The determined DBS is high, i.e. 1334 and 1351 kV·cm^{-1} for as-deposited and annealed thick films, respectively. Compared to the as-deposited films, the annealed films exhibit lower hysteresis losses and higher polarization. At 1350 kV·cm^{-1} the polarization of as-deposited and annealed films reaches 43 and 59 μC·cm^{-2}, respectively. The high electric polarization and DBS indicate possibility of achieving excellent energy storage properties.

The energy storage performance of the PMN–35PT thick films was evaluated by calculating the recoverable energy density (U_{rec}) and energy storage efficiency (η). The U_{rec} represents the energy that is available in the discharge cycle and is therefore calculated by integrating the area between the discharge curve and the polarization axis (red patterned area in figure 2(a)). The charge–discharge cycle generates also hysteresis or polarization losses (U_{loss}), which are calculated by integrating the area between the charge and discharge curves (grey patterned area in figure 2(a)). The η is determined from the ratio between the recovered and stored energy: $\eta = U_{rec}/(U_{rec} + U_{loss})$ and therefore, highly efficient energy storage capacitors, should have low U_{loss} [9].

In as-deposited thick films, the U_{rec} increases linearly with the electric field and reaches 10.7 J·cm^{-3} at 1350 kV·cm^{-1}, which is already high for AD thick films prepared at room temperature (figure 2(b)). These values are almost an order of magnitude higher than U_{rec} of various bulk ceramics, reaching between 1 and 5 J·cm^{-3} [39–41]. However, the η-value decreases with the electric field. It decreases from 78% at 100 kV·cm^{-1} to 32% at 1350 kV·cm^{-1} ($\Delta\eta = 46\%$). The annealed thick films have improved energy storage

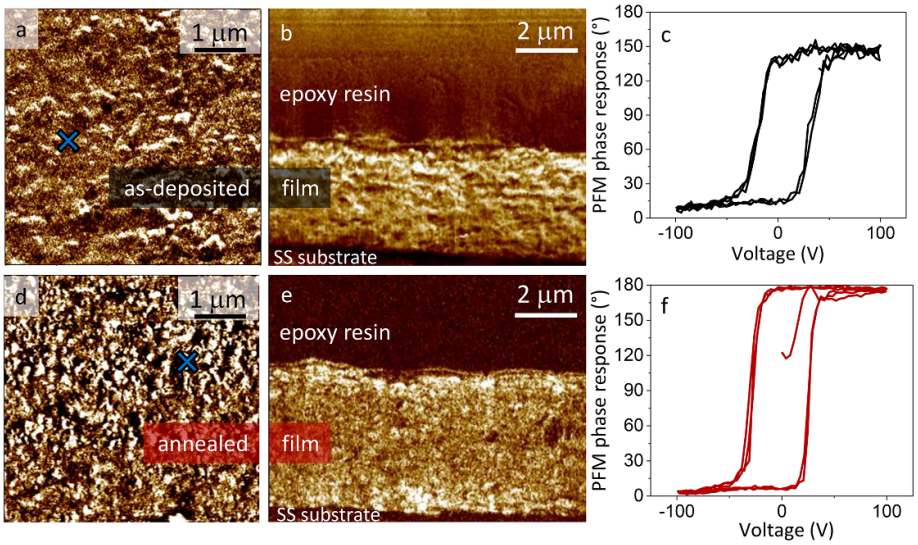

Figure 3. PFM out-of-plane amplitude images of (a), (d) surface and (b), (e) cross-section views for (a), (b) as-deposited and (d), (e) annealed PMN–35PT thick films on SS. Switching spectroscopy experiment; the local hysteresis loops of the PFM out-of-plane (c), (f) phase measurements obtained at the point marked by blue crosses in panels (a), (d).

properties. The U_{rec} value reaches 15.1 J·cm^{-3} at 1350 kV·cm^{-1}, which corresponds to an increase of 41% compared to the as-deposited films (figure 2(b)). Overall, the annealed PMN–35PT films on low-cost SS substrate exhibit U_{rec} values comparable to other AD thick films on conventional, more expensive platinized silicon substrates (Pt/Ti/SiO$_2$/Si) [42–46]. The η of the annealed films is more stable with increasing electric field compared to the as-deposited films. It reaches 70% at 100 kV·cm^{-1} and 55% at 1350 kV·cm^{-1} ($\Delta\eta = 15\%$).

The properties during fatigue cycling under electric field are shown in figure 2(c). Both the deposited and annealed films withstood a large number of electric field cycles, i.e. 5×10^6. During the fatigue test, the η-value of both samples is stable while the U_{rec} value of the deposited and annealed films decreases to ~0.6 and ~0.8 of the initial U_{rec} value after 5 million cycles, respectively.

The local electromechanical response of the as-deposited (figures 3(a)–(c)) and annealed films (figures 3(d)–(f)) was investigated by PFM. The PFM out-of-plane amplitude images of the polished film surfaces (figures 3(a) and (d)) show a piezoelectric response associated with the fine-grained microstructure of as-deposited and annealed films (figure 1). It is evident that the annealed thick film exhibits more areas with enhanced piezoelectric response (bright regions) in comparison to the as-deposited film. The cross-sectional PFM out-of-plane amplitude images (figures 3(b) and (e)) confirm that both films are piezoelectrically active throughout their thickness, while the SS substrate or the encapsulating epoxy resin above the film does not show any piezoelectric response (dark areas). Furthermore, PFM switching spectroscopy was performed on the polished film surfaces. The analysis shows a local hysteresis loop of the PFM phase (figures 3(c) and (f)), which is evidence that the ferroelectric domains in the as-deposited and annealed films can be effectively switched.

Macroscopic displacement measurements were performed on the as-deposited and annealed films. The measured relative longitudinal strain with the applied electric field (*S–E*) is shown in figure 4(a). The *S–E* loops of both samples are symmetrical i.e. without any imprint and their shape is typical of relaxor-ferroelectric materials. The strain response is much larger for the annealed films. The as-deposited and annealed films reach a maximum strain of 0.25% and 0.38%, respectively, at 1000 kV·cm^{-1}. Figure 4(b) shows the *S/E* coefficient (or inverse effective piezoelectric coefficient, $d^*_{33\,eff}$) evaluated from the slope of the *S–E* loops by linear regression. In as-deposited films, $d^*_{33\,eff}$ gradually increases with the electric field, reaching 25 pm·V^{-1} at 1000 kV·cm^{-1}, while in annealed films, $d^*_{33\,eff}$ reaches a constant value of 41 pm·V^{-1} from 650 to 1000 kV·cm^{-1}. A small difference between the $d^{*,+}_{33\,eff}$ and $d^{*,-}_{33\,eff}$ coefficients (determined from the right and left sides of the (*S–E*) hysteresis loops, respectively) confirms a symmetrical electromechanical behavior. The displacement measurements were also performed with a double beam laser interferometer (DBLI, supplementary material S6) and the determined $d^*_{33\,eff}$ is similar, indicating that there is no displacement due to substrate bending during the measurements. Additional measurements of the direct effective piezoelectric coefficient ($d_{33\,eff}$) were performed after the DC poling at elevated temperatures. The $d_{33\,eff}$ of the annealed films reaches ~25 pC·N^{-1}, which is close to the measured $d^*_{33\,eff}$ at low electric field. However, the

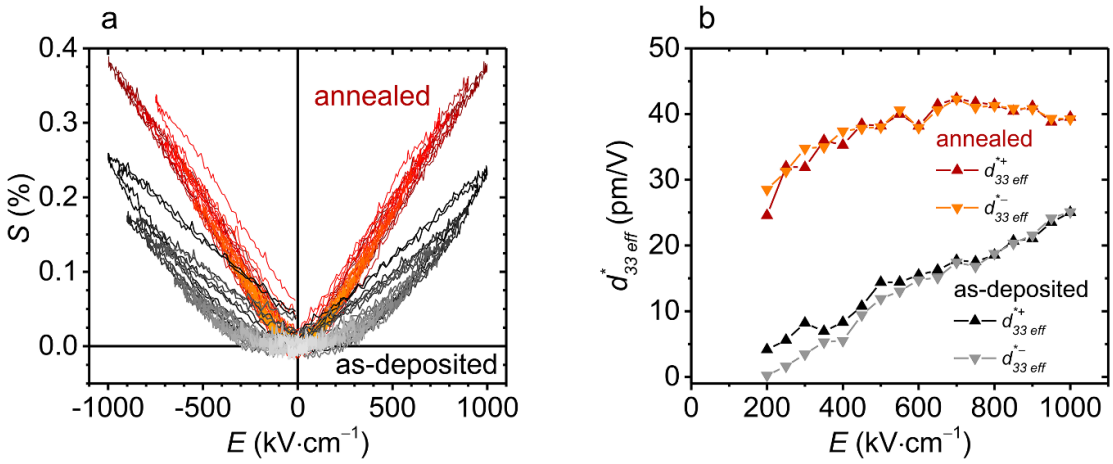

Figure 4. (a) Strain vs. electric field (*S*–*E*) hysteresis loops of as-deposited (grey-black) and annealed (orange-red) thick films. (b) The $d^*_{33\,eff}$ vs. *E* of as-deposited (grey and black) and annealed (orange and red) thick films. The $d^{*,+}_{33\,eff}$ and $d^{*,-}_{33\,eff}$ coefficients are evaluated with a linear regression of the positive and negative *E* (i.e. the right and left sides of the *S*–*E* hysteresis loops), respectively.

piezoelectric coefficient of PMN–35PT AD thick films is lower than that of PMN–35PT ceramics (typically above 525 pC·N^{-1}) [4, 47–49] and screen-printed thick films on platinized Al_2O_3 substrates (typically between 130 and 170 pC·N^{-1}) [50–52]. This can be attributed to several factors: first, the film-substrate clamping effect in thick films [51, 53] and second, the much smaller grain size in AD thick films [47] in comparison to screen-printed films or bulk ceramics, due to the low processing temperature.

4. Summary and conclusions

By employing the AD method, which enables the fabrication of dense ceramic layers at room temperature, we deposited ceramic PMN–35PT thick films on low-cost stainless-steel substrates. The deposited 4 μm thick films exhibit high density, namely 97% of the theoretical density, with pores in the range of a few to tens of nm. Post-deposition annealing at moderate temperatures of 500 °C does not lead to any microstructural changes, but reduces the microstrain by 41%.

The annealed thick films exhibit high polarization (59 μC·cm^{-2}) and high DBS (~1350 kV·cm^{-1}), leading to promising energy storage performance. The U_{rec} value of the annealed PMN–35PT films on the low-cost SS reaches 15.1 J·cm^{-3} at 1350 kV·cm^{-1}, which is similar to other AD thick films on conventional, more expensive platinized silicon substrates (Pt/Ti/SiO_2/Si). Moreover, both the as-deposited and annealed films withstand a large number of electric field cycles, namely 5×10^6. The electromechanical response of the thick films was investigated in cross-section using the PFM technique. The as-deposited and annealed films are piezoelectric/ferroelectric over the entire film thickness. The macroscopic electromechanical measurements of the as-deposited and annealed films revealed a longitudinal strain of 0.25% and 0.38% at 1000 kV·cm^{-1}, corresponding to $d^*_{33\,eff}$ of 25 and 41 pm·V^{-1}, respectively.

In summary, we have shown that the integration of PMN–35PT thick films on SS is possible and that such integration enables the multifunctionalization of future ceramic-metal structures, since the deposited PMN–35PT thick films exhibit energy storage capability and piezoelectric properties. The multifunctional properties are already observed in films deposited at room temperature. However, they are further enhanced by post-deposition annealing at moderate temperatures of 500 °C.

Data availability statement

The data generated and/or analyzed during the current study are not publicly available for legal/ethical reasons but are available from the corresponding author on reasonable request.

Acknowledgments

H U and M S acknowledge the Slovenian Research Agency (research project J2-3058, young researcher project PR-08977, bilateral projects BI-FR/21-22-PROTEUS-004 and BI-DE/20-21-012 and research core

funding P2-0105) and JSI Director's fund 2017-ULTRACOOL. They thank R Elshuraf (Erasmus+ program), V Fišinger and J Cilenšek for help in the laboratory.

Conflict of interest

The authors declare that they have no known competing financial interests or personal relationships that could have appeared to influence the work reported in this paper.

ORCID iDs

Matej Sadl https://orcid.org/0000-0003-1497-5610
Kevin Nadaud https://orcid.org/0000-0002-2969-1453
Micka Bah https://orcid.org/0000-0001-6636-2854
Udo Eckstein https://orcid.org/0000-0001-9546-8463
Neamul H Khansur https://orcid.org/0000-0001-8769-3329
Hana Ursic https://orcid.org/0000-0003-4525-404X

References

[1] Uchino K 2015 Glory of piezoelectric perovskites *Sci. Technol. Adv. Mater.* **16** 46001
[2] Otoničar M *et al* 2020 Connecting the multiscale structure with macroscopic response of relaxor ferroelectrics *Adv. Funct. Mater.* **30** 1–12
[3] Uršič H, Tellier J, Hrovat M, Holc J, Drnovšek S, Bobnar V, Alguero M and Kosec M 2011 The effect of poling on the properties of 0.65Pb($Mg_{1/3}Nb_{2/3}$)O_3–0.35$PbTiO_3$ ceramics *Jpn. J. Appl. Phys.* **50** 035801
[4] Kelly J, Leonard M, Tantigate C and Safari A 1997 Effect of composition on the electromechanical properties of (1-x)Pb($Mg_{1/3}Nb_{2/3}$)O_3 −x$PbTiO_3$ ceramics *J. Am. Ceram. Soc.* **80** 957–64
[5] Algueró M, Alemany C, Pardo L and Pham-Thi M 2005 Piezoelectric resonances, linear coefficients and losses of morphotropic phase boundary Pb($Mg_{1/3}Nb_{2/3}$)O_3–$PbTiO_3$ ceramics *J. Am. Ceram. Soc.* **88** 2780–7
[6] Narita F and Fox M 2018 A review on piezoelectric, magnetostrictive, and magnetoelectric materials and device technologies for energy harvesting applications *Adv. Eng. Mater.* **20** 1700743
[7] Sun H, Yin M, Wei W, Li J, Wang H and Jin X 2018 MEMS based energy harvesting for the internet of things: a survey *Microsyst. Technol.* **24** 2853–69
[8] Hooper T E, Roscow J I, Mathieson A, Khanbareh H, Goetzee-Barral A J and Bell A J 2021 High voltage coefficient piezoelectric materials and their applications *J. Eur. Ceram. Soc.* **41** 6115–29
[9] Palneedi H, Peddigari M, Hwang G T, Jeong D Y and Ryu J 2018 High-performance dielectric ceramic films for energy storage capacitors: progress and outlook *Adv. Funct. Mater.* **28** 1803665
[10] Kosec M, Kuscer D and Holc J 2011 Processing of ferroelectric ceramic thick films *Multifunctional Polycrystalline Ferroelectric Materials* vol 140 ed Pardo L and Ricote J (Dordrecht: Springer) (https://doi.org/10.1007/978-90-481-2875-4_2)
[11] Akedo J 2008 Room temperature impact consolidation (RTIC) of fine ceramic powder by aerosol deposition method and applications to microdevices *J. Therm. Spray Technol.* **17** 181–98
[12] Hanft D, Exner J, Schubert M, Stöcker T, Fuierer P and Moos R 2015 An overview of the aerosol deposition method: process fundamentals and new trends in materials applications *J. Ceram. Sci. Technol.* **6** 147–81
[13] Saunders R, Johnson S D, Schwer D, Patterson E A, Ryou H and Gorzkowski E P 2021 A self-consistent scheme for understanding particle impact and adhesion in the aerosol deposition process *J. Therm. Spray Technol.* **30** 523–41
[14] Baba S and Akedo J 2005 Damage-free and short annealing of Pb(Zr,Ti)O_3 thick films directly deposited on stainless steel sheet by aerosol deposition with CO_2 laser radiation *J. Am. Ceram. Soc.* **88** 1407–10
[15] Zou Q, Ruda H E, Yacobi B G, Saegusa K and Farrell M 2000 Dielectric properties of lead zirconate titanate thin films deposited on metal foils *Appl. Phys. Lett.* **77** 1038–40
[16] Cheng I-C and Wagner S 2009 Overview of flexible electronics technology *Flexible Electronics: Materials and Applications* vol 11 ed Wong W S and Salleo A (Boston, MA: Springer) pp 1–28
[17] Akedo J and Lebedev M 2002 Effects of annealing and poling conditions on piezoelectric properties of Pb($Zr_{0.52}$,$Ti_{0.48}$)O_3 thick films formed by aerosol deposition method *J. Cryst. Growth* **235** 415–20
[18] Akedo J, Lebedev M, Sato H and Park J 2005 High-speed optical microscanner driven with resonation of lam waves using Pb(Zr,Ti)O_3 thick films formed by aerosol deposition *Jpn. J. Appl. Phys.* **44** 7072–7
[19] Lin S-C and Wu W-J 2013 Fabrication of PZT MEMS energy harvester based on silicon and stainless-steel substrates utilizing an aerosol deposition method *J. Micromech. Microeng.* **23** 125028
[20] Kawakami Y, Yoshikawa H, Komagata K and Akedo J 2005 Powder preparation for 0.5 Pb($Ni_{1/3}Nb_{2/3}$)O_3-0.15 $PbZrO_3$-0.35$PbTiO_3$ thick films by the aerosol deposition method *J. Cryst. Growth* **275** 1295–300
[21] Chen C-T, Lin S-C, Trstenjak U, Spreitzer M and Wu W-J 2021 Comparison of metal-based PZT and PMN–PT energy harvesters fabricated by aerosol deposition method *Sensors* **21** 4747
[22] Kawakami Y, Watanabe M, Arai K-I and Sugimoto S 2016 Effects of substrate materials on piezoelectric properties of $BaTiO_3$ thick films deposited by aerosol deposition *Jpn. J. Appl. Phys.* **55** 10TA10
[23] Khansur N H, Eckstein U, Benker L, Deisinger U, Merle B and Webber K G 2018 Room temperature deposition of functional ceramic films on low-cost metal substrate *Ceram. Int.* **44** 16295–301
[24] Khansur N H, Eckstein U, Sadl M, Ursic H and Webber K G 2020 Fabrication of porous thick films using room-temperature aerosol deposition *J. Am. Ceram. Soc.* **103** 43–47
[25] Oh S-W, Akedo J, Park J-H and Kawakami Y 2006 Fabrication and evaluation of lead-free piezoelectric ceramic LF4 thick film deposited by aerosol deposition method *Jpn. J. Appl. Phys.* **45** 7465–70

[26] Sadl M et al 2021 Energy-storage-efficient 0.9Pb($Mg_{1/3}Nb_{2/3}$)O_3–0.1$PbTiO_3$ thick films integrated directly onto stainless steel *Acta Mater.* **221** 117403
[27] Dragomir M, Otoničar M, Vrabelj M, Fulanović L, Drnovšek S, Rojac T and Malič B 2019 Seeding effects on the mechanochemical synthesis of 0.9Pb($Mg_{1/3}Nb_{2/3}$)O_3–0.1$PbTiO_3$ *J. Eur. Ceram. Soc.* **39** 1837–45
[28] Sadl M, Tomc U, Prah U and Ursic H 2019 Protective alumina coatings prepared by aerosol deposition on magnetocaloric gadolinium elements *Inf. MIDEM* **49** 177–82
[29] Cheary R W and Coelho A 1992 A fundamental parameters approach to x-ray line-profile fitting *J. Appl. Crystallogr.* **25** 109–21
[30] Klug H P and Alexander L E 1974 *X-ray Diffraction Procedures: For Polycrystalline and Amorphous Materials* 2nd edn (New York: Wiley)
[31] Balzar D *et al* 2004 Size-strain line-broadening analysis of the ceria round-robin sample *J. Appl. Crystallogr.* **37** 911–24
[32] Wilcox D, Dove B, McDavid B and Greer D 2002 UTHSCSA image tool for windows Version 3.0. (San Antonio: University of Texas Health Science Center)
[33] Kržmanc M M, Uršič H, Meden A, Korošec R C and Suvorov D 2018 $Ba_{1-x}Sr_xTiO_3$ plates: synthesis through topochemical conversion, piezoelectric and ferroelectric characteristics *Ceram. Int.* **44** 21406–14
[34] Kržmanc M M, Jančar B, Uršič H, Tramšek M and Suvorov D 2017 Tailoring the shape, size, crystal structure, and preferential growth orientation of $BaTiO_3$ plates synthesized through a topochemical conversion process *Cryst. Growth Des.* **17** 3210–20
[35] Uršič H and Prah U 2019 Investigations of ferroelectric polycrystalline bulks and thick films using piezoresponse force microscopy *Proc. R. Soc.* A **475** 20180782
[36] Khansur N H, Eckstein U, Riess K, Martin A, Drnec J, Deisinger U and Webber K G 2018 Synchrotron x-ray microdiffraction study of residual stresses in $BaTiO_3$ films deposited at room temperature by aerosol deposition *Scr. Mater.* **157** 86–89
[37] Exner J, Nazarenus T, Hanft D, Kita J and Moos R 2020 What happens during thermal post-treatment of powder aerosol deposited functional ceramic films? Explanations based on an experiment-enhanced literature survey *Adv. Mater.* **32** 1908104
[38] Exner J, Schubert M, Hanft D, Kita J and Moos R 2019 How to treat powders for the room temperature aerosol deposition method to avoid porous, low strength ceramic films *J. Eur. Ceram. Soc.* **39** 592–600
[39] Peddigari M, Palneedi H, Hwang G-T and Ryu J 2019 Linear and nonlinear dielectric ceramics for high-power energy storage capacitor applications *J. Korean Ceram. Soc.* **56** 1–23
[40] Zhao P, Wang S, Tang H, Jian X, Zhao X, Yao Y, Tao T, Liang B and Lu S-G 2021 Superior energy storage density and giant negative electrocaloric effects in ($Pb_{0.98}La_{0.02}$)(Zr, Sn)O_3 antiferroelectric ceramics *Scr. Mater.* **200** 113920
[41] Kumar R and Singh S 2018 Giant electrocaloric and energy storage performance of [($K_{0.5}Na_{0.5}$)NbO_3](1−x)-[$LiSbO_3$] x nanocrystalline ceramics *Sci. Rep.* **8** 1–9
[42] Peddigari M, Palneedi H, Hwang G T, Lim K W, Kim G Y, Jeong D Y and Ryu J 2018 Boosting the recoverable energy density of lead-free ferroelectric ceramic thick films through artificially induced quasi-relaxor behavior *ACS Appl. Mater. Interfaces* **10** 20720–7
[43] Jung H-B, Lim J-H, Peddigari M, Ryu J, Choi D H and Jeong D-Y 2020 Enhancement of energy storage and thermal stability of relaxor $Pb_{0.92}La_{0.08}Zr_{0.52}Ti_{0.48}O_3$-Bi($Zn_{0.66}Nb_{0.33}$)$O_3$ thick films through aerosol deposition *J. Eur. Ceram. Soc.* **40** 63–70
[44] Kumar A, Kim S H, Thakre A, Lee G, Chae Y G and Ryu J 2020 Increased energy-storage density and superior electric field and thermally stable energy efficiency of aerosol-deposited relaxor ($Pb_{0.89}La_{0.11}$)($Zr_{0.70}Ti_{0.30}$)O_3 Films *J. Therm. Spray Technol.* **30** 591–602
[45] Park C-K, Lee S H, Lim J-H, Ryu J, Choi D H and Jeong D-Y 2018 Nano-size grains and high density of 65PMN-35PT thick film for high energy storage capacitor *Ceram. Int.* **44** 20111–4
[46] Kumar A, Lee G, Chae Y G, Thakre A, Choi H S, Nam G H and Ryu J 2021 Induced slim ferroelectric hysteresis loops and enhanced energy-storage properties of Mn-doped ($Pb_{0.93}La_{0.07}$)($Zr_{0.82}Ti_{0.18}$)O_3 anti-ferroelectric thick films by aerosol deposition *Ceram. Int.* **47** 31590–6
[47] Algueró M, Ricote J, Jiménez R, Ramos P, Carreaud J, Dkhil B, Kiat J M, Holc J and Kosec M 2007 Size effect in morphotropic phase boundary Pb($Mg_{1/3}Nb_{2/3}$)O_3–$PbTiO_3$ *Appl. Phys. Lett.* **91** 112905
[48] Koo T Y and Cheong S-W 2002 Dielectric and piezoelectric enhancement due to 90° domain rotation in the tetragonal phase of Pb($Mg_{1/3}Nb_{2/3}$)O_3-$PbTiO_3$ *Appl. Phys. Lett.* **80** 4205–7
[49] Xia Z, Wang L, Yan W, Li Q and Zhang Y 2007 Comparative investigation of structure and dielectric properties of Pb($Mg_{1/3}Nb_{2/3}$)O_3–$PbTiO_3$ (65/35) and 10% $PbZrO_3$-doped Pb($Mg_{1/3}Nb_{2/3}$)O_3–$PbTiO_3$ (65/35) ceramics prepared by a modified precursor method *Mater. Res. Bull.* **42** 1715–22
[50] Kuščer D, Skalar M, Holc J and Kosec M 2009 Processing and properties of 0.65Pb($Mg_{1/3}Nb_{2/3}$)O_3–0.35$PbTiO_3$ thick films *J. Eur. Ceram. Soc.* **29** 105–13
[51] Uršič H, Zarnik M S, Tellier J, Hrovat M, Holc J and Kosec M 2011 The influence of thermal stresses on the phase composition of 0.65Pb($Mg_{1/3}Nb_{2/3}$)O_3–0.35$PbTiO_3$ thick films *J. Appl. Phys.* **109** 014101
[52] Kosec M, Holc J, Kuscer D and Drnovšek S 2007 Pb($Mg_{1/3}Nb_{2/3}$)O_3–$PbTiO_3$ thick films from mechanochemically synthesized powder *J. Eur. Ceram. Soc.* **27** 3775–8
[53] Damjanovic D 1998 Ferroelectric, dielectric and piezoelectric properties of ferroelectric thin films and ceramics *Rep. Prog. Phys.* **61** 1267–324

Supplementary material

Multifunctional energy storage and piezoelectric properties of 0.65Pb($Mg_{1/3}Nb_{2/3}$)O_3–0.35$PbTiO_3$ thick films on stainless-steel substrates

Matej Sadl[1,2], Kevin Nadaud[3], Micka Bah[3], Franck Levassort[3], Udo Eckstein[4], Neamul H. Khansur[4], Kyle G. Webber[4] and Hana Ursic[1,2,*]

[1]Electronic Ceramics Department, Jožef Stefan Institute, Jamova cesta 39, 1000 Ljubljana, Slovenia;

[2]Jožef Stefan International Postgraduate School, Jamova cesta 39, 1000 Ljubljana, Slovenia;

[3]GREMAN UMR 7347, Université de Tours, CNRS, INSA CVL, 16 rue Pierre et Marie Curie, 37071 TOURS Cedex 2, France;

[4]Department of Materials Science and Engineering, Friedrich-Alexander-Universität Erlangen-Nürnberg (FAU), 91058 Erlangen, Germany.

*Correspondence: hana.ursic@ijs.si

S1: Aerosol deposition process parameters

Table S1. Process parameters used during the AD.

Process Parameters	
Carrier gas species	N_2
Nozzle geometry (slit size)	(0.5 × 10) mm^2
Distance between nozzle and substrate	5 mm
Sweep speed	5 $mm \cdot s^{-1}$
Gas flow rate	4 $L \cdot min^{-1}$
Pressure in aerosol chamber	180 mbar
Pressure in deposition chamber	2 mbar

S2: Rietveld refinement

A quantitative analysis of the XRD data was performed using the Rietveld refinement method. The measured XRD patterns and the corresponding calculated profiles after Rietveld refinement of the PMN–35PT powder, as-deposited thick film and annealed thick film are shown in Figure S2. The agreement factors and unit cell parameters of the Rietveld refinement are listed in Table S2.

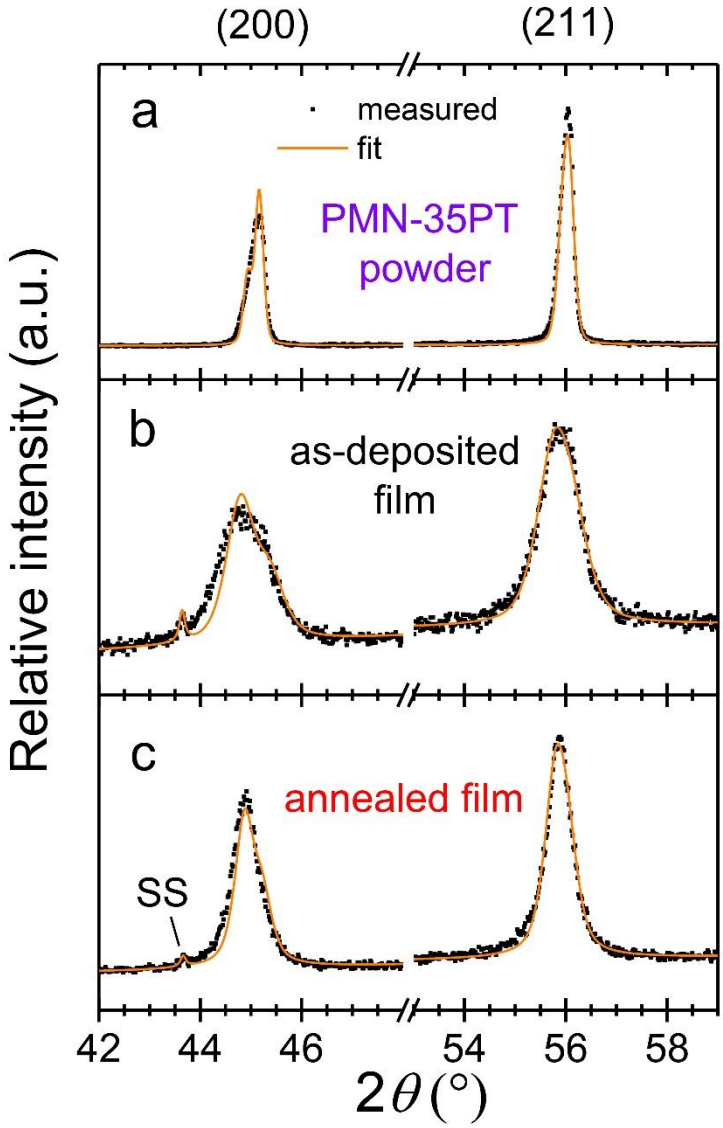

Figure S2: The measured XRD patterns (black) and the corresponding calculated profiles (orange) of (200) and (211) PMN–35PT reflections for (a) PMN–35PT powder, (b) as-deposited thick film and (c) annealed thick film. A cubic (*Fm*-3*m*) crystal structure was used to fit the stainless-steel (SS) reflections originating from the substrate.

Table S2. Agreement factors of the Rietveld refinement.

Sample	PMN–35PT powder	As-deposited film	Annealed film
Crystal system	Tetragonal	Tetragonal	Tetragonal
Space group	*P*4*mm*	*P*4*mm*	*P*4*mm*
a (Å)	4.01098(8)	3.99538(54)	4.01024(38)
c (Å)	4.03040(11)	4.04584(30)	4.04047(21)
R_{wp} (%)	14.49	8.27	8.95
R_{exp} (%)	10.28	7.13	7.14
R_p (%)	11.47	5.82	6.26
G. O. F.	1.41	1.16	1.25

S3: Dielectric properties as a function of temperature

The relative dielectric permittivity and dielectric losses (*tan δ*) were measured between 5 and 300 °C with a Precision LCR impedance meter (HP 4284A, Hewlett-Packard, USA) in the frequency range 1–100 kHz. Figure S3 reveals a remarkable increase of dielectric permittivity after thermal annealing of thick films at 500 °C. During heating, the dielectric permittivity of the as-deposited films increases, while the annealed films exhibit a broad frequency-dependent dielectric permittivity maximum at ~150°C. The *tan δ* of thick films stays below 0.1, except for the as-deposited thick films at elevated temperatures (above ~200 °C). Note that the electrical response of as-deposited films is dominated by the defects, which are generated after AD. The reason for increase of *tan δ* with increasing temperature can be attributed to the relaxation of space charges, that become mobile at higher temperatures.

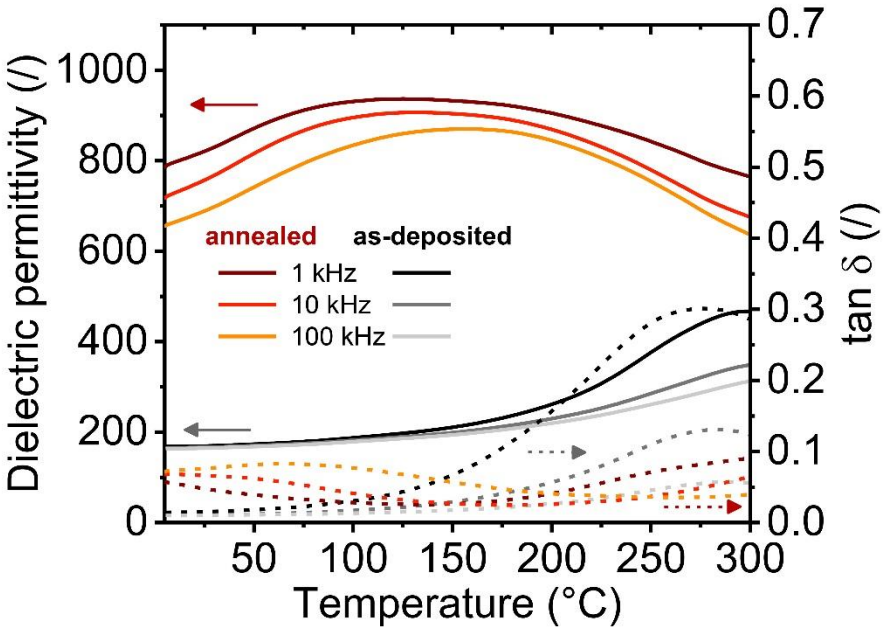

Figure S3: The relative dielectric permittivity (solid line) and *tan δ* (dashed line) vs. temperature of as-deposited (black-grey) and annealed (red-orange) PMN–35PT films.

S4: Polarization vs. electric field loops at various frequencies

The unipolar polarization–electric field (*P*–*E*) hysteresis loops as-deposited and annealed PMN–35PT thick films were measured at room temperature using an aixACCT TF analyzer 2000 (aixACCT Systems GmbH, Germany). The single sinusoidal waveform up to an amplitude of 500 kV·cm^{-1} and at frequencies from 1 to 100 Hz was applied on top Au electrodes with the diameter of 1.5 mm.

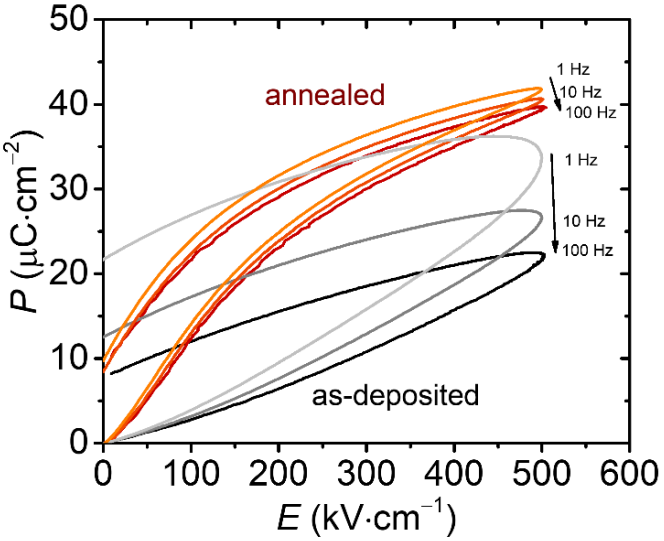

Figure S4: Unipolar *P*–*E* hysteresis loops of as-deposited (grey to black lines) and annealed (orange to red lines) thick films. *P*–*E* loops were measured up to 500 kV·cm^{-1} and at frequencies from 1 to 100 Hz.

S5: Dielectric breakdown measurements – Weibull analysis

Dielectric breakdown measurements of as-deposited and annealed PMN–35PT thick films were performed using an aixACCT TF analyzer 2000 (aixACCT Systems GmbH, Germany) by applying a single sinusoidal unipolar waveform with a frequency of 100 Hz. To evaluate the dielectric breakdown fields (E_i), 10 Au top electrodes (1.5 mm diameter) of each sample were used. The evaluated E_i follow the two-parameter Weibull distribution described by [RS1, RS2]:

$$X_i = \ln(E_i) \tag{S5.1}$$

$$Y_i = \ln(-\ln(1 - p_i)) \tag{S5.2}$$

$$p_i = \frac{i - 0.3}{N + 0.4} \tag{S5.3}$$

Here i, N and p_i represent the specimen sequential number, the sum of the tested specimens and the cumulative probability of dielectric breakdown, respectively. A high shape factor ($\beta > 1$), determined from the slope of the Weibull distribution, indicates low fluctuations of E_i in the as-deposited and annealed samples. The dielectric breakdown strength (DBS) is extracted from the intersection of the linear regression curve and the horizontal line $\ln(-\ln(1-p_i)) = 0$. It represents the electric field at which the breakdown probability is 63.2%.

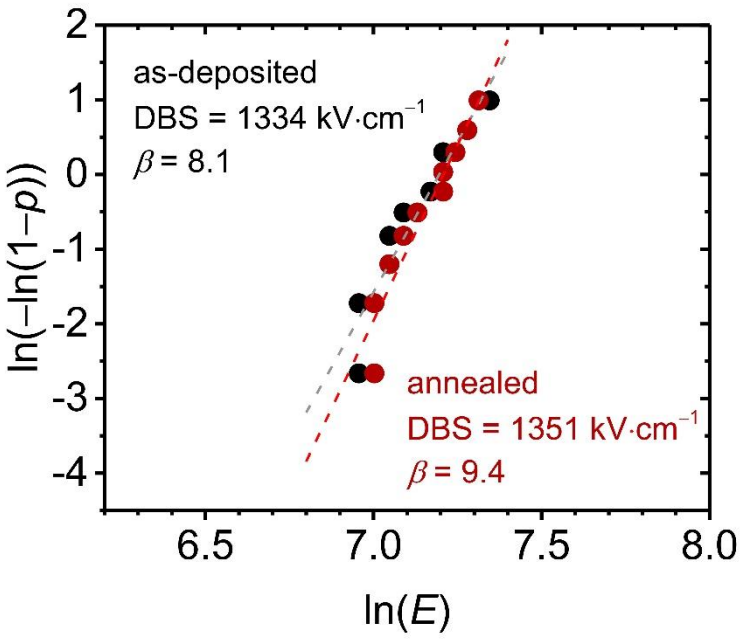

Figure S5: Weibull distribution of the dielectric breakdown field of as-deposited (black) and annealed (red) PMN–35PT thick films. The dashed lines represent linear regression.

S6: Macroscopic displacement measurements with a single and double beam laser interferometer

The macroscopic displacement measurements were performed on annealed PMN–35PT thick films. The bipolar strain–electric field hysteresis loops of the films were measured at room temperature using a single beam laser interferometer (SBLI, aixACCT TF analyzer 2000, aixACCT Systems GmbH, Germany) and a double beam laser interferometer (DBLI, AixACCT DBLI, aixACCT Systems GmbH, Germany). The applied electric field had a single sinusoidal waveform with a frequency of 100 Hz. The inverse effective piezoelectric coefficients $d^{*,+}_{33\,eff}$ and $d^{*,-}_{33\,eff}$ were determined using a linear regression of the positive and negative electric field (i.e., the right and left sides of the strain–electric field hysteresis loops), respectively.

The $d^{*}_{33\,eff}$ values measured with a SBLI and a DBLI are comparable despite the different measurement techniques. It is known that SBLI can overestimate the $d^{*}_{33\,eff}$ value due to a contribution from substrate bending, which is not the case with DBLI measurements. However, similar values of $d^{*}_{33\,eff}$ indicate that there is no significant contribution from substrate bending in SBLI measurements.

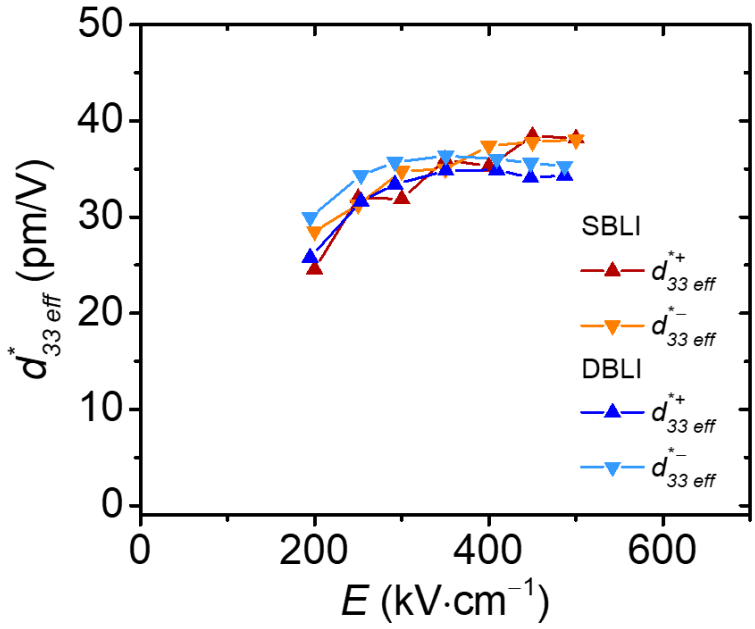

Figure S6: The $d^{*}_{33\,eff}$ vs. *E* of annealed thick films measured with a SBLI (red and orange) and DBLI (dark and light blue) method.

References

[RS1] E. Tuncer, D. R. James, I. Sauers, A. R. Ellis, and M. O. Pace, "On dielectric breakdown statistics," *J. Phys. D: Appl. Phys.*, vol. 39, no. 19, pp. 4257–4268, 2006.

[RS2] J. Li, Z. Shen, X. Chen, S. Yang, W. Zhou, M. Wang, L. Wang, Q. Kou, Y. Liu, Q. Li, Z. Xu, Y. Chang, S. Zhang, and F. Li, "Grain-orientation-engineered multilayer ceramic capacitors for energy storage applications," *Nat. Mater.*, vol. 19, no. 9, pp. 999–1005, 2020.

Chapter 5

Summary and Conclusions

In the scope of this thesis we prepared and characterized new relaxor-ferroelectric thick-film structures by depositing PMN–10PT and PMN–35PT on low-cost SS and flexible PI substrates. We applied an AD method that enables ceramic-metal and ceramic-polymer integration, which can significantly impact the availability and affordability of future electronic devices and energy systems, such as capacitive energy storage, energy harvesting, actuators and sensors.

Based on the results, the following conclusions can be drawn:

- The room-temperature AD of PMN–10PT and PMN–35PT thick films on low-cost substrates was investigated for the first time. The objective, i.e., to deposit functional ceramic thick films on substrates incompatible with high-temperature sintering process, was achieved.
- After mechanochemically assisted synthesis, the PMN–10PT powder obtains nanocrystalline particles (size less than 100 nm), which are not acceptable for AD because too small particles do not undergo typical fragmentation and re-bonding in the deposition process. This fully confirms the hypotheses 1 and 2, that heating of such powders is needed to increase the crystallite size, which leads to a successful AD.
- Controlling the material parameters is crucial to successful AD. The properties of PMN–10PT powder were modified by heating and milling treatments. Such treatments resulted in highly crystalline powders with an average crystallite size of ~180 nm, with particles of several hundred nm in size and without excessive agglomeration. This supports hypothesis 1, which predicts that only powders with particles in the range of several hundred nm are capable of forming consolidated PMN–10PT and PMN–35PT thick films.
- We prepared PMN–10PT thick films on SS and PI substrates and PMN–35PT on SS substrates. The optimized PMN–10PT and PMN–35PT powders resulted in dense and few-µm-thick films with very low porosity (1.5–3.0%, see Table 5.1), good adhesion and a homogeneous film surface and thickness. Thus, the objective of depositing high-density PMN–10PT and PMN–35PT thick films was achieved.
- After the deposition at room temperature, the thick films were thermally annealed at 400 °C (for PI substrates) and 500 °C (for SS substrates). The thermal annealing up to 500 °C does not change the microstructure of the ceramic thick films, i.e., the crystallite and grain growth are insignificant and the density remains same. The annealing temperatures are much lower than the temperatures of ceramic sintering. This conclusion supports hypothesis 3.
- The thermal annealing causes stress relaxation in PMN–10PT and PMN–35PT thick films, which is evident from the peak shifting in the tilt-angle-dependent XRD and the

shift of the Raman modes. In addition, thermal annealing between 400 °C and 500 °C also causes microstrain reduction up to 50% (Table 5.1). The findings confirm hypothesis 4, which assumes significant stress relaxation after thermal annealing.

- The DBS of PMN–10PT and PMN–35PT thick films reaches 900 $kV \cdot cm^{-1}$ or even more, which is one order of magnitude higher than that of bulk ceramic ferroelectrics. The contributing factors to a high DBS are high density/low porosity, small thickness of the order of µm and a small grain size. These results agree with hypothesis 5, which also predicts that the DBS does not change after post-deposition thermal annealing due to the preserved microstructure.
- As-deposited PMN–10PT and PMN–35PT thick films fabricated completely at room temperature show promising energy-storage properties. The U_{rec} and η reach values in the range 5.1–7.0 $J \cdot cm^{-3}$ and 38–69% at 900 $kV \cdot cm^{-1}$, respectively (Table 5.1). Moreover, the stress relaxation by thermal annealing improves the energy-storage properties. After thermal annealing, U_{rec} and η reach values in the range 8.8–9.8 $J \cdot cm^{-3}$ and 61–79% at 900 $kV \cdot cm^{-1}$, respectively. The highest U_{rec} (9.8 $J \cdot cm^{-3}$) is achieved in the PMN–10PT thick films on SS, since they exhibit the largest polarization. In comparison to PMN–35PT, PMN–10PT thick films reach a higher η due to the lower hysteresis losses. These results confirm hypotheses 4 and 6, predicting that stress relaxation improves the energy-storage properties, which are higher than in their bulk ceramic counterparts.
- Overall, the thermally annealed PMN–10PT and PMN–35PT thick films prepared in this work on low-cost substrates have energy-storage properties comparable to those of other AD thick films in the literature (Figure 5.1). However, the vast majority of the reported AD thick films were fabricated on much more expensive platinized silicon substrates.
- The PMN–10PT and PMN–35PT thick films on SS endure a large number of cycles in the electrical fatigue test. The PMN–10PT and PMN–35PT thick films endure $16 \cdot 10^6$ and $5 \cdot 10^6$ cycles, respectively (Table 5.1), which confirms hypothesis 7. The lower performance of the PMN–35PT thick film might be related to the increased hysteretic polarization losses.
- The ceramic-polymer PMN–10PT on PI structures exhibits excellent flexibility without fatigue by a tensile bending radius of up to 3 mm and 10^5 bending cycles (Table 5.1). These results confirm hypothesis 8, which predicts that the thick films withstand bending without a degradation of energy-storage performance.
- The direct and inverse electromechanical measurements reveal a piezoelectric activity of PMN–35PT thick film on SS. The as-deposited and annealed thick films reach a $d^*_{33\,eff}$ of 25 and 41 $pm \cdot V^{-1}$, respectively (Table 5.1). This supports hypothesis 9, assuming that in piezoelectrically active as-deposited thick films the piezoelectric response increases after thermal annealing. However, the piezoelectric performance reported here and that of other PMN–100xPT thick and thin films [107], [121], are significantly lower than that of PMN–35PT ceramics (reaching d_{33} typically above 525 $pC \cdot N^{-1}$ [79]). The reason for that can be found in a strong film-substrate clamping effect and a much smaller grain size in the films.

Table 5.1: Comparison of the properties of PMN–100xPT thick films.

	thick film structures	PMN–10PT on SS		PMN–10PT on PI		PMN–35PT on SS	
	post-deposition annealing	as-deposited	500 °C	as-deposited	400 °C	as-deposited	500 °C
SEM	porosity (%)	1.6 ± 1.0	1.5 ± 1.0	2.0 ± 1.0	2.0 ± 1.0	3.0 ± 1.0	3.0 ± 1.0
XRD	cry. size (nm)	33 ± 1	38 ± 2	49 ± 13	51 ± 6	17.2 ± 0.3	21.9 ± 0.3
	microstrain (10^{-4})	25.9 ± 0.3	13.7 ± 0.3	34.4 ± 6.3	24.1 ± 3.0	22.7 ± 2.1	13.4 ± 1.2
	reduction of microstrain after annealing (%)	-	47	-	30	-	41
energy-storage	U_{rec} ($J \cdot cm^{-3}$) at 900 $kV \cdot cm^{-1}$	7.0	9.8	5.1	8.8	6.6	9.6
	η (%) at 900 $kV \cdot cm^{-1}$	68	79	69	73	38	61
	relative U_{rec} (%)[1] at 500 $kV \cdot cm^{-1}$ (after electrical fatigue of N cycles)	65% ($16 \cdot 10^6$)	90% ($16 \cdot 10^6$)	-	-	60% ($5 \cdot 10^6$)	82% ($5 \cdot 10^6$)
	relative U_{rec} (%)[1] at 500 $kV \cdot cm^{-1}$ (after N bending cycles with $r = 3$ mm)	-	-	95% (10^5)	100% (10^5)	-	-
electro-mechanical	$d^*_{33,eff.}$ ($pm \cdot V^{-1}$) measured by SBLI	-	-	-	-	25	41

[1] relative $U_{rec}(\%) = \dfrac{U_{rec} \text{ before el. fatigue/bending}}{U_{rec} \text{ after el. fatigue/bending of } N \text{ cycles}}$

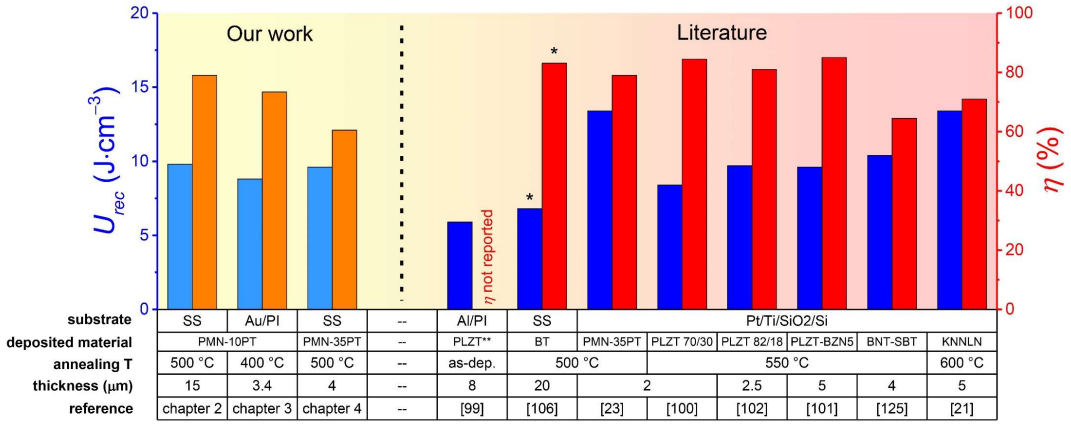

substrate	SS	Au/PI	SS	--	Al/PI	SS	Pt/Ti/SiO2/Si					
deposited material	PMN-10PT		PMN-35PT	--	PLZT**	BT	PMN-35PT	PLZT 70/30	PLZT 82/18	PLZT-BZN5	BNT-SBT	KNNLN
annealing T	500 °C	400 °C	500 °C	--	as-dep.	500 °C		550 °C				600 °C
thickness (µm)	15	3.4	4	--	8	20	2		2.5	5	4	5
reference	chapter 2	chapter 3	chapter 4	--	[99]	[106]	[23]	[100]	[102]	[101]	[125]	[21]

Figure 5.1: Comparison of the energy-storage properties of AD thick films. The plot shows the U_{rec} (blue) and η (orange and red) of thick films at 900 kV · cm^{-1}. The left- and right-hand sides show data from our work and the literature, respectively. Our PMN–100xPT thick films were deposited on SS and golden polyimide (Au/PI), while others also used platinized silicon (Pt/Ti/SiO_2/Si) and aluminium-metallized polyimide (Al/PI) as substrates. The deposited thick films were $0.942(Na_{0.535}K_{0.480})NbO_3$–$0.058LiNbO_3$ (KNNLN), $0.95(Pb_{0.92}La_{0.08})(Zr_{0.52}Ti_{0.48})O_3$–$0.05Bi(Zn_{0.66}Nb_{0.33})O_3$ (PLZT–BZN5), $(Pb_{0.89}La_{0.11})(Zr_{0.70}Ti_{0.30})O_3$ (PLZT 70/30), $(Pb_{0.93}La_{0.07})(Zr_{0.82}Ti_{0.18})O_3$ (PLZT 82/18), $BaTiO_3$ (BT), $0.6(Bi_{0.5}Na_{0.5})TiO_3$–$0.4(Sr_{0.7}Bi_{0.2})TiO_3$ (BNT–SBT) [122]. Note that the data marked with * were measured at 1000 kV · cm^{-1}. For PLZT** thick films the chemical composition was not reported [99].

We can conclude that the three different thick-film structures demonstrated and evaluated in this thesis have great potential for future capacitive energy-storage and electro-mechanical applications:

- PMN–10PT thick films on SS exhibit efficient energy-storage properties, reliable electrical fatigue endurance and high-temperature stability, making them particularly promising for reliable and cost-effective energy-storage applications.
- The PMN–10PT thick films on PI presented here are one of the first ceramic-polymer layered structures to offer high energy-storage performance and flexural endurance for future flexible and mechanically robust energy-storage devices.
- PMN–35PT thick films on SS exhibit a high recoverable energy-storage density and electro-mechanical properties, which make them attractive for multifunctional applications such as autonomous sensors for the Internet of Things or small portable microelectronic devices that have both energy-storage and energy-harvesting functions.

Here, we summarize future work that may be of importance for developments in the field of AD thick films:

- Considering the electro-mechanical potential of PMN–35PT thick films demonstrated on SS substrates, future research needs to focus on the deposition of PMN–35PT thick films on flexible PI for future electromechanical applications such as flexible energy harvesting.
- The AD method can be used to deposit not only single-phase ceramic materials, but also mixed composites. The method, known as aerosol co-deposition, can incorporate ferroelectric polymers such as polyvinylidene fluoride (PVDF) into ceramic thick films. The PVDF, in a mixed ceramic-polymer composite (e.g., PMN–100xPT/PVDF), can

improve energy-storage properties by increasing DBS and maintaining maximum polarization.

- Further work needs to be done to evaluate the relationship between the processing of the different ceramic powders and the final film-deposition behavior. This is important in order to deposit a wider variety of new ceramic materials in the form of thick films.
- Due to its low-temperature operation and fast deposition rate, AD has been referred to as a cost-effective film-deposition method. However, to bring AD into mass production, which could have a significant impact on the availability and affordability of future electronic devices, the AD method requires further research and innovation in process engineering.

References

[1] R. A. Dorey, *Ceramic Thick Films for MEMS and Microdevices*. Oxford: Elsevier, 2012.

[2] M. Kosec, D. Kuscer, and J. Holc, "Processing of Ferroelectric Ceramic Thick Films," in *Multifunctional Polycrystalline Ferroelectric Materials*, Dordrecht: Springer, 2011.

[3] S. J. L. Kang, *Sintering*. Oxford: Elsevier, 2005.

[4] J. Akedo, "Room Temperature Impact Consolidation (RTIC) of Fine Ceramic Powder by Aerosol Deposition Method and Applications to Microdevices," *J. Therm. Spray Technol.*, vol. 17, no. 2, pp. 181–198, 2008.

[5] D. Hanft, J. Exner, M. Schubert, T. Stöcker, P. Fuierer, and R. Moos, "An overview of the Aerosol Deposition method: Process fundamentals and new trends in materials applications," *J. Ceram. Sci. Technol.*, vol. 6, no. 3, pp. 147–181, 2015.

[6] J. Akedo, "Aerosol deposition of ceramic thick films at room temperature: Densification mechanism of ceramic layers," *J. Am. Ceram. Soc.*, vol. 89, no. 6, pp. 1834–1839, 2006.

[7] M. Schubert, N. Leupold, J. Exner, J. Kita, and R. Moos, "High-Temperature Electrical Insulation Behavior of Alumina Films Prepared at Room Temperature by Aerosol Deposition and Influence of Annealing Process and Powder Impurities," *J. Therm. Spray Technol.*, vol. 27, no. 5, pp. 870–879, 2018.

[8] J. Ryu, D.-S. Park, B.-D. Hahn, J.-J. Choi, W.-H. Yoon, K.-Y. Kim, and H.-S. Yun, "Photocatalytic TiO_2 thin films by aerosol-deposition: From micron-sized particles to nano-grained thin film at room temperature," *Appl. Catal. B Environ.*, vol. 83, no. 1–2, pp. 1–7, 2008.

[9] B.-K. Lee, D.-S. Park, W.-H. Yoon, J.-H. Ryu, B.-D. Hahn, and J.-J. Choi, "Microstructure and Properties of Yttria Film Prepared by Aerosol Deposition," *J. Korean Ceram. Soc.*, vol. 46, no. 5, pp. 441–446, 2009.

[10] J. Exner, G. Albrecht, D. Schönauer-Kamin, J. Kita, and R. Moos, "Pulsed polarization-based NO_x sensors of YSZ films produced by the aerosol deposition method and by screen-printing," *Sensors (Basel)*, vol. 17, no. 8, p. 1715, 2017.

[11] C.-C. Hsiao and S.-Y. Yu, "Rapid deposition process for zinc oxide film applications in pyroelectric devices," *Smart Mater. Struct.*, vol. 21, no. 10, p. 105012, 2012.

[12] S. Baba, H. Tsuda, and J. Akedo, "Thickness dependence of electrical properties of PZT films deposited on metal substrates by laser-assisted aerosol deposition," *IEEE Trans. Ultrason. Ferroelectr. Freq. Control*, vol. 55, no. 5, pp. 1009–1016, 2008.

[13] J.-M. Oh and S.-M. Nam, "Role of Surface Hardness of Substrates in Growing

$BaTiO_3$ Thin Films by Aerosol Deposition Method," *Jpn. J. Appl. Phys.*, vol. 48, no. 9, p. 09KA07, 2009.

[14] J.-J. Choi, J. Ryu, B.-D. Hahn, W.-H. Yoon, and D.-S. Park, "Room-Temperature Conducting $LaNiO_3$ Thick-Film Coatings Prepared by Aerosol Deposition," *J. Am. Ceram. Soc.*, vol. 91, no. 8, pp. 2756–2758, 2008.

[15] Y.-C. Wu, S.-F. Wang, and L.-G. Teng, "Microstructures and Dielectric Properties of $MgTiO_3$ Thick Film Prepared Using Aerosol Deposition Method," *Ferroelectrics*, vol. 435, no. 1, pp. 137–147, 2012.

[16] J.-J. Choi, J.-H. Lee, D.-S. Park, B.-D. Hahn, W.-H. Yoon, and H.-T. Lin, "Oxidation Resistance Coating of LSM and LSCF on SOFC Metallic Interconnects by the Aerosol Deposition Process," *J. Am. Ceram. Soc.*, vol. 90, no. 6, pp. 1926–1929, 2007.

[17] J.-J. Choi, J. Ryu, B.-D. Hahn, C.-W. Ahn, J.-W. Kim, W.-H. Yoon, and D.-S. Park, "Low temperature preparation and characterization of solid oxide fuel cells on FeCr-based alloy support by aerosol deposition," *Int. J. Hydrogen Energy*, vol. 39, no. 24, pp. 12878–12883, 2014.

[18] J. Exner, T. Nazarenus, J. Kita, and R. Moos, "Dense Y-doped ion conducting perovskite films of $BaZrO_3$, $BaSnO_3$, and $BaCeO_3$ for SOFC applications produced by powder aerosol deposition at room temperature," *Int. J. Hydrogen Energy*, vol. 45, no. 16, pp. 10000–10016, 2020.

[19] J. Ryu, J.-J. Choi, B.-D. Hahn, D.-S. Park, and W.-H. Yoon, "Ferroelectric and piezoelectric properties of $0.948(K_{0.5}Na_{0.5})NbO_3 - 0.052LiSbO_3$ lead-free piezoelectric thick film by aerosol deposition," *Appl. Phys. Lett.*, vol. 92, no. 1, p. 012905, 2008.

[20] M. Peddigari, H. Palneedi, G. T. Hwang, K. W. Lim, G. Y. Kim, D. Y. Jeong, and J. Ryu, "Boosting the Recoverable Energy Density of Lead-Free Ferroelectric Ceramic Thick Films through Artificially Induced Quasi-Relaxor Behavior," *ACS Appl. Mater. Interfaces*, vol. 10, no. 24, pp. 20720–20727, 2018.

[21] J. Ryu, J.-J. Choi, B.-D. Hahn, D.-S. Park, W.-H. Yoon, and K.-H. Kim, "Fabrication and ferroelectric properties of highly dense lead-free piezoelectric $(K_{0.5}Na_{0.5})NbO_3$ thick films by aerosol deposition," *Appl. Phys. Lett.*, vol. 90, no. 15, p. 152901, 2007.

[22] J. Ryu, C.-W. Baek, D.-S. Park, and D.-Y. Jeong, "Multiferroic $BiFeO_3$ thick film fabrication by aerosol deposition," *Met. Mater. Int.*, vol. 16, no. 4, pp. 639–642, 2010.

[23] C. K. Park, S. H. Lee, J. H. Lim, J. Ryu, D. H. Choi, and D. Y. Jeong, "Nano-size grains and high density of 65PMN-35PT thick film for high energy storage capacitor," *Ceram. Int.*, vol. 44, no. 16, pp. 20111–20114, 2018.

[24] T. Nazarenus, J. Kita, R. Moos, and J. Exner, "Laser-Annealing of Thermoelectric $CuFe_{0.98}Sn_{0.02}O_2$ Films Produced by Powder Aerosol Deposition Method," *Adv. Mater. Interfaces*, vol. 7, no. 22, pp. 1–13, 2020.

[25] M. Lebedev, J. Akedo, A. Iwata, S. Sugimoto, and K. Inomata, "NiZnCu Ferrite Thick Film with Nano Scale Crystallites Formed by the Aerosol Deposition Method," *J. Am. Ceram. Soc.*, vol. 87, no. 9, pp. 1621–1624, 2004.

[26] M. Schubert, C. Münch, S. Schuurman, V. Poulain, J. Kita, and R. Moos,

"Characterization of nickel manganite NTC thermistor films prepared by aerosol deposition at room temperature," *J. Eur. Ceram. Soc.*, vol. 38, no. 2, pp. 613–619, 2018.

[27] D.-S. Park, I.-S. Kim, H. Kim, A. H. K. Chou, B.-D. Hahn, L.-H. Li, and S.-J. Hwang, "Improved biocompatibility of hydroxyapatite thin film prepared by aerosol deposition," *J. Biomed. Mater. Res. Part B Appl. Biomater.*, vol. 94B, no. 2, pp. 353–358, 2010.

[28] Y. J. Heo, H. T. Kim, K. J. Kim, S. Nahm, Y. J. Yoon, and J. Kim, "Enhanced heat transfer by room temperature deposition of AlN film on aluminum for a light emitting diode package," *Appl. Therm. Eng.*, vol. 50, no. 1, pp. 799–804, 2013.

[29] Y.-H. Kim, J.-W. Lee, H.-J. Kim, Y.-H. Yun, and S.-M. Nam, "Silver metallization for microwave device using aerosol deposition," *Ceram. Int.*, vol. 38, pp. S201–S204, 2012.

[30] S. Baba, L. Huang, H. Sato, R. Funahashi, and J. Akedo, "Room-temperature fast deposition and characterization of nanocrystalline $Bi_{0.4}Sb_{1.6}Te_3$ thick films by aerosol deposition," *J. Phys. Conf. Ser.*, vol. 379, no. 1, p. 012011, 2012.

[31] S. Sugimoto, M. Nakamura, T. Maki, T. Kagotani, K. Inomata, J. Akedo, S. Hirosawa, and Y. Shigemoto, "$Nd_2Fe_{14}B/Fe_3B$ nanocomposite film fabricated by aerosol deposition method," *J. Alloys Compd.*, vol. 408–412, pp. 1413–1416, 2006.

[32] S. Sugimoto, T. Hirayama, T. Maki, T. Kagotani, K. Inomata, and J. Akedo, "Fabrication of Anisotropic SmFeN Films using the Aerosol Deposition Method," *J. Japan Soc. Powder Powder Metall.*, vol. 53, no. 3, pp. 258–262, 2006.

[33] Y. Imanaka, "Materials and Processes of Microelectronic Packaging including Low-Temperature Cofired Ceramics Technology (Past, Present and Future)," *J. Ceram. Sci. Technol.*, vol. 6, no. 4, pp. 291–300, 2015.

[34] Y. Imanaka, H. Amada, and F. Kumasaka, "Microstructure and Dielectric Properties of Composite Films for Embedded Capacitor Applications," *Int. J. Appl. Ceram. Technol.*, vol. 8, no. 3, pp. 653–657, 2011.

[35] B.-D. Hahn, D.-S. Park, J.-J. Choi, J. Ryu, W.-H. Yoon, J.-H. Choi, H.-E. Kim, and S.-G. Kim, "Aerosol deposition of hydroxyapatite–chitosan composite coatings on biodegradable magnesium alloy," *Surf. Coatings Technol.*, vol. 205, no. 8–9, pp. 3112–3118, Jan. 2011.

[36] J. Iwasawa, R. Nishimizu, M. Tokita, M. Kiyohara, and K. Uematsu, "Plasma-Resistant Dense Yttrium Oxide Film Prepared by Aerosol Deposition Process," *J. Am. Ceram. Soc.*, vol. 90, no. 8, pp. 2327–2332, 2007.

[37] J. Exner, M. Hahn, M. Schubert, D. Hanft, P. Fuierer, and R. Moos, "Powder requirements for aerosol deposition of alumina films," *Adv. Powder Technol.*, vol. 26, no. 4, pp. 1143–1151, 2015.

[38] M. Schubert, M. Hahn, J. Exner, J. Kita, and R. Moos, "Effect of substrate hardness and surface roughness on the film formation of aerosol-deposited ceramic films," *Funct. Mater. Lett.*, vol. 10, no. 4, p. 1750045, 2017.

[39] Y. Imanaka, N. Hayashi, M. Takenouchi, and J. Akedo, "Aerosol deposition for post-LTCC," *J. Eur. Ceram. Soc.*, vol. 27, no. 8–9, pp. 2789–2795, 2007.

[40] J. Akedo, N. Minami, K. Fukuda, M. Ichiki, and R. Maeda, "Electrical properties

of direct deposited piezoelectric thick film formed by gas deposition method annealing effect of the deposited films," *Ferroelectrics*, vol. 231, no. 1, pp. 285–292, 1999.

[41] N. H. Khansur, U. Eckstein, L. Benker, U. Deisinger, B. Merle, and K. G. Webber, "Room temperature deposition of functional ceramic films on low-cost metal substrate," *Ceram. Int.*, vol. 44, no. 14, pp. 16295–16301, 2018.

[42] D.-W. Lee and S.-M. Nam, "Factors affecting surface roughness of Al_2O_3 films deposited on Cu substrates by an aerosol deposition method," *J. Ceram. Process. Res.*, vol. 11, no. 1, pp. 100–106, 2010.

[43] N. Leupold, M. Schubert, J. Kita, and R. Moos, "Influence of high temperature annealing on the dielectric properties of alumina films prepared by the aerosol deposition method," *Funct. Mater. Lett.*, vol. 11, no. 2, pp. 1–4, 2018.

[44] D. Hanft, M. Bektas, and R. Moos, "Powder Pre-Treatment for Aerosol Deposition of Tin Dioxide Coatings for Gas Sensors," *Materials*, vol. 11, no. 8, p. 1342, 2018.

[45] S.-M. Nam, N. Mori, H. Kakemoto, S. Wada, J. Akedo, and T. Tsurumi, "Alumina Thick Films as Integral Substrates Using Aerosol Deposition Method," *Jpn. J. Appl. Phys.*, vol. 43, no. 8A, pp. 5414–5418, 2004.

[46] J. Ryu, K.-Y. Kim, J.-J. Choi, B.-D. Hahn, W.-H. Yoon, B.-K. Lee, D.-S. Park, D.-Y. Jeong, and C. Park, "Flexible Dielectric $Bi_{1.5}Zn_{1.0}Nb_{1.5}O_7$ Thin Films on a Cu-Polyimide Foil," *J. Am. Ceram. Soc.*, vol. 92, no. 2, pp. 524–527, 2009.

[47] Y. Taira, H. Hatono, M. Tokita, and T. Sawase, "Thickness and surface structure of a ceramic layer created on three indirect resin composites with aerosol deposition," *J. Prosthodont. Res.*, vol. 54, no. 4, pp. 168–172, 2010.

[48] M. A. Piechowiak, J. Henon, O. Durand-Panteix, G. Etchegoyen, V. Coudert, P. Marchet, and F. Rossignol, "Growth of dense Ti_3SiC_2 MAX phase films elaborated at room temperature by aerosol deposition method," *J. Eur. Ceram. Soc.*, vol. 34, no. 5, pp. 1063–1072, 2014.

[49] S.-C. Lin and W.-J. Wu, "Fabrication of PZT MEMS energy harvester based on silicon and stainless-steel substrates utilizing an aerosol deposition method," *J. Micromechanics Microengineering*, vol. 23, no. 12, p. 125028, 2013.

[50] J. Akedo and M. Lebedev, "Microstructure and Electrical Properties of Lead Zirconate Titanate ($Pb(Zr_{52}/Ti_{48})O_3$) Thick Films Deposited by Aerosol Deposition Method," *Jpn. J. Appl. Phys.*, vol. 38, no. 9B, pp. 5397–5401, 1999.

[51] K. Mihara, T. Hoshina, H. Takeda, and T. Tsurumi, "Controlling factors of film-thickness in improved aerosol deposition method," *J. Ceram. Soc. Japan*, vol. 117, no. 1368, pp. 868–872, 2009.

[52] D.-W. Lee, H.-J. Kim, Y.-H. Kim, Y.-H. Yun, and S.-M. Nam, "Growth Process of alpha-Al_2O_3 Ceramic Films on Metal Substrates Fabricated at Room Temperature by Aerosol Deposition," *J. Am. Ceram. Soc.*, vol. 94, no. 9, pp. 3131–3138, 2011.

[53] M. Sadl, U. Tomc, U. Prah, and H. Ursic, "Protective Alumina Coatings Prepared by Aerosol Deposition on Magnetocaloric Gadolinium Elements," *Inf. MIDEM - J. Microelectron. Electron. Components Mater.*, vol. 49, no. 3, pp. 177–182, 2019.

[54] J. Akedo and M. Lebedev, "Powder Preparation in Aerosol Deposition Method for Lead Zirconate Titanate Thick Films," *Jpn. J. Appl. Phys.*, vol. 41, no. 11B, pp.

6980–6984, 2002.

[55] J. Exner, M. Schubert, D. Hanft, J. Kita, and R. Moos, "How to treat powders for the room temperature aerosol deposition method to avoid porous, low strength ceramic films," *J. Eur. Ceram. Soc.*, vol. 39, no. 2–3, pp. 592–600, 2019.

[56] J. Akedo, "Aerosol Deposition Method for Fabrication of Nano Crystal Ceramic Layer," *Mater. Sci. Forum*, vol. 449–452, pp. 43–48, 2004.

[57] J. Henon, M. A. Piechowiak, O. Durand-Panteix, G. Etchegoyen, O. Masson, C. Dublanche-Tixier, P. Marchet, B. Lucas, and F. Rossignol, "Dense and highly textured coatings obtained by aerosol deposition method from Ti_3SiC_2 powder: Comparison to a dense material sintered by spark plasma sintering," *J. Eur. Ceram. Soc.*, vol. 35, no. 4, pp. 1179–1189, 2015.

[58] S.-Q. Fan, C.-J. Li, G.-J. Yang, L.-Z. Zhang, J.-C. Gao, and Y.-X. Xi, "Fabrication of Nano-TiO_2 Coating for Dye-Sensitized Solar Cell by Vacuum Cold Spraying at Room Temperature," *J. Therm. Spray Technol.*, vol. 16, no. 5–6, pp. 893–897, 2007.

[59] D.-M. Chun and S.-H. Ahn, "Deposition mechanism of dry sprayed ceramic particles at room temperature using a nano-particle deposition system," *Acta Mater.*, vol. 59, no. 7, pp. 2693–2703, 2011.

[60] N. H. Khansur, U. Eckstein, K. Riess, A. Martin, J. Drnec, U. Deisinger, and K. G. Webber, "Synchrotron x-ray microdiffraction study of residual stresses in $BaTiO_3$ films deposited at room temperature by aerosol deposition," *Scr. Mater.*, vol. 157, pp. 86–89, 2018.

[61] M. Schubert, J. Exner, and R. Moos, "Influence of carrier gas composition on the stress of Al_2O_3 coatings prepared by the aerosol deposition method," *Materials*, vol. 7, no. 8, pp. 5633–5642, 2014.

[62] D. Damjanovic, "Ferroelectric, dielectric and piezoelectric properties of ferroelectric thin films and ceramics," *Reports Prog. Phys.*, vol. 61, no. 9, pp. 1267–1324, 1998.

[63] U. Böttger, "Dielectric Properties of Polar Oxides," in *Polar Oxides*, Weinheim: Wiley-VCH Verlag GmbH & Co. KGaA, 2005.

[64] D. Damjanovic, "Hysteresis in Piezoelectric and Ferroelectric Materials," in *The Science of Hysteresis*, vol. 3, San Diego: Elsevier, 2006.

[65] Wikipedia, "Introduction to Inorganic Chemistry/Ionic and Covalent Solids - Structures," 2017. https://en.wikibooks.org/wiki/Introduction_to_Inorganic_Chemistry/Ionic_and_Covalent_Solids_-_Structures (accessed Feb. 07, 2019).

[66] L. E. Cross, "Relaxor ferroelectrics," *Ferroelectrics*, vol. 76, no. 1, pp. 241–267, 1987.

[67] R. A. Cowley, S. N. Gvasaliya, S. G. Lushnikov, B. Roessli, and G. M. Rotaru, "Relaxing with relaxors: a review of relaxor ferroelectrics," *Adv. Phys.*, vol. 60, no. 2, pp. 229–327, 2011.

[68] V. Bovtun, J. Petzelt, V. Porokhonskyy, S. Kamba, and Y. Yakimenko, "Structure of the dielectric spectrum of relaxor ferroelectrics," *J. Eur. Ceram. Soc.*, vol. 21, no. 10–11, pp. 1307–1311, 2001.

[69] R. Pirc and R. Blinc, "Spherical random-bond–random-field model of relaxor ferroelectrics," *Phys. Rev. B*, vol. 60, no. 19, pp. 13470–13478, 1999.

[70] A. A. Bokov, B. J. Rodriguez, X. Zhao, J.-H. Ko, S. Jesse, X. Long, W. Qu, T. H.

Kim, J. D. Budai, A. N. Morozovska, and S. Kojima, "Compositional disorder, polar nanoregions and dipole dynamics in $Pb(Mg_{1/3}Nb_{2/3})O_3$-based relaxor ferroelectrics," *Zeitschrift für Krist.*, vol. 226, no. 2, pp. 99–107, 2011.

[71] P. K. Davies and M. A. Akbas, "Chemical order in PMN-related relaxors: structure, stability, modification, and impact on properties," *J. Phys. Chem. Solids*, vol. 61, no. 2, pp. 159–166, 2000.

[72] T. Tsurumi, K. Soejima, T. Kamiya, and M. Daimon, "Mechanism of diffuse phase transition in relaxor ferroelectrics," *Jpn. J. Appl. Phys.*, vol. 33, no. 4R, pp. 1959–1964, 1994.

[73] A. A. Bokov and Z. G. Ye, "Recent progress in relaxor ferroelectrics with perovskite structure," *J. Mater. Sci.*, vol. 41, no. 1, pp. 31–52, 2006.

[74] B. Jaffe, W. R. Cook, and H. L. Jaffe, *Piezoelectric ceramics*. London: Academic Press, 1971.

[75] H. Ouchi, K. Nagano, and S. Hayakawa, "Piezoelectric Properties of $Pb(Mg_{1/3}Nb_{2/3})O_3$-$PbTiO_3$-$PbZrO_3$ Solid Solution Ceramics," *J. Am. Ceram. Soc.*, vol. 48, no. 12, pp. 630–635, 1965.

[76] A. K. Singh, D. Pandey, and O. Zaharko, "Powder neutron diffraction study of phase transitions in and a phase diagram of (1-x) [Pb $(Mg_{1/3}Nb_{2/3})O_3$]-x$PbTiO_3$," *Phys. Rev. B - Condens. Matter Mater. Phys.*, vol. 74, no. 2, p. 024101, 2006.

[77] T. Y. Koo and S.-W. Cheong, "Dielectric and piezoelectric enhancement due to 90° domain rotation in the tetragonal phase of $Pb(Mg_{1/3}Nb_{2/3})O_3$-$PbTiO_3$," *Appl. Phys. Lett.*, vol. 80, no. 22, pp. 4205–4207, 2002.

[78] A. K. Singh and D. Pandey, "Structure and the location of the morphotropic phase boundary region in (1-x)[$Pb(Mg_{1/3}Nb_{2/3})O_3$]-x$PbTiO_3$," *J. Phys. Condens. Matter*, vol. 13, no. 48, pp. L931–L936, 2001.

[79] J. Kelly, M. Leonard, C. Tantigate, and A. Safari, "Effect of Composition on the Electromechanical Properties of (1-x)$Pb(Mg_{1/3}Nb_{2/3})O_3$—x$PbTiO_3$ Ceramics," *J. Am. Ceram. Soc.*, vol. 80, no. 4, pp. 957–964, 1997.

[80] Z. Xia, L. Wang, W. Yan, Q. Li, and Y. Zhang, "Comparative investigation of structure and dielectric properties of $Pb(Mg_{1/3}Nb_{2/3})O_3$–$PbTiO_3$ (65/35) and 10% $PbZrO_3$-doped $Pb(Mg_{1/3}Nb_{2/3})O_3$–$PbTiO_3$ (65/35) ceramics prepared by a modified precursor method" *Mater. Res. Bull.*, vol. 42, no. 9, pp. 1715–1722, 2007.

[81] M. Algueró, J. Ricote, R. Jiménez, P. Ramos, J. Carreaud, B. Dkhil, J. M. Kiat, J. Holc, and M. Kosec, "Size effect in morphotropic phase boundary $Pb(Mg_{⅓}Nb_{⅔})O_3$–$PbTiO_3$," *Appl. Phys. Lett.*, vol. 91, no. 11, p. 112905, 2007.

[82] M. Vrabelj, H. Uršič, Z. Kutnjak, B. Rožič, S. Drnovšek, A. Benčan, V. Bobnar, L. Fulanović, and B. Malič, "Large electrocaloric effect in grain-size-engineered $0.9Pb(Mg_{1/3}Nb_{2/3})O_3$ –$0.1PbTiO_3$," *J. Eur. Ceram. Soc.*, vol. 36, no. 1, pp. 75–80, 2016.

[83] J. Peräntie, H. N. Tailor, J. Hagberg, H. Jantunen, and Z.-G. Ye, "Electrocaloric properties in relaxor ferroelectric (1—x)$Pb(Mg_{1/3}Nb_{2/3})O_3$ – x$PbTiO_3$ system," *J. Appl. Phys.*, vol. 114, no. 17, p. 174105, 2013.

[84] U. Plaznik, A. Kitanovski, B. Rožič, B. Malič, H. Uršič, S. Drnovšek, J. Cilenšek, M. Vrabelj, A. Poredoš, and Z. Kutnjak, "Bulk relaxor ferroelectric ceramics as a

working body for an electrocaloric cooling device," *Appl. Phys. Lett.*, vol. 106, no. 4, p. 043903, 2015.

[85] M. G. Del Duca, J. Tušek, A. Maiorino, L. Fulanović, A. Bradeško, U. Plaznik, B. Malič, C. Aprea, and A. Kitanovski, "Comprehensive evaluation of electrocaloric effect and fatigue behavior in the $0.9Pb(Mg_{1/3}Nb_{2/3})O_3$–$0.1PbTiO_3$ bulk relaxor ferroelectric ceramic," *J. Appl. Phys.*, vol. 128, no. 10, p. 104102, 2020.

[86] M. Otonicar, H. Ursic, M. Dragomir, A. Bradesko, G. Esteves, J. L. Jones, A. Bencan, B. Malic, and T. Rojac, "Multiscale field-induced structure of (1-x)$Pb(Mg_{1/3}Nb_{2/3})O_3$–x$PbTiO_3$ ceramics from combined techniques," *Acta Mater.*, vol. 154, pp. 14–24, 2018.

[87] G. Helke and K. Lubitz, "Piezoelectric PZT Ceramics," in *Piezoelectricity*, Berlin: Springer, 2008.

[88] J. Akedo, "Microstructure of Ceramic Thick Film Formed by Aerosol Deposition and its Applications to Microactuator," *Integr. Ferroelectr.*, vol. 80, no. 1, pp. 55–65, 2006.

[89] N. Asai, R. Matsuda, M. Watanabe, H. Takayama, S. Yamada, A. Mase, M. Shikida, K. Sato, M. Lebedev, and J. Akedo, "Novel high resolution optical scanner actuated by aerosol deposited PZT films," in *The Sixteenth Annual International Conference on Micro Electro Mechanical Systems, MEMS-03,* Kyoto, Japan: Institute of Electrical and Electronics Engineers (IEEE), 2003.

[90] J.-H. Park, J. Akedo, M. Lebedev, and H. Sato, "Optical scanning devices based on PZT thick films formed by aerosol deposition method," in *Proceedings SPIE 6037, Device and Process Technologies for Microelectronics, MEMS, and Photonics IV,* Brisbane, Australia: International Society for Optics and Photonics (SPIE), 2005.

[91] J. Jung, V. Annapureddy, G. T. Hwang, Y. Song, W. Lee, W. Kang, J. Ryu, and H. Choi, "31-mode piezoelectric micromachined ultrasonic transducer with PZT thick film by granule spraying in vacuum process," *Appl. Phys. Lett.*, vol. 110, no. 21, p. 212903, 2017.

[92] M. Iwanami, M. Nakada, H. Tsuda, K. Ohashi, and J. Akedo, "Ultra small electro-optic field probe fabricated by aerosol deposition," *IEICE Electron. Express*, vol. 4, no. 2, pp. 26–32, 2007.

[93] M. Nakada, H. Tsuda, K. Ohashi, and J. Akedo, "Aerosol deposition on transparent electro-optic films for optical modulators," in *IEICE Transactions on Electronics*, 2007, vol. E90-C, no. 1, pp. 36–40.

[94] M. Nakada, T. Shimizu, H. Miyazaki, H. Tsuda, J. Akedo, and K. Ohashi, "Lanthanum-modified lead zirconate titanate electro-optic modulators fabricated using aerosol deposition for LSI interconnects," *Jpn. J. Appl. Phys.*, vol. 48, no. 9, p. 09KA06, 2009.

[95] S. P. Yeh, L. T. Wang, Y. J. Wang, S. C. Lin, Y. S. Shih, and W. J. Wu, "Recent progress on micro-piezoelectric energy harvesters fabricated with aerosol deposition method and the interfacing circuits," in *SPIE Smart Structures and Materials + Nondestructive Evaluation and Health Monitoring*, 2014, vol. 90570M.

[96] C. L. Kuo, S. C. Lin, and W. J. Wu, "Fabrication and performance evaluation of a metal-based bimorph piezoelectric MEMS generator for vibration energy

harvesting," *Smart Mater. Struct.*, vol. 25, no. 10, p. 105016, 2016.

[97] G. T. Hwang, V. Annapureddy, J. H. Han, D. J. Joe, C. Baek, D. Y. Park, D. H. Kim, J. H. Park, C. K. Jeong, K. Il Park, J. J. Choi, D. K. Kim, J. Ryu, and K. J. Lee, "Self-Powered Wireless Sensor Node Enabled by an Aerosol-Deposited PZT Flexible Energy Harvester," *Adv. Energy Mater.*, vol. 6, no. 13, 2016.

[98] S. Bin Kang, M. G. Choi, D. Y. Jeong, Y. M. Kong, and J. Ryu, "Energy storage properties of nano-grained antiferroelectric (Pb, La)(Zr, Ti)O_3 films prepared by aerosol-deposition method," *IEEE Trans. Dielectr. Electr. Insul.*, vol. 22, no. 3, pp. 1477–1482, 2015.

[99] B. Ma, T. H. Lee, S. E. Dorris, R. E. Koritala, and U. Balachandran, "Flexible ceramic film capacitors for high-temperature power electronics," *Mater. Sci. Energy Technol.*, vol. 2, no. 1, pp. 96–103, 2019.

[100] A. Kumar, S. H. Kim, A. Thakre, G. Lee, Y. G. Chae, and J. Ryu, "Increased Energy-Storage Density and Superior Electric Field and Thermally Stable Energy Efficiency of Aerosol-Deposited Relaxor $(Pb_{0.89}La_{0.11})(Zr_{0.70}Ti_{0.30})O_3$ Films," *J. Therm. Spray Technol.*, vol. 30, no. 3, pp. 591–602, 2021.

[101] H.-B. Jung, J.-H. Lim, M. Peddigari, J. Ryu, D. H. Choi, and D.-Y. Jeong, "Enhancement of energy storage and thermal stability of relaxor $Pb_{0.92}La_{0.08}Zr_{0.52}Ti_{0.48}O_3$-$Bi(Zn_{0.66}Nb_{0.33})O_3$ thick films through aerosol deposition," *J. Eur. Ceram. Soc.*, vol. 40, no. 1, pp. 63–70, 2020.

[102] A. Kumar, G. Lee, Y. G. Chae, A. Thakre, H. S. Choi, G. H. Nam, and J. Ryu, "Induced slim ferroelectric hysteresis loops and enhanced energy-storage properties of Mn-doped $(Pb_{0.93}La_{0.07})(Zr_{0.82}Ti_{0.18})O_3$ anti-ferroelectric thick films by aerosol deposition," *Ceram. Int.*, vol. 47, no. 22, pp. 31590–31596, 2021.

[103] Z. Yao, C. Wang, Y. Li, H. K. Kim, and N. Y. Kim, "Effects of starting powder and thermal treatment on the aerosol deposited $BaTiO_3$ thin films toward less leakage currents," *Nanoscale Res. Lett.*, vol. 9, no. 1, pp. 4–9, 2014.

[104] T. Hoshina, T. Furuta, Y. Kigoshi, S. Hatta, N. Horiuchi, H. Takeda, and T. Tsurumi, "Size Effect of Nanograined $BaTiO_3$ Ceramics Fabricated by Aerosol Deposition Method," *Jpn. J. Appl. Phys.*, vol. 49, no. 9, pp. 1–5, 2010.

[105] U. Eckstein, J. Exner, A. Bencan Golob, K. Ziberna, G. Drazic, H. Ursic, H. Wittkämper, C. Papp, J. Kita, R. Moos, K. G. Webber, and N. H. Khansur, "Temperature-dependent dielectric anomalies in powder aerosol deposited ferroelectric ceramic films," *J. Mater.*, 2022, In press. doi: 10.1016/j.jmat.2022.05.001.

[106] F. Zhuo, U. R. Eckstein, N. H. Khansur, C. Dietz, D. Urushihara, T. Asaka, K. Kakimoto, K. G. Webber, X. Fang, and J. Rödel, "Temperature-induced changes of the electrical and mechanical properties of aerosol-deposited $BaTiO_3$ thick films for energy storage applications," *J. Am. Ceram. Soc.*, vol. 105, no. 6, pp. 4108–4121, 2022.

[107] C.-T. Chen, S.-C. Lin, U. Trstenjak, M. Spreitzer, and W.-J. Wu, "Comparison of Metal-Based PZT and PMN–PT Energy Harvesters Fabricated by Aerosol Deposition Method," *Sensors (Basel)*, vol. 21, no. 14, p. 4747, 2021.

[108] A. Thakre, A. Kumar, M. Y. Lee, D. R. Patil, S. H. Kim, and J. Ryu, "Artificially

induced normal ferroelectric behaviour in aerosol deposited relaxor 65PMN-35PT thick films by interface engineering," *J. Mater. Chem. C*, vol. 9, no. 10, pp. 3403–3411, 2021.

[109] J. J. Choi, B. D. Hahn, J. Ryu, W. H. Yoon, and D. S. Park, "Effects of $Pb(Zn_{1/3}Nb_{2/3})O_3$ addition and postannealing temperature on the electrical properties of Pb $(Zr_xTi_{1-x})O_3$ thick films prepared by aerosol deposition method," *J. Appl. Phys.*, vol. 102, no. 4, pp. 1–6, 2007.

[110] J. Akedo and M. Lebedev, "Effects of annealing and poling conditions on piezoelectric properties of $Pb(Zr_{0.52},Ti_{0.48})O_3$ thick films formed by aerosol deposition method," *J. Cryst. Growth*, vol. 235, no. 1–4, pp. 415–420, 2002.

[111] Y. Kawakami, S. Aisawa, and J. Akedo, "Annealing Effect on $0.5Pb(Ni_{1/3}Nb_{2/3})O_3$-$0.5Pb(Zr_{0.3}Ti_{0.7})O_3$ Thick Film Deposited By Aerosol Deposition Method," *Jpn. J. Appl. Phys.*, vol. 44, no. 9B, pp. 6934–6937, 2005.

[112] R. Gerson and T. C. Marshall, "Dielectric breakdown of porous ceramics," *J. Appl. Phys.*, vol. 30, no. 11, pp. 1650–1653, 1959.

[113] T. Miyoshi, M. Nakajima, and H. Funakubo, "Effects of substrate clamping on electrical properties of polycrystalline piezoelectric films," *Jpn. J. Appl. Phys.*, vol. 48, no. 9 Part 2, pp. 1–6, 2009.

[114] G. Han, J. Ryu, W.-H. Yoon, J.-J. Choi, B.-D. Hahn, J.-W. Kim, D.-S. Park, C.-W. Ahn, S. Priya, and D.-Y. Jeong, "Stress-controlled $Pb(Zr_{0.52}Ti_{0.48})O_3$ thick films by thermal expansion mismatch between substrate and $Pb(Zr_{0.52}Ti_{0.48})O_3$ film," *J. Appl. Phys.*, vol. 110, no. 12, p. 124101, 2011.

[115] G. Han, J. Ryu, W.-H. Yoon, J.-J. Choi, B.-D. Hahn, and D.-S. Park, "Effect of Film Thickness on the Piezoelectric Properties of Lead Zirconate Titanate Thick Films Fabricated by Aerosol Deposition," *J. Am. Ceram. Soc.*, vol. 94, no. 5, pp. 1509–1513, 2011.

[116] M. Kosec, J. Holc, B. Malič, and V. Bobnar, "Processing of high performance lead lanthanum zirconate titanate thick films," *J. Eur. Ceram. Soc.*, vol. 19, no. 6–7, pp. 949–954, 1999.

[117] R. A. Dorey and R. W. Whatmore, "Electroceramic Thick Film Fabrication for MEMS," *J. Electroceramics*, vol. 12, no. 1/2, pp. 19–32, 2004.

[118] S. Khan, L. Lorenzelli, and R. S. Dahiya, "Technologies for Printing Sensors and Electronics Over Large Flexible Substrates: A Review," *IEEE Sens. J.*, vol. 15, no. 6, pp. 3164–3185, 2015.

[119] I.-C. Cheng and S. Wagner, "Overview of Flexible Electronics Technology," in *Flexible Electronics: Materials and Applications*, Springer, 2009, pp. 1–28.

[120] J. A. Spechler, T. W. Koh, J. T. Herb, B. P. Rand, and C. B. Arnold, "A Transparent, Smooth, Thermally Robust, Conductive Polyimide for Flexible Electronics," *Adv. Funct. Mater.*, vol. 25, no. 48, pp. 7428–7434, 2015.

[121] U. Gabor, M. Spreitzer, H. Uršič, E. Tchernychova, Z. Samardžija, W. J. Wu, and D. Suvorov, "Structural peculiarities of 0.67 $Pb(Mg_{1/3}Nb_{2/3})O_3$–0.33 $PbTiO_3$ thin films grown directly on $SrTiO_3$ substrates," *J. Eur. Ceram. Soc.*, vol. 38, no. 13, pp. 4453–4462, 2018.

[122] M. K. Kim, S. Y. Ji, J. H. Lim, S. W. Kim, and D. Y. Jeong, "Energy storage

performance and thermal stability of BNT-SBT with artificially modulated nanograins via aerosol deposition method," *J. Asian Ceram. Soc.*, vol. 10, no. 1, pp. 196–202, 2022.

Bibliography

Scientific Articles Related to the Thesis

M. Sadl, O. Condurache, A. Benčan, M. Dragomir, U. Prah, B. Malič, M. Deluca, U. Eckstein, D. Hausmann, N. H. Khansur, K. G. Webber, H. Uršič, "Energy-storage-efficient $0.9Pb(Mg_{1/3}Nb_{2/3})O_3$–$0.1PbTiO_3$ thick films integrated directly onto stainless steel", *Acta materialia*, vol. 221, p. 117403, 2021.

M. Sadl, A. Lebar, J. Valentinčič, H. Uršič, "Flexible energy-storage ceramic thick-film structures with high flexural fatigue endurance", *ACS applied energy materials*, vol. 5, no. 6, pp. 6896–6902, 2022.

K. Nadaud, M. Sadl, M. Bah, F. Levassort, H. Uršič, "Effect of thermal annealing on dielectric and ferroelectric properties of aerosol-deposited $0.65Pb(Mg_{1/3}Nb_{2/3})O_3$-$0.35PbTiO_3$ thick films", *Applied physics letters*, vol. 120, no. 11, p. 112902, 2022.

M. Sadl, K. Nadaud, M. Bah, F. Levassort, U. Eckstein, N. H. Khansur, K. G. Webber, H. Uršič, "Multifunctional energy storage and piezoelectric properties of $0.65Pb(Mg_{1/3}Nb_{2/3})O_3$–$0.35PbTiO_3$ thick films on stainless-steel substrates", *JPhys energy*, vol. 4, no. 2, p. 024004, 2022.

Other Scientific Articles

E. Khomyakova, M. Sadl, H. Uršič, J. Daniels, B. Malič, A. Benčan, D. Damjanović, T. Rojac, "Self-poling of $BiFeO_3$ thick films," *ACS applied materials & interfaces.*, vol. 8, no. 30, pp. 19626–19634, 2016.

M. Sadl, A. Bradeško, D. Belavič, A. Benčan, B. Malič, T. Rojac, "Construction and functionality of a ceramic resonant pressure sensor for operation at elevated temperatures", *Sensors (Basel)*, vol. 18, no. 5, p. 1423, 2018.

M. Sadl, U. Tomc, U. Prah, H. Uršič, "Protective alumina coatings prepared by aerosol deposition on magnetocaloric gadolinium elements", *Informacije MIDEM*, vol. 49, no. 3, pp. 177–182, 2019.

N. H. Khansur, U. Eckstein, M. Sadl, H. Uršič, K. G. Webber, "Fabrication of porous thick films using room-temperature aerosol deposition", *Journal of the American Ceramic Society*, vol. 103, no. 1, pp. 43–47, 2020.

J. Walker, A. Mirjanić, U. Prah, M. Sadl, O. Condurache, A. Benčan, T. Rojac, M. Grigoras, H. Uršič, "Magnetic contributions in multiferroic gadolinium modified bismuth ferrite ceramics", *Scripta materialia*, vol. 188, pp. 233–237, 2020.

N. H. Khansur, U. Eckstein, H. Uršič, M. Sadl, M. Brehl, A. Martin, K. Riess, D. de Ligny, K. G. Webber, "Enhanced electromechanical response and thermal stability of $0.93(Na_{1/2}Bi_{1/2})TiO_3$–$0.07BaTiO_3$ through aerosol deposition of base metal electrodes", *Advanced materials interfaces*, vol. 8, no. 11, p. 2100309, 2021.

M. Sadl, U. Tomc, H. Uršič, "Investigating the feasibility of preparing metal-ceramic multi-layered composites using only the aerosol-deposition technique", *Materials (Basel)*, vol. 14, no. 16, pp. 1–10, 2021.

U. Eckstein, M. Sadl, M. Dragomir, H. Uršič, et al., "Room temperature deposition of freestanding $BaTiO_3$ films", *Journal of Materials Science*, vol. 57, no. 28, pp. 13264–13286, 2022.

Published Scientific Conference Contributions – Abstracts (Invited Lecture)

H. Uršič, M. Sadl, U. Eckstein, N. H. Khansur, K. G. Webber, U. Prah, B. Malič, "$Pb(Mg_{1/3}Nb_{2/3})O_3$–$PbTiO_3$ thick films prepared by aerosol deposition onto metal and polymer substrates", in *IEEE IFCS 2020 ISAF 2020 Virtual Conference*, Keystone, Colorado, USA: joint Conference of IEEE International Symposium on Applications of Ferroelectrics, 2020.

U. Tomc, S. Dall′Olio, K. Klinar, S. Nosan, U. Erjavec, M. Sadl, H. Uršič, A. Kitanovski, "Cool future: magnetocaloric devices based on static and rare earth free magnetic field sources", in *CHC Eurotherm Seminar, 2021*, Eurotherm, 2021.

N. H. Khansur, U. Eckstein, M. Sadl, H. Uršič, K. G. Webber, "Impact modulated electromechanical response in functional ceramics using aerosol deposition", in *IEEE ISAF 2021 joint ISAF ISIF-PMF virtual Conference, IEEE International Symposium on Applications of Ferroelectric (ISAF), International Symposium on Integrated Functionalities (ISIF), Piezoresponse Force Microscopy Workshop (PFM)*, Sydney, Australia: Institute of Electrical and Electronics Engineers (IEEE), 2021.

Published Scientific Conference Contributions – Abstracts

E. Khomyakova, M. Sadl, H. Uršič, J. E. Daniels, B. Malič, A. Benčan, D. Damjanović, T. Rojac, B. Malič, "Self-poling effect in bismuth ferrite thick films", in *2016 joint IEEE ISAF-ECAPD-PMF 2016, International Symposium on Applications of Ferroelectrics (ISAF), European Conference on the Applications of Polar Dielectrics (ECAPD), Workshop on Piezoresponse Force Microscopy (PMF),* Darmstadt, Germany: Technische Univetität, 2016.

E. Khomyakova, M. Sadl, H. Uršič, J. E. Daniels, B. Malič, A. Benčan, D. Damjanović, T. Rojac, "Annealing through the ferroelectric-to-paraelectric phase transition induces self-poling effect in bismuth ferrite thick films", in *COST TO-BE Fall Meeting*, Ljubljana, Slovenia: Jožef Stefan Institute, 2016.

E. Khomyakova, M. Sadl, H. Uršič, J. E. Daniels, B. Malič, A. Benčan, D. Damjanović, T. Rojac, "Self-poling of $BiFeO_3$ thick films induced by the annealing through the ferroelectric-to-paraelectric phase transition", in *Piezo 2017 : Electroceramics for End-Users IX,* Madrid, Spain: The Euroepan Institute of Piezoelectric Materials and Devices, 2017.

M. Sadl, E. Khomyakova, H. Uršič, T. Rojac, B. Malič, A. Benčan, "Thickness-dependent structural and microstructural properties of self-poled $BiFeO_3$ thick films", in *9th Jožef Stefan International Postgraduate School Students′ Conference and 11th Young researchers′ Day*, Ljubljana, Slovenija: Jožef Stefan International Postgraduate School, Jožef Stefan Institute, 2017.

M. Sadl, A. Bradeško, D. Belavič, A. Benčan, B. Malič, T. Rojac, "Ceramic resonant pressure sensor with an integrated piezoelectric bismuth ferrite and its functionality at elevated temperatures", in *54th International Conference on Microelectronics, Devices and Materials & the Workshop on Sensors and Transducers*, Ljubljana, Slovenia: MIDEM - Society for Microelectronics, Electronic Components and Materials, 2018.

M. Sadl, U. Eckstein, N. H. Khansur, K. G. Webber, U. Prah, A. Bradeško, B. Malič, H. Uršič, "$Pb(Mg_{1/3}Nb_{2/3})O_3$–$PbTiO_3$ thick films prepared by aerosol deposition onto low-cost substrates", in *55th International Conference on Microelectronics, Devices and Materials with the Workshop on Laser Systems and Photonics*, Ljubljana, Slovenia: MIDEM - Society for Microelectronics, Electronic Components and Materials, 2019.

U. Tomc, M. Sadl, H. Uršič, "Digital microfluidics in caloric cooling", in *E-MRS 2019 Fall Meeting,* Warsaw, Poland: Faculty of Materials Science and Engineering, 2019.

M. Sadl, U. Tomc, U. Prah, A. Bradeško, B. Malič, U. Eckstein, N. H. Khansur, K. G. Webber, H. Uršič, "Using the aerosol deposition method in the preparation of caloric-cooling elements", in *E-MRS 2019 Fall Meeting,* Warsaw, Poland: Faculty of Materials Science and Engineering, 2019.

M. Sadl, U. Eckstein, N. H. Khansur, K. G. Webber, U. Prah, B. Malič, H. Uršič, "$0.9Pb(Mg_{1/3}Nb_{2/3})O_3$–$0.1PbTiO_3$ thick films prepared by aerosol deposition onto low-cost metal substrates", in *Joint ISAF-ICE-EMF-IWPM-PFM meeting, 2019 IEEE International Symposium on Applications of Ferroelectrics (ISAF),* Lausanne, Switzerland: IEEE Advancing Technology for Humanity, École Polytechnique Fédérale de Lausanne, 2019.

M. Sadl, U. Eckstein, N. H. Khansur, K. G. Webber, U. Prah, B. Malič, H. Uršič, "Aerosol deposition of relaxor-ferroelectric $0.9Pb(Mg_{1/3}Nb_{2/3})O_3$–$0.1PbTiO_3$ thick films onto low-cost metal substrates", in *11th Jožef Stefan International Postgraduate School Students' Conference and 13th Young Researchers' Day*, Planica, Slovenia: Jožef Stefan International Postgraduate School, Jožef Stefan Institute, 2019.

M. Koblar, B. Leskovar, E. Khomyakova, M. Sadl, A. Benčan, B. Šetina, N. Stanković, S. Drev, M. Čeh, "Electron backscattered diffraction (EBSD) in materials science", in *3. slovensko posvetovanje mikroskopistov*, Ankaran, Slovenia: Slovensko društvo za mikroskopijo, 2019.

M. Sadl, U. Eckstein, N. H. Khansur, K. G. Webber, U. Prah, B. Malič, H. Uršič, "PMN-PT thick films on low-cost and flexible materials realized by aerosol deposition method", in *Electroceramics XVII, International Virtual Conference*, Darmstadt, Germany: Technische Universität, 2020.

A. Dubey, D. Lewin, U. Prah, M. Sadl, M. Escobar Castillo, H. Uršič, T. Rojac, V. V. Shvartsman, D. C. Lupascu, "Ferroelectric properties of Ba and Mn doped bismuth ferrite bulk and nanoparticles", in *IEEE IFCS 2020 ISAF 2020 Virtual Conference*, Keystone, Colorado, USA: joint Conference of IEEE International Symposium on Applications of Ferroelectrics, 2020.

A. Mirjanić, U. Prah, M. Sadl, J. Walker, O. Condurache, A. Benčan, T. Rojac, M. Grigoras, H. Uršič, "Local piezoelectric and magnetic properties of $(Bi_{0.88}Gd_{0.12}FeO_3$ ceramics", in *12th Jožef Stefan International Postgraduate School Students' Conference and 14th Young Researchers' Day*, Ljubljana, Slovenia: Jožef Stefan International Postgraduate School, Jožef Stefan Institute, 2020.

M. Sadl, O. Condurache, A. Benčan, M. Dragomir, U. Prah, B. Malič, H. Uršič, "Aerosol deposition as an enabling technology for flexible energy storage and electrocaloric devices", in *[1st] Crossnano Crossborder Workshop in Nanoscience and Nanotechnology*, Trieste, Italy: University of Trieste, 2021.

M. Sadl, O. Condurache, A. Benčan, M. Dragomir, U. Prah, B. Malič, H. Uršič, "Energy storage and electrocaloric $(1–x)Pb(Mg_{1/3}Nb_{2/3})O_3$–$xPbTiO_3$ thick films realized by aerosol deposition method", in *56th International Conference on Microelectronics, Devices and Materials & the Workshop on Personal Sensor for Remote Health Care*

Monitoring, Ljubljana, Slovenia: MIDEM - Society for Microelectronics, Electronic Components and Materials, 2021.

K. Makarovič, M. Sadl, A. Bradeško, M. Jerlah, D. Belavič, B. Malič, "From material to 3D LTCC structures developed for electronic components and devices", in *56th International Conference on Microelectronics, Devices and Materials & the Workshop on Personal Sensor for Remote Health Care Monitoring*, Ljubljana, Slovenia: MIDEM - Society for Microelectronics, Electronic Components and Materials, 2021.

H. Uršič, M. Sadl, O. Condurache, A. Benčan, M. Dragomir, B. Malič, "Relaxor-ferroelectric $0.9Pb(Mg_{1/3}Nb_{2/3})O_3{-}0.1PbTiO_3$ ceramic thick films integrated by aerosol deposition on stainless-steel and polymer substrates", in *8th International Workshop on piezoelectric MEMS: online/on-site hybrid meeting*, Nara, Japan: 2021.

M. Sadl, O. Condurache, M. Dragomir, A. Benčan, U. Prah, B. Malič, H. Uršič, et al., "$0.9Pb(Mg_{1/3}Nb_{2/3})O_3{-}0.1PbTiO_3$ thick films integrated by aerosol deposition on metal and polymer substrates", in *Electronic materials and applications (EMA) 2021*, virtual only event: The American Ceramic Society, 2021.

M. Sadl, O. Condurache, A. Benčan, M. Dragomir, U. Prah, B. Malič, M. Deluca, et al., "Integration of aerosol deposited $0.9Pb(Mg_{1/3}Nb_{2/3})O_3{-}0.1PbTiO_3$ thick films on low-cost stainless steel and flexible polymer substrates", in *IEEE ISAF 2021 joint ISAF ISIF-PMF virtual Conference, IEEE International Symposium on Applications of Ferroelectric (ISAF), International Symposium on Integrated Functionalities (ISIF), Piezoresponse Force Microscopy Workshop (PFM)*, Sydney, Australia: Institute of Electrical and Electronics Engineers (IEEE), 2021.

U. Tomc, M. Sadl, K. Klinar, H. Uršič, A. Kitanovski, "Digital microfluidics in magnetocaloric cooling", in *THERMAG IX: 9th IIR International Conference on Caloric Cooling and Applications of Caloric Materials: virtual conference*, College Part, Maryland, USA: 2021.

M. Sadl, O. Condurache, A. Benčan, M. Dragomir, U. Prah, B. Malič, H. Uršič, "Relaxor-ferroelectric ceramic thick films integrated by aerosol deposition on metal and polymer substrates", in *13th Jožef Stefan International Postgraduate School Students' Conference and 15th Young Researchers' Day*, Ljubljana, Slovenija: Jožef Stefan International Postgraduate School, Jožef Stefan Institute, 2021.

M. Sadl, A. Lebar, J. Valentinčič, H. Uršič, "Integration of relaxor-ferroelectric $0.9Pb(Mg_{1/3}Nb_{2/3})O_3{-}0.1PbTiO_3$ thick films on polymer substrates", in *14th Jožef Stefan International Postgraduate School Students' Conference*, Kamnik, Slovenia: Jožef Stefan International Postgraduate School, Jožef Stefan Institute, 2022.

V. Regis Moraes, M. Sadl, H. Uršič, "Preparation of multicaloric composites by aerosol deposition method", in *2022 UFFC ferroelectrics school*, Lyon, France: INSA Ecole Centrale de Lyon, 2022.

U. Prah, M. Sadl, V. Kovacova, P. Lheritier, Y. Nouchokgwe, A. Torello, H. Uršič, E. Defay, "Direct electrocaloric measurements of flexible $Pb(Mg_{1/3}Nb_{2/3})O_3{-}PbTiO_3$ ceramic films", in *ISAF 2022: ISAF-PFM-ECAPD joint conference*, Tours, France: Institute of Electrical and Electronics Engineers (IEEE), 2022.

V. Regis Moraes, M. Sadl, H. Uršič, et al., "Preparation of multicaloric composites using aerosol deposition method", in *ISAF 2022: ISAF-PFM-ECAPD joint conference*, Tours, France: Institute of Electrical and Electronics Engineers (IEEE), 2022.

M. Sadl, O. Condurache, A. Benčan, M. Dragomir, B. Malič, A. Lebar, J. Valentinčič, H. Uršič, et al., "Energy storage $Pb(Mg_{1/3}Nb_{2/3})O_3{-}PbTiO_3$ thick films integrated by aerosol deposition on metal and polymer substrates", in *ISAF 2022: ISAF-PFM-*

ECAPD joint conference, Tours, France: Institute of Electrical and Electronics Engineers (IEEE), 2022.

Unpublished Scientific Conference Contributions

H. Uršič, M. Sadl, O. Condurache, A. Benčan, M. Dragomir, U. Eckstein, N. H. Khansur, K. G. Webber, M. Deluca, U. Prah, B. Malič, "Aerosol-deposited $Pb(Mg_{1/3}Nb_{2/3})O_3$–$PbTiO_3$ films on metal and polymer substrates", *Workshop Recent Advances in Nanoscience and It's Applications,* Zoom seminar, 2020.

M. Sadl, "Energy storage and piezoelectric properties of $0.65Pb(Mg_{1/3}Nb_{2/3})O_3$–$0.35PbTiO_3$ thick films on stainless-steel substrate", in *Japan - Slovenia workshop on piezoelectric thin films,* Zoom seminar, 2022.

Invited Lecture at Foreign Universities

O. Condurache, H. Uršič, M. Sadl, K. Radan, U. Prah, M. Otoničar, B. Kmet, G. Dražić, B. Malič, A. Benčan, "Studies of different ceramic systems by means of electron microscopy techniques" Iasi, Romania: Laboratory for Dielectrics, Ferroelectrics and Multiferroics, Faculty of Physics, University “A.I. Cuza”, 2019.

Biography

The author of this thesis was born in 1994 on the 12th of February in Murska Sobota. After finishing the Gymnasium in Ljutomer in 2013, he enrolled in a Chemical Engineering programme at the Faculty of Chemistry and Chemical Technology, University of Ljubljana. After completing his first year of studies, he started working as a student in the Electronic Ceramics Department (K5), Jožef Stefan Institute (JSI). In September 2016, he received a BSc degree in Chemical Engineering. His diploma thesis entitled "Characterization of Bismuth Ferrite Thick Films, Prepared by Screen-Printing, on a Low Temperature Co-Fired Ceramics Substrate" was conducted under the supervision of Prof. Dr Marjan Marinšek from the University of Ljubljana and the co-supervision of Prof. Dr. A. Benčan Golob from K5, JSI.

After graduation, he became a MSc student of Nanosciences and Nanotechnologies at the Jožef Stefan International Postgraduate School. In 2018, he finished MSc studies with the master thesis entitled: "Bismuth Ferrite in the Form of Thick Films and its Integration into a Resonant Pressure Sensor". In the same year he published as first author his first article entitled: "Construction and Functionality of a Ceramic Resonant Pressure Sensor for Operation at Elevated Temperatures."

In 2018 he enrolled in the PhD program in Sensor Technologies at Jožef Stefan International Postgraduate School under the supervision of Prof. Dr. H. Uršič. In the last 4 years, his research activities have been mainly devoted to the processing and characterization of functional ceramic thick films. He mainly works with $Pb(Mg_{1/3}Nb_{2/3})O_3$–$PbTiO_3$–based perovskite thick films deposited by aerosol deposition. He is particularly interested in studying how the structural and microstructural properties affect the functional properties of thick films, i.e., dielectric, energy storage, electro-mechanical and electrocaloric properties.

In 2021 he received the "student competition" awards at two international conferences: the joint 2021 ISAF-ISIF-PMF virtual Conference, and Crossnano Crossborder Workshop in Nanoscience and Nanotechnology 2021.